What is the flux of low energy electron precipitation in the lower thermosphere?

Haakon Dahl Eide

June 2022

Master thesis in space physics

Supervisor: **Dr. Hilde Nesse Tyssøy**

Co-supervisor: **Dr. Christine Smith-Johnsen**

Department of Physics and Technology
University of Bergen

Acknowledgement

First, I want to extend my deepest thanks and gratitude to my supervisor and team leader of Particle Precipitation group at BCSS, Dr. Hilde Nesse Tyssøy. From the laughter filled meetings (both in person and zoom), to the advice, help and encouragement, this thesis would have not been possible without you. I would also like to thank my Co-supervisor (for 6 months!!) Dr. Christine Smith-Johnsen, for the joy she brought to meetings and for all the help and advice she gave, especially surrounding MATLAB and WACCM related issues (even after she moved jobs!!). I would also like to extend my thanks to Dr. Fasil Tesema, for all the DMSP data and help he provided. Further, I want to thank Dr. Jan Maik Wissing for the AIMOS data, and all the help gave with AIMOS and the various bugs we discovered with AIMOS' website.

I like to thank all the members of the Particle Precipitation group at BCSS for all the help and advice they gave me, as well as all the fun we had at various group activities. I would like to also give my thanks to the entire Space physics group for all the kindness and warmth you have shown me and all the joy and laughter you have shared. I do not regret my choice of taking my master degree at the Birkeland Centre. I also want to give special thanks to Josephine and Eldho, for making days at the office fun, as well as all the help you have given me. Either if it was proof reading my thesis (Josephine) or providing me with data and helping with MATLAB (Eldho).

I want to thank my parents for always supporting me, checking up on me (even if am not the fastest to respond) and indulging my rants about various events and news. I'd like to thank my three siblings for always being supportive and encouraging. My thanks goes also to my friends for all the fun nights, movies, activities, beers and discussions we have shared over both my master and bachelor degree. Lastly I want to thank my girlfriend for always supporting me and being there for me, for both the good days and bad days. From encouraging me when i felt down, cheering me on when I was able to locate bugs in my various codes, to indulging in my many rants when LaTeX or MATLAB didn't do what i wanted!! I wouldn't be able to do this without you.

Abstract

The ionisation caused by Energetic particle precipitation (EPP) into the atmosphere, lead to chemical reactions producing NO_x (N, NO, NO_2) gases. Auroral electrons (1-30 keV) deposit their energy throughout the upper mesosphere and lower thermosphere. During the dark winter, the EPP-produced NO_x gases can survive for months and be transported down to the stratosphere, where it will destroy ozone through catalytic reactions. Studies comparing the NO density estimated by chemistry climate models and observations suggest that the estimation of NO-production by auroral forcing is overestimated during quiet times and underestimated during active time. This thesis provides an intercomparison of different auroral forcing estimates. We compare fluxes from the Total energy detector (TED) onboard the NOAA Polar Orbiting Environmental Satellites (POES) and Meteorological Operational satellite (MetOp) and sensor for precipitating particles (SSJ) from Defense Meteorological Spacecraft Program (DMSP). The data, taken over the year 2010, was sorted by the daily Kp and evaluated as function of geomagnetic latitude and magnetic local time. Discrepancies are evaluated in respect to geographical bias, potential spacecraft charging, as well as the detector's pointing directions relative to the magnetic field. Inside the auroral oval, for the dayside MLT sectors, the DMSP/SSJ instrument observed consistently higher electron fluxes than the POES/TED detectors, independent of Kp level. The shape of the energy flux spectra was evaluated in respect to Maxwellian, Exponential or Power law distributions. The best fit was shown to depend mostly on latitude, implying the magnetospheric origin of the electrons mainly decide the shape of the spectra. Furthermore, daily ionisation rate estimates implemented in the Whole Atmosphere Community Climate Model (WACCM) and estimated by the Atmospheric Ionization Module Osnabrück (AIMOS) were compared with the flux observations in mind. The data from the entire year of 2010, was estimated in WACCM's standard geographical grid and sorted by daily Kp level. Discrepancies were evaluated as functions of Kp, geographic latitude and longitude, with previous studies and our flux results as reference. WACCM underestimated the ionisation rate during periods of high geomagnetic activity, while overestimating during periods of weak activity compared to AIMOS.

Contents

1 Introduction

Figure 1.1: Picture taken of the Aurora over Andøya, October 2020. credit: Kjartan Olafsson

The aurora has illuminated observers for millennia with its dancing colours, high up in the sky in the polar regions of the Earth. The aurora has been part of myths, folklore, and legends for people living in the auroral regions. In this day and age, with modern scientific methods, instruments and techniques, much is understood of how the aurora is produced alongside its impact on the atmosphere. Energetic particles, originally originating from the Sun, are guided into the atmosphere by Earth's magnetic field, depositing their energy in the lower thermosphere (>100 km). The resulting ionisation, dissociation, and excitation of the atmospheric constituents produce the green, red, and blue lights which makes up the visible Aurora. Moreover, the last 50 years it has been shown that the auroral electrons (1-30 keV) that lights up the polar sky, also causes chemical changes in the upper atmosphere [*Crutzen et al.*, 1975; *Swider and Keneshea*, 1973; *Weeks et al.*, 1972]. Essentially, the ionisation initiates a series of chemical reactions producing NO_x and HO_x gasses in the lower thermosphere, and mesosphere, respectively [*Sætre et al.*, 2004; *Zawedde et al.*, 2016; *Sinnhuber et al.*, 2012; *Funke et al.*, 2014; *Andersson et al.*, 2012]. Of particular interest is the production of NO_x due to the long lifetime (months) in the polar winter darkness. That implies, that NO_x gasses will not be confined to the regions they are produced, but the molecules will be transported both horizontally and vertically [*Smith-Johnsen et al.*, 2017]. If trapped inside the winter polar vortex, the NO_x gasses will be transported downward from the lower thermosphere to the stratosphere by the residual circulation which has a descending branch over the winter pole [*Smith-Johnsen et al.*, 2017]. Here the NO_x gasses can deplete the stratospheric ozone through catalytic reactions. Ozone plays a major role

in the stabilisation of Earth's climate system. It is known for absorbing dangerous UV radiation from the Sun, stopping it before it can reach us at the surface. Ozone is also a green house gas absorbing and emitting infrared radiation. The depletion of the ozone layer, can therefore impact both the temperature profile and the dynamics of the atmosphere.

To quantify these effects, the flux of low energy electron precipitation into the lower thermosphere needs to be determined. Both spaceborne particle detectors and UV cameras are used to estimate the global input. Moreover, the empirical data has been the foundation for ionisation rate estimates that are applied in chemistry climate models to study the direct and indirect effect of energetic particle precipitation (EPP). In this context, some important question arises: What is the energy input associated with the auroral electrons? How to accurately parameterise the auroral electron fluxes? How to characterise the energy spectra of the auroral electrons? And how realistic are the parameterisations and characterisations compared to the observed auroral electrons? The Whole Atmosphere Community Climate Model (WACCM) is a model that tries to model the effects of EPP. Similar to most atmospheric climate models, it predicts EPP based on a geomagnetic activity index (the Kp-index). However, doubts regarding its ability to produce the correct levels NO for various geomagnetic activity have been raised [*Hendrickx et al.*, 2018; *Smith-Johnsen et al.*, 2018, 2022]. There appear to be a consensus that WACCM underestimates the lower thermospheric NO levels in periods of high geomagnetic activity, while it overestimates the NO levels during periods of low activity. The research questions addressed in this thesis are therefore as follows:

- Do the available spaceborne particle detectors observe the same flux of auroral electrons? And do they observe the same flux distribution dependent om magnetic local time and latitude?
- How does the auroral electron fluxes vary in terms of geomagnetic activity?
- Is this accurately parameterised in current chemistry-climate models ?

The scope of this study is to compare the measured auroral electron fluxes and how they vary with Kp observed by the Total Energy Detector (TED) on board the National Oceanic and Atmospheric Administration (NOAA)/Polar Orbiting Environmental Satellite (POES) and the European Organisation for the Exploitation of Meteorological Satellites (EUMETSAT)/Meteorological Operational Satellite Program of Europe (MetOp), with the fluxes observed by the SSJ instruments onboard the Defense Meteorological Satellite Program (DMSP) spacecrafts. Furthermore, a comparison between the two ionisation rate estimates applied in atmospheric models are performed. WACCM includes ionisation rates scaled by the geomagnetic activity index, Kp. The Atmospheric Ionization Module Osnabrück (AIMOS) is a semi-empirical ionisation rate estimate, partly scaled by Kp, that is used as input in several chemistry-climate models.

2 Theory:

2.1 The Sun and solar activity

The Sun is Earth's main source of energy, it's "power plant", and ultimately what makes the Earth inhabitable. The energy of the Sun can be categorised into two components. The main component of the energy is in the form of electromagnetic energy, called solar radiation. An estimate of the spectral energy distribution of solar radiation received by Earth's surface per unit area can be obtained through Planck's law/function. [*Bohren and Clothiaux*, 2008]

The other component of the energy transported to the Earth is in the form of kinetic energy, called the solar wind. The solar wind is a magnetised collisionless plasma, which drives particles at supersonic speeds, 500 km/s [*Baumjohann and Treumann*, 1996]. It is the component of most interest in the field of Space physics, where the effects of the solar wind particles on Earth's climate, the atmosphere and instruments are important areas of research.

2.1.1 Solar properties

The Sun is a ball of gas which lies in the centre of our solar system. It is classified as a yellow dwarf star and consists mostly of hydrogen, ∼70%, and helium, ∼27%, as well as some heavier elements like oxygen, carbon, neon and iron. It is held together by its own gravity [*NASA*, 2021], and accounts for over 99% of the total mass in our solar system [*Woolfson*, 2000]. It's radius is around 109 times the Earth's at 696,340 km, and its volume 1.3 million times larger than the Earth. The Sun's surface temperature is approximately 5,778 K, while its core is about 15 million Kelvin.

Figure 2.1 shows the regions of the Sun. It is divided into six zones, three interior and three exterior. The three interior zones are the core, the radiative zone and the convection zone. Then we have the photosphere, the chromosphere and the corona as the exterior zones. The photosphere is the visible surface, and is where most of the solar energy escapes, in the form of sunlight. Material leaving the corona, the Sun's outer atmosphere, becomes the solar wind [*NASA*, 2021].

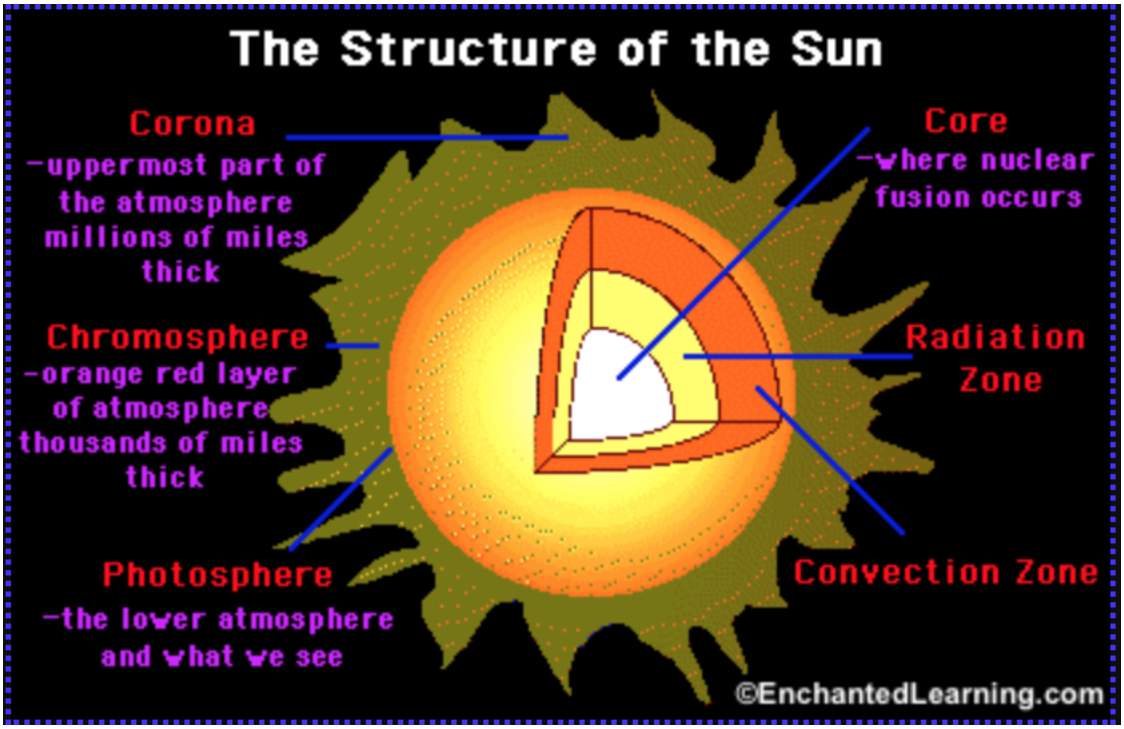

Figure 2.1: Illustration of the structure of the Sun, from [https://www.enchantedlearning.com/subjects/astronomy/sun/sunstructure.shtml]

The Sun's rotation is dependent on the latitude since it's not a solid rigid body. At the equator, the Sun's rotation is about 25 days, while near the poles it is around 36 days [*Zell*, 2017]. The Sun has a complex magnetic field, resembling a dipole, which is generated by the Sun's dynamo. The difference in rotation leads to a distortion of the magnetic field. In Figure 2.2 we can see the evolution of the magnetic field due to the distortion. At first, the magnetic field is dipolar or poloidal (see Figure 2.2.a). However, over time, due to the faster rotation at equator, the field lines are stretched out around the centre, resulting in twisted magnetic flux ropes (see Figure 2.2.b/c.) [*Babcock*, 1961].

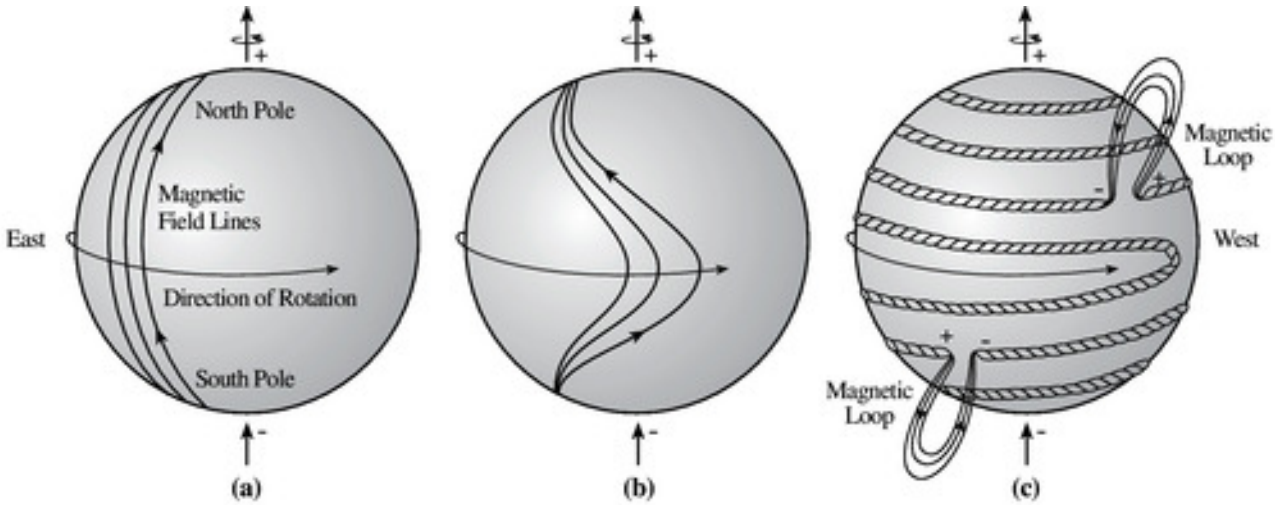

Figure 2.2: Evolution of the Sun's magnetic field due to the latitudinal dependent rotation, adapted from [Babcock, 1961]

The distortion causes a change in solar magnetic activity, which increases as the field lines get more and more twisted until it reaches the solar maximum. Afterwards the field lines eventually relax back to a dipole with inverted polarity and solar minimum. This change can be described by the solar cycle, where the polarity switch happens approximately every 11 years. For solar magnetic configuration, a complete solar cycle, the time it takes for it to reach its initial state, is 22 years.

2.1.2 Sunspots

Sunspots are a phenomena that temporarily appears on the Sun's photosphere, appearing as dark regions. Figure 2.3 shows an image of sunpots on the Sun's surface. The regions appear dark since they are of lower temperature than their surroundings. They typically consists of a dark part, *umbra*, surrounded by a lighter part, *penumbra*. Sunspots can last anywhere from a few days to a couple of months until they decay. Furthermore they also contract and expand while they move around the Sun's surface, with sizes ranging from 16 to 160 000 km in diameter. The average sunspot is around the size of the Earth.

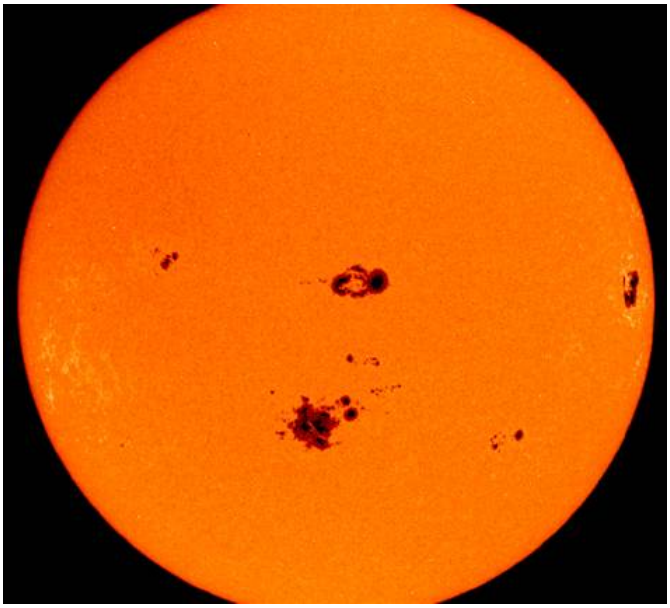

Figure 2.3: Picture of sunspots on the Sun's surface, courtesy of NASA

Sunspots usually appears in pairs with opposite magnetic polarity, and are a consequence of the previously mentioned twisting of the Sun's magnetic field lines. Magnetic flux tubes from the Sun's convective zone projects through the photosphere within active regions of the Sun. Active regions are defined as temporary regions in the Sun's atmosphere with strong and complex magnetic field. This strong magnetic field then inhibits the convection of plasma in the photosphere. Meaning there is less new flow of hot plasma coming from the Sun's interior, which results in the darker and colder region known as sunspots.

The sunspot activity quantifies the solar cycle, where solar maximum corresponds with to the highest sunspot number and solar minimum to the lowest. Sunspots usually forms around high latitudes at solar minimum, and move towards equator at solar maximum.

Coronal mass ejections (CME) and solar flares are large explosions/eruptions on the photosphere. They occur near and are closely related to sunspots. As sunspots are characterised as regions of intense magnetic activity, the field lines can be stressed, by magnetic pressure, to the point they reconnect with field lines of opposite polarity and reconfigure. This is called magnetic reconnection, a process where magnetic energy is converted (See section 2.2.3). The result is a sudden intense eruption of electromagnetic radiation, known as a solar flare. Solar flares affect all layers of the Sun's atmosphere. The same energy release can also accelerate plasma in the corona, leading to an ejection of solar mass from the Sun's atmosphere, known as a CME. CMEs are the largest scale eruptive phenomenon in the solar system [*Chen*, 2011]. CMEs are related to geomagnetic storms (See section 2.3)

2.1.3 Coronal holes

Coronal holes are regions of the Sun with colder and less dense plasma [*Zirker*, 1977]. They are characterised by open magnetic field lines that extend out in interplanetary space [*Cranmer*, 2009]. The plasma can then flow along the field lines out in space, escaping the Sun more easily than elsewhere. This results into streams of relatively faster solar wind (>600 km/s), commonly called high speed streams/fast solar wind [*Marsch*, 2006; *Baumjohann and Treumann*, 1996]. When the faster solar wind interacts with the relatively slower one, a compression region forms, Co-rotating interaction region (CIR). CIRs can result in geomagnetic storm/disturbances (see section 2.3).

Coronal holes depend on the solar cycle, both in terms of number and location on the solar disk. As the cycle reaches towards the solar maximum, coronal holes move closer and closer to the poles. The population of coronal holes decreases under solar maximum, until the polarity of the magnetic field lines on the Sun switch. New coronal holes then appear near the poles, growing in size and extending farther away from the poles until solar minimum. Coronal holes and CIRs are the primary sources of geomagnetic disturbances during solar minimum [*Cranmer*, 2009].

Coronal holes are visible to the naked eye, but first appeared on X-ray images as dark areas on the Sun. Figure 2.4 shows an x-ray image of coronal holes

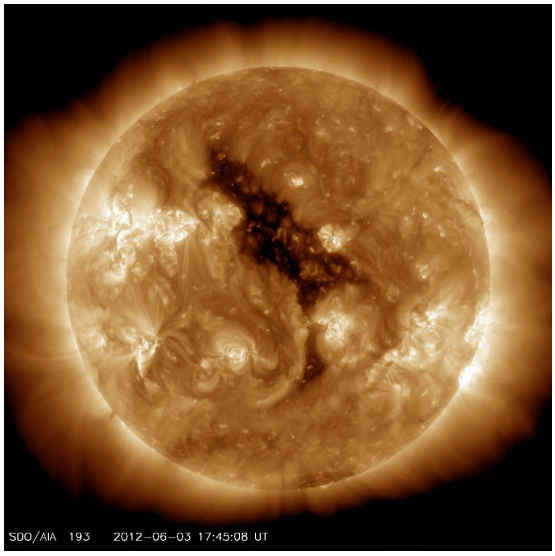

Figure 2.4: Soft x-ray images of coronal holes 2012, credit NASA/AIA [https://www.nasa.gov/multimedia/imagegallery/image_feature_2268.html]

2.1.4 Solar Wind

The solar wind is highly conductive plasma emitted from the Sun. The plasma escapes radially out from the Sun's atmosphere (the corona) as particle streams with hypersonic speeds, around 500 km/s, and into the interplanetary space [*Baumjohann and Treumann*, 1996]. The 500 km/s value is the most probable velocity value of the solar wind and the

solar wind's velocity ranges typically between 300-1400 km/s near Earth [*Baumjohann and Treumann*, 1996]. Streams with velocities less than 400 km/s are considered low speed, while above 600 are considered high speed. Typical values for electron density and temperature in the solar wind near Earth is $n_e \approx 5cm^{-3}$ and $T_e \approx 10^5 K$. The solar wind continuously blows out of the corona and reaches far beyond 1 AU.

The solar wind is for the most part made up by electrons and protons, with a about 5 % helium [*Baumjohann and Treumann*, 1996]. The magnetic field of the Sun is embedded in the solar wind. It is frozen in to the plasma because of the high conductivity, and therefor gets drawn outward into the interplanetary space. This is called the interplanetary magnetic field (IMF). The IMF is approximately 5nT.

As mentioned, there is two types of solar wind, fast solar wind and slow solar wind. The fast solar wind originates from large coronal holes, where the open magnetic field lines extends into interplanetary space [*Marsch*, 2006; *Ohmi et al.*, 2004; *Zirker*, 1977]. Here the plasma is confined by magnetic field lines that confine and transport it into the so called coronal funnels [*Marsch*, 2006]. The solar wind flows out of these funnels at heights above the photosphere [*Marsch*, 2006]. The fast solar wind is associated with high geomagnetic activity and the Kp-index [*Zirker*, 1977]. The slow solar wind is thought to originate from two regions, from close coronal loops and rapidly diverging open flux tubes which are rooted just inside the coronal hole boundaries [*Ohmi et al.*, 2004]. CMEs is also considered a type of solar wind [*Marsch*, 2006], as discussed earlier they are related to sunspots.

2.2 Magnetosphere

The magnetosphere is the region around a planet where the planet's magnetic field dominates. In the near-Earth space environment this is where the geomagnetic field is stronger than the IMF. The interaction between the geomagnetic field and the solar wind and IMF is key to understanding how solar activity affects the Earth. The magnetosphere and its dynamics is the result of this interaction.

2.2.1 The Geomagnetic field

The origin of Earth's magnetic field, or the geomagnetic field, is not quite fully understood. However it is believed to be generated by the dynamo of melted iron (and nickel) in the core. The flow of liquid metal in the core creates electric currents which then generates the magnetic field. This is known as the dynamo theory. It gives a mechanism where a celestial body (Earth, Sun etc.) can generate a magnetic field and maintain it over astronomical times. The principal sources of power for this dynamo is believed to be the energy released by the solidification of its core [*Russell*, 1993].

The geomagnetic field is quite inhomogenous, due to magnetic irregularities of the Earth's crust and mantle [*Baumjohann and Treumann*, 1996]. These inhomegeniteis can be accounted for by an expansion of the geomagnetic field into multipoles. However at large but not too far distances from Earth's centre, the field can be approximated and modelled as a dipole field. This dipole model is only valid for low L-shell values, the approximation breaks for

higher L values. The L-shell value is the ratio between the radial distance to a field line in the equatorial plane, r_{eq} of the Earth and the Earth's radius, $R_E = 6371km$

$$L = \frac{r_{eq}}{R_E} \tag{1}$$

[*Baumjohann and Treumann*, 1996]. As seen in Figure 2.5 the magnetic field line loops around the Earth, diverging near the geographical south pole and converging near the geographical north pole. Meaning, the magnetic north pole roughly corresponds with the geographic south pole and the magnetic south pole roughly corresponds with the geographic north pole. Its axis is sightly tilted from the rotational axis of the Earth at about 9.69 degrees [*Laundal and Richmond*, 2017].

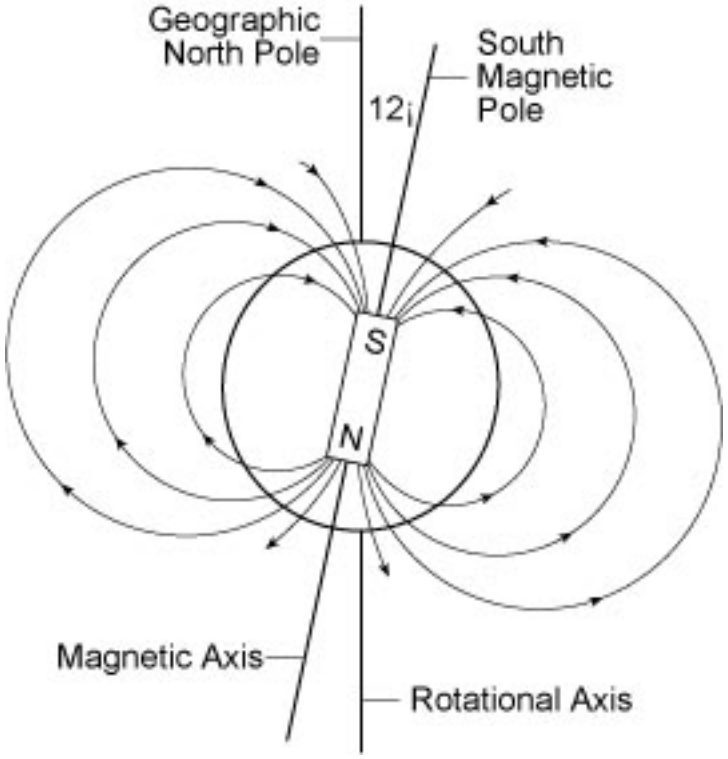

Figure 2.5: Illustration of Earths dipole magnetic field, from `https://ase.tufts.edu/cosmos/view_picture.asp?id=326`

2.2.2 Magnetic coordinates

In this thesis, data is used from low Earth orbit (LEO) satellites. Meaning well inside the region appropriate for the dipole approximation model. Therefore, it is common to use a coordinate system that is defined by the axis of the geomagnetic dipole. A specific point on a dipolar field line is defined by a distance and angle. The angle is between the point and the largest distance in equatorial plane [*Baumjohann and Treumann*, 1996; *Laundal and*

Richmond, 2017]. In fig 2.6 the distance and angle are represented by r and λ respectively. λ is called magnetic latitude (MLAT), and is given by:

$$\lambda = \cos^{-1}(\sqrt{\frac{r}{r_{eq}}}) \tag{2}$$

where r_{eq} is the same as earlier defined in reference to the L-shell value.

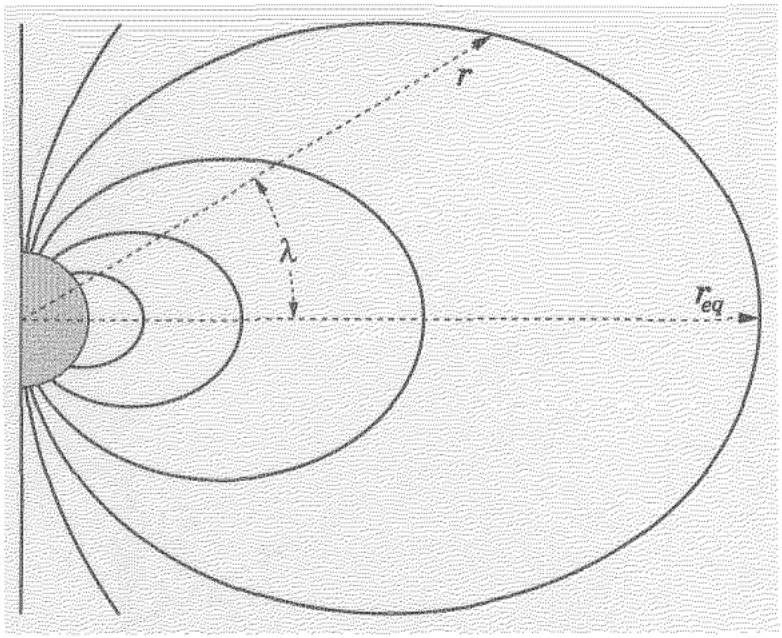

Figure 2.6: Illustration of magnetic latitude, adapted from [Baumjohann and Treumann, 1996]

Despite LEO satellites being inside the dipole approximation, better accuracy and common practice is to use the corrected geomagnetic latitude (CGMLAT)[*Laundal and Richmond*, 2017]. CGMLAT is defined in the terms of line tracing with the International Geomagnetic Reference Field (IGRF) [*Laundal and Richmond*, 2017]. CGMLAT point x is found through the location of the intersection between point x and the centered equatorial dipole plane and dipole mapping it to 1 Earth radius[*Laundal and Richmond*, 2017]. CGMLAT is given by:

$$\lambda_{cgm} = \pm\sqrt{\frac{R_E}{R_{E+h_{eq}}}} \tag{3}$$

where R_E is the radius of the Earth and h_{eq} is the height of the centered dipole equatorial plane.

Due to the interaction with the solar wind (which will be discussed more in detail in section 2.2.3) Earth's magnetic field configures into a comet-like structure, fixed with

respect to the Sun. The Earth spins inside this structure. Since the magnetic longitude (MLON) is fixed with respect to Earth, it is appropriate to introduce a magnetic local time (MLT), in order to organise data with respect to the position of the Sun [*Laundal and Richmond*, 2017; *Vegard*, 1912, 1917]. MLT = 0 is midnight and in the anti-sunward direction, while MLT = 12 is noon and in the sunward direction. MLT 6 and 12 represents dawn and dusk, respectively. The magnetic local time can be seen as an extension of the local solar time on Earth. The magnetic noon is always found where the Universal time (UT) is noon. A commonly used definition of MLT is the hour angle from the midnight magnetic meridian, positive in the magnetic eastward direction. Here 1 hour MLT is equal to 15° magnetic longitude, and the magnetic meridian can be defined as the meridian 180° magnetic longitude away from the subsolar point [*Laundal and Richmond*, 2017].

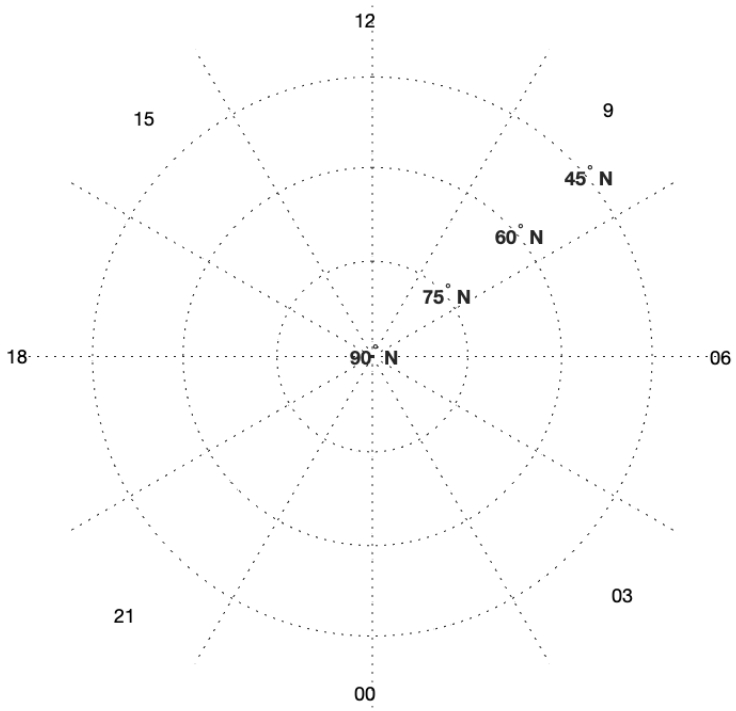

Figure 2.7: Illustration of a MLT grid

2.2.3 Interaction between solar wind and the magnetosphere

The solar wind travels with supersonic and super-alfvenic velocities, which means when it hits an obstacle, it will be subjected to shocks [*Baumjohann and Treumann*, 1996]. A shock is a type of propagating disturbance that moves faster than the speed of sound of the medium it propagates in. It is characterised by abrupt and nearly discontinuous changes

in temperature, pressure and density of the medium [*Anderson*, 2001]. A defining criteria for a shock, is the change of velocities from supersonic to subsonic.

Obstacles that can cause shocks in the solar wind are for example planets, comets and asteroids. However, the obstacle of most interest is the extended magnetospheres for magnetised planets. The magnetosphere extends the cross section of a planet by large factor. For Earth's magnetosphere, this factor is about 150 [*Baumjohann and Treumann*, 1996]. This then generates Earth's extended Bow shock when hit by the Solar wind, illustrated in Figure 2.8.

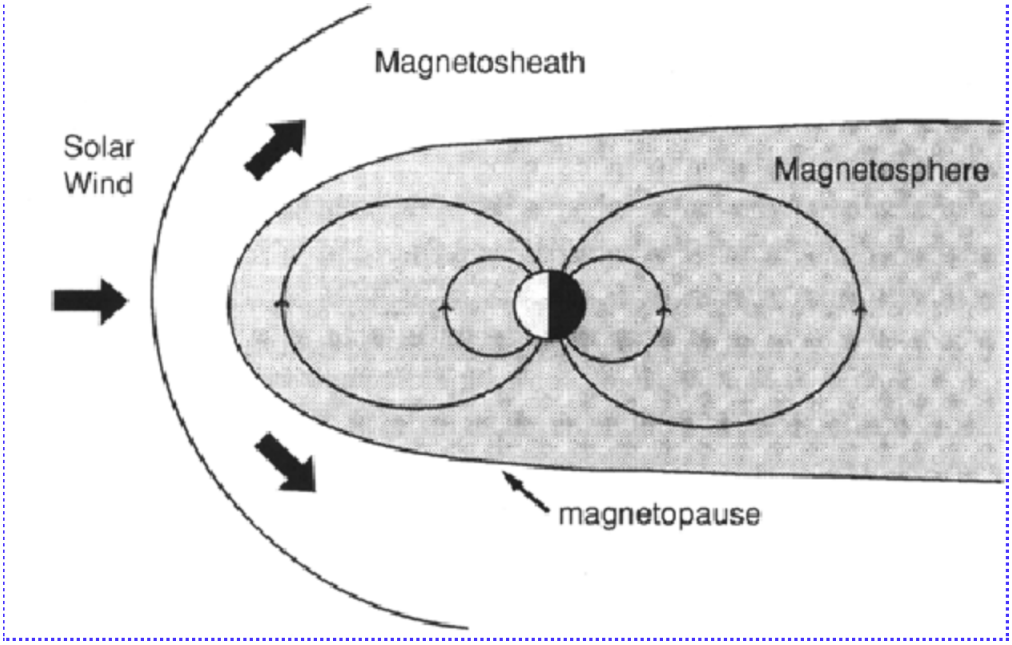

Figure 2.8: Illustration of Earth's bow shock, magnetosheath etc, Cravens 1997 [http://www.physics.usyd.edu.au/~cairns/teaching/lecture13/node2.html]

The size and shape of the magnetosphere is decided by its interaction with the solar wind. The balance between the dynamic pressure of the solar wind and the pressure exerted by the magnetosphere, mostly by the geomagnetic field, determines the size of the magnetosphere. [*Russell*, 2000]. The Earth's magnetic field strength is around 30 nT at 10 Earth radii. The interaction with the solar wind increases this by more than double on the dayside, so the pressure exerted by the magnetic field is around 2 nPa. This pressure is then balanced by the dynamic pressure exerted by the flowing solar wind plasma, which also about 2 nPa [*Russell*, 2000]. The shape of the magnetosphere is also caused by the drag of the solar wind. Mainly caused by reconnection, where the magnetic field of the IMF links with the magnetic field of the Earth [*Russell*, 2000]. At the dayside, the solar wind pressure compresses the field, while on the night side it stretches it out into a long tail called the magnetotail [*Baumjohann and Treumann*, 1996]

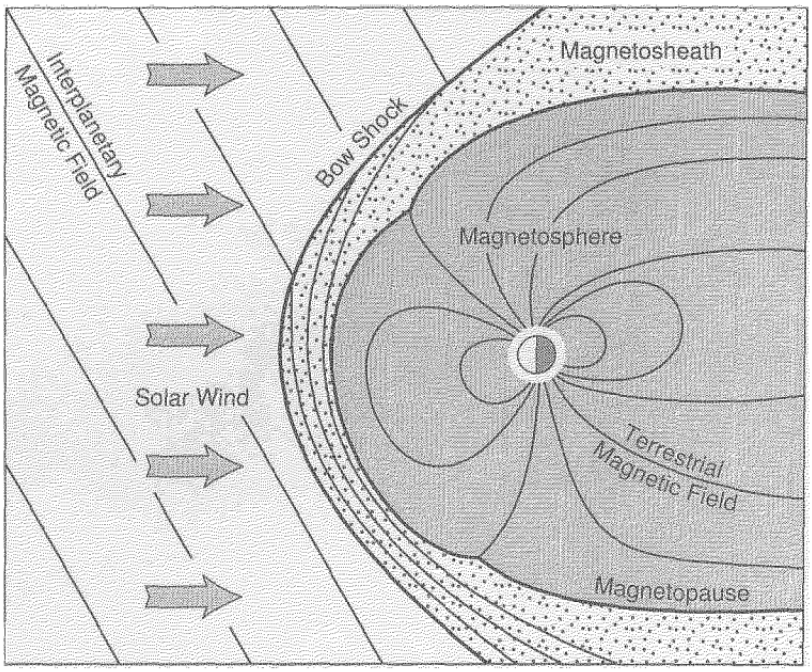

Figure 2.9: Topology of the Solar Terrestrial environment, adapted from [Baumjohann and Treumann, 1996]

The bow shock creates an extended region of subsonic plasma behind it, the magnetosheath. In the magnetosheath the shocked plasma from the solar wind can't easily penetrate Earth's magnetic field and therefore is mostly deflected around it. As seen in Figure 2.9, it will instead compress Earth's magnetic field on the dayside. A narrow boundary is then formed between the solar wind and Geomagnetic field, the magnetopause [*Baumjohann and Treumann*, 1996]. The magnetopause is the forementioned region where the pressure exerted by the geomagnetic field is balanced by the pressure of the solar wind. An interesting feature to note, is that in the magnetopause, the charges will travel around on opposite sides, leading to the magentopause currents (see Figure 2.10) [*Kelley*, 2009]

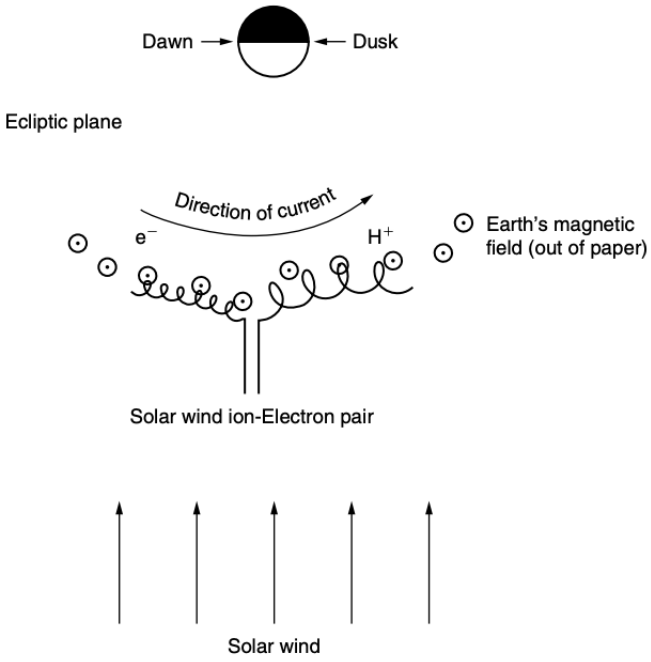

Figure 2.10: Illustration of the formation of the Magnetopause current, adapted from [Kelley, 2009]

While most of the solar wind plasma will be deflected by the geomagnetic field, a process called magnetic reconnction allows for both energy and plasma transfer between the solar wind and magnetosphere. The simplest way to describe magnetic reconnection is through the Sweet-Parker reconnection model, an illustration of which can be seen in Figure 2.11. The model assumes the plasma as a incompressible fluid, meaning there can be no density build up in the reconnection region. It views reconnection as a static momentum balance. Therefore it can be consider as an energy conservation model, where the electromagnetic energy stored in the magnetic fields is converted to kinetic energy. The energy conversion rate is given by the flow of electromagnetic energy into the reconnection region. The inflow is therefore coupled with the reconnection outflow. The outflow is limited by the Alfvén velocity, meaning there is a limit on how fast reconnection can occur under the Sweet-Parker model. The Sweet-Parker model makes no assumption on what happens inside the diffusion/reconnection region (see Figure 2.11).

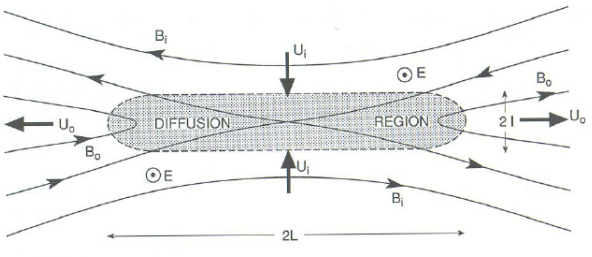

Figure 2.11: Illustration of Sweet-Parker reconnection, adapted from [Kivelson and Russell, 1995]

In 1961, James Dungey proposed the Dungey cycle [*Dungey*, 1961], a model explaining how the interaction between the solar wind and Earth's magnetic field drives magnetospheric dynamics through reconnection [*Milan et al.*, 2007] [*Dungey*, 1961]. Magnetic field lines are always closed [Gauss' law], however in the Dungey cycle the concept of "open" and "closed" magnetic field lines are introduced. A "closed" field line is one with both its ends attached to the Earth(poles), while an "open" field line only has one footpoint on Earth and The other end is then part of the IMF.

The Dungey cycle, illustrated in Figure 2.12, begins when the IMF approaches Earth's magnetic field. The field lines of the IMF and Earth's magnetic field are anti-parallel. Reconnection then occurs at the subsolar magnetopause, which opens up the field lines (1-2). This opening is called dayside reconnection. The footpoints on Earth lies in the ionosphere, where conductivity is high and field line mobility low, due to friction from collisions with local ions (Ions are not assumed to be frozen-in in the ionosphere [*Kelley*, 2009]). The open field lines are then dragged antisunward and curved by the solar wind forming an extended magnetotail (3-6) [*Dungey*, 1965] [*Cowley*, 1991] [*Milan*, 2004]. The end points in the ionosphere will also be transported across the polar cap, to the night side, when the magnetic curvature force exceeds the friction from the ions (3-6) [*Baumjohann and Treumann*, 1996] .

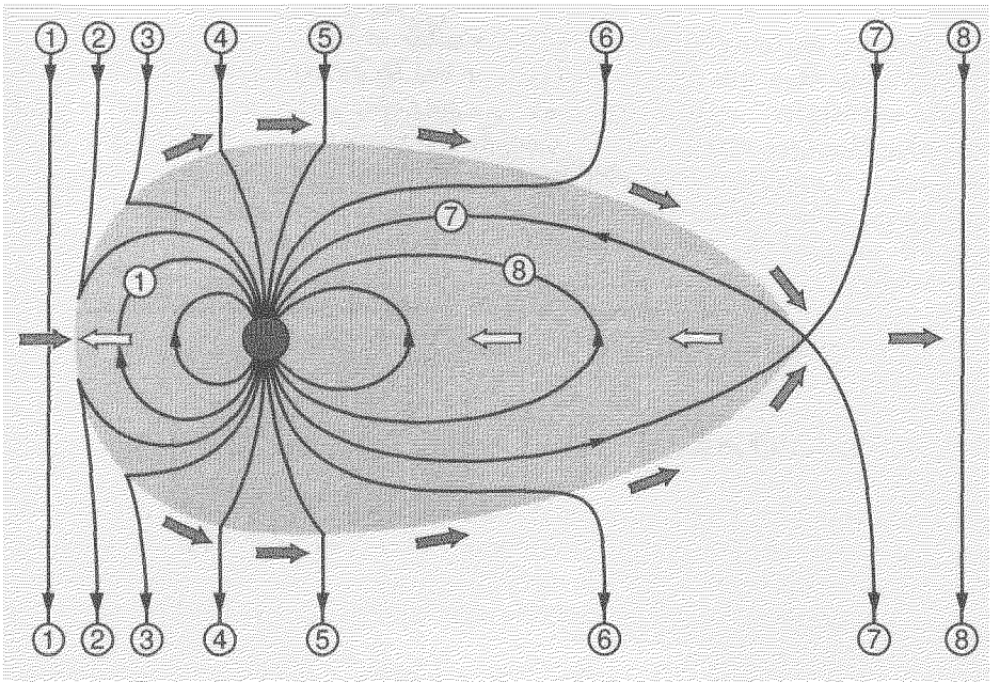

Figure 2.12: Illustartion of the Dungey cycle, adapted from [Baumjohann and Treumann, 1996]

On the night side, around 100-200 Earth radii, the two open field lines from each hemisphere will meet again and reconnect. Forming a closed but stretched out terrestrial field line in the magnetotail and an open solar wind field line down tail of the magnetosphere (7-8). The IMF and Earth's magnetic field is then disconnected, and the solar wind plasma is transported into the magnetosphere. The stretched field line will, due to magnetic tension, relax and force towards to the Earth into a more dipole structure (8 in the shaded area). The field lines are then eventually transported to the dayside, completing the cycle [*Baumjohann and Treumann*, 1996] [*Milan et al.*, 2007]

Since the geomagentic field is northward, the Dungey cycle depends on the IMF anti-parrallel component, B_z, being negative. Meaning in other words, the Dungey cycle depends on a southward IMF. So as long as the IMF is southward the Dungey cycle can be repeated. The intensity of the southward IMF, as well as the solar wind speed, will decide the rate of reconnection in the magnetopause. Dungey originally proposed that the rates of dayside and nightside reconnection were equal. However, the nightside reconnection is limited and there is lag between the two [*Milan et al.*, 2007]. This leads to a varying amount of open and closed field lines which results in the expanding contracting polar cap paradigm [*Russell*, 1972; *Cowley and Lockwood*, 1992]. It should also be noted that in high latitudes reconnection can still occur when the IMF is northward[*Kelley*, 2009]

The Dungey cycle is a simple model, however it has helped explain previously known and observed features of Earth's magnetosphere [*Milan et al.*, 2007]. For example the two cell convection pattern of plasma in the ionosphere [*Cowley and Lockwood*, 1992; *Kelley*, 2009], which is both influenced by the Northward-Southward component, B_z, and East-

West component, B_y, of the IMF. For s southward IMF the convection patterns are more pronounced, while the B_y component influences symmetry [*Kelley*, 2009].

2.2.4 Regions within the magnetosphere:

The magnetosphere is divided up into different regions based on the characteristics of the different particle and plasma populations found there. Fig 2.13 gives an overall view of the plasma regions and associated currents.

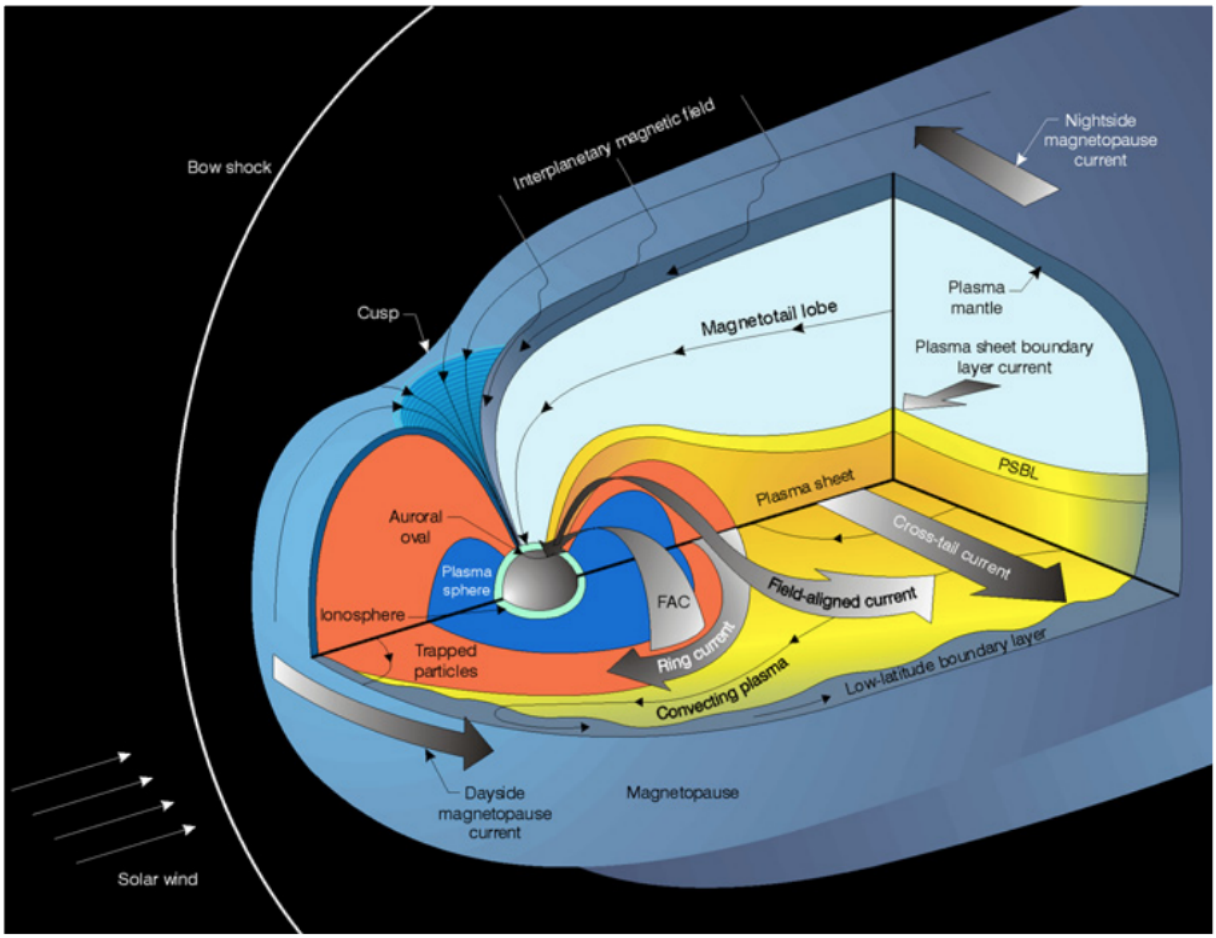

Figure 2.13: The magnetospheric cavity; it's plasma regions and associated currents

Plasmasphere:

The plasmasphere is the inner region of the magnetosphere. The plasmespheric environment is characterised by dipolar-like magnetic field lines. It consists of cold dense plasma, with particle energies of around 1 eV and density of several $10^3 cm_{-3}$ [*Baumjohann and Treumann*, 1996]. The plasmasphere is made up of light ions, mainly H^+ but also some helium and oxygen ions, that lie on closed magnetic flux tubes that corotates with the Earth [*Moffett et al.*, 1989]. At high latitudes the lighter ions and hydrogen atoms can

escape gravity, guided by the dipolar magnetic field lines. filling up the plasmasphere during daytime. At night, the lower latitude plasmasphere is depleted through fast recombination. However, at high latitudes, recombination is slow and the plasma is persistent. Leading to the upper plasmasphere to be filled up on average with cold dense proton plasma.

The plasmasphere located where the electric field created due to corotating plamsa dominates over electric fields of magnetospheric origins [*Kelley*, 2009]. A comparison between the ionospheric dynamo, corotation, and magnetospheric electric fields found that the corotation field is strongest at midlatitudes and diminishes towards the poles [*Mozer*, 1973]. The boundary of the plasmasphere is called the plasmapause. It is characterised by sharp plasma density gradient and was first discovered by *Gringauz* [1963] and *Carpenter* [1963]. It can be seen as the boundary between the corotating and convection dominated regions of the equatorial magnetosphere [*Baumjohann and Treumann*, 1996]. The boundary depends on geomagnetic activity and MLT, and lies between 3-7 Earth radii [*Chappell et al.*, 1970; *Doe et al.*, 1992]

Radiation Belts:

The radiation belts, or Van Allen belts, were discovered in 1958 by instruments on the Explorer 1 [*Van Allen et al.*, 1959]. It was the first major scientific discovery of the space age, and can be considered as the start of modern space physics [*Li and Hudson*, 2019]. The radiation belts consists of two regions, the inner and outer belt, which closely follows the geometry of the magnetic dipole field [*Baumjohann and Treumann*, 1996], as seen in Figure 2.14. The regions are populated by highly energetic charged particles, which are trapped by Earth's dipole field [*Horne et al.*, 2005]. Protons are confined to the inner belt, due to the large gyroradii [*Li and Hudson*, 2019]. The electrons exhibit a two belt/zone structure, due to wave particle interactions which causes pitch angle scattering losses to the atmosphere [*Li and Hudson*, 2019; *Ganushkina et al.*, 2011]. The inner region is quite stable and is typically located between 1.2 and 3 Earth radii [*Ganushkina et al.*, 2011; *Lyons and Thorne*, 1973], coexisting with the plasmasphere. It consist mainly of ions with energies between 0.1-40 MeV. The outer belt extends from about 3 to 7 Earth radii [*Ganushkina et al.*, 2011], and consists mostly of electrons with energies from 0.1-10 MeV. The outer belt is not as stable as the inner belt, and its electron fluxes are highly dynamic and varying with both space and time [*Ganushkina et al.*, 2011]

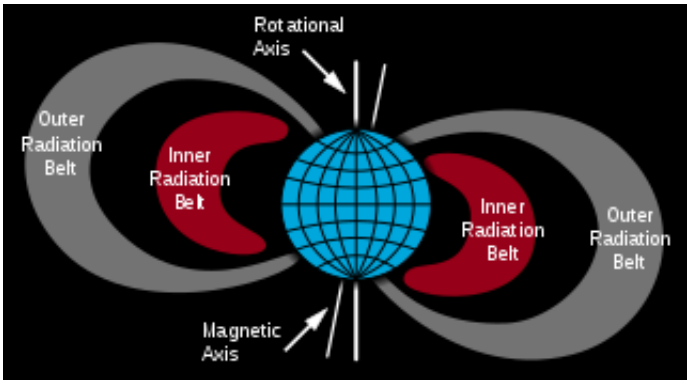

Figure 2.14: Illustration the inner and outer regions of the radiation belts, adapted from [https://en.wikipedia.org/wiki/Van_Allen_radiation_belt]

The charged particles trapped in the radiation belts are governed by Earth's magnetic field. When approaching Earth the field lines will converge into both hemispheres. In such configuration, the charged particles will move in three ways due to the laws of electromagnetism *Baumjohann and Treumann* [1996]: 1) They will gyrate around field lines. 2) They will bounce/oscillate back and forth between the two hemispheres, turning at the magnetic mirror point in each hemisphere. 3) They will drift around the Earth in constant paths of magnetic strength[*Baumjohann and Treumann*, 1996]. Each motion has an associated adiabatic invariant. For the gyration motion it is the magnetic moment, which states that for a surface encircled by a gyrating particle the magnetic flux is constant. The bounce motion is associated with the longitudinal invariant, Where a charged particle will be reflected from the area of strong magnetic field and oscillate in the field with a certain bounce frequency. Its motion is almost periodic if the field doesn't change during its bounce period [*Baumjohann and Treumann*, 1996]. Lastly the drift motion is associated with the drift invariant. These invariants cannot be assumed to always be constant with time and space, as they rely on timescales where the magnetic field is constant or close to it.

The drift of the particles are due to the curvature and gradient of the magnetic field line, as the particles accelerate from the nighttime reconnection region [*Baumjohann and Treumann*, 1996]. Since ions and electrons have opposite charges, they drift in opposite directions around the Earth. Generating a current known as the Ring current (see Figure 2.13).

The particles bouncing between the hemispheres are not all trapped even when the longitudinal invariant is conserved. They can be lost to the atmosphere through collisions with neutrals, if the magnetic mirror points are below 100km altitude [*Baumjohann and Treumann*, 1996]. A particle's pitch angle is key to determine if it gets lost to the atmosphere. The pitch angle is defined as the angle formed between a particle's velocity vector and the local magnetic field line. A pitch angle of 0° means the particle is travelling parallel with the field, and a pitch angle of 90° is one that mirrors. One can then define a loss cone, seen in Figure 2.15), which contains all the pitch angles for which a particle can reach the atmosphere,

get lost and deposit their energy through particle precipitation.

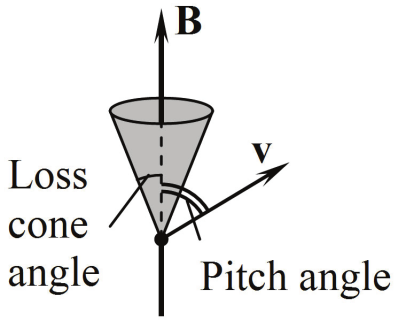

Figure 2.15: Illustration of the loss cone, adapted from Karavaev [2010]

Various magnetospheric processes, like convection and wave-particle interaction, can change a particles energy and pitch angle, leading to diffusion of particles into the loss cone.

Ring Current:

Despite mainly being confined to the inner radiation belt, there is an positive ion component of the outer radiation belt, with energies from 1 keV to few hundred keVs [*Baumjohann and Treumann*, 1996]. These ions are injected into the inner magnetosphere from the solar wind through $E \times B$-drift. Trapped by the geomagnetic field, they start to feel the magnetic gradient and curvature and undergo a azimouthal drift around the Earth [*Baumjohann and Treumann*, 1996; *Daglis et al.*, 1999]. Since both the magnetic drifts is dependent on the particle's charge, the ions and electrons will drift in opposite direction. This creates a current flowing in the westward direction, known as the ring current [*Baumjohann and Treumann*, 1996; *Daglis et al.*, 1999]. The ring current is centred at the equatorial plane and at altitudes of ∼10 000 - 60 000 km. The magnetic field induced by the ring current is noticeable all the way down to Earth's surface and it disturbs the geomagnetic field [*Baumjohann and Treumann*, 1996]. The decrease of the geomagnetic field by the ring current is known as Geomagnetic storms (see section 2.3) [*Daglis et al.*, 1999]. The particles themselves also gyrate, which constitutes their own small currents. The magnetic field of each of these currents are small, however their diamagnetic contribution has to be included to properly represent the magnetic disturbance from the ring current [*Baumjohann and Treumann*, 1996]. The DST index, see section 2.3.3, is a measure of this disturbance.

Plasma sheet and the Magnetotail:

In the magnetotail most of the plasma is concentrated in a sheet like region called the

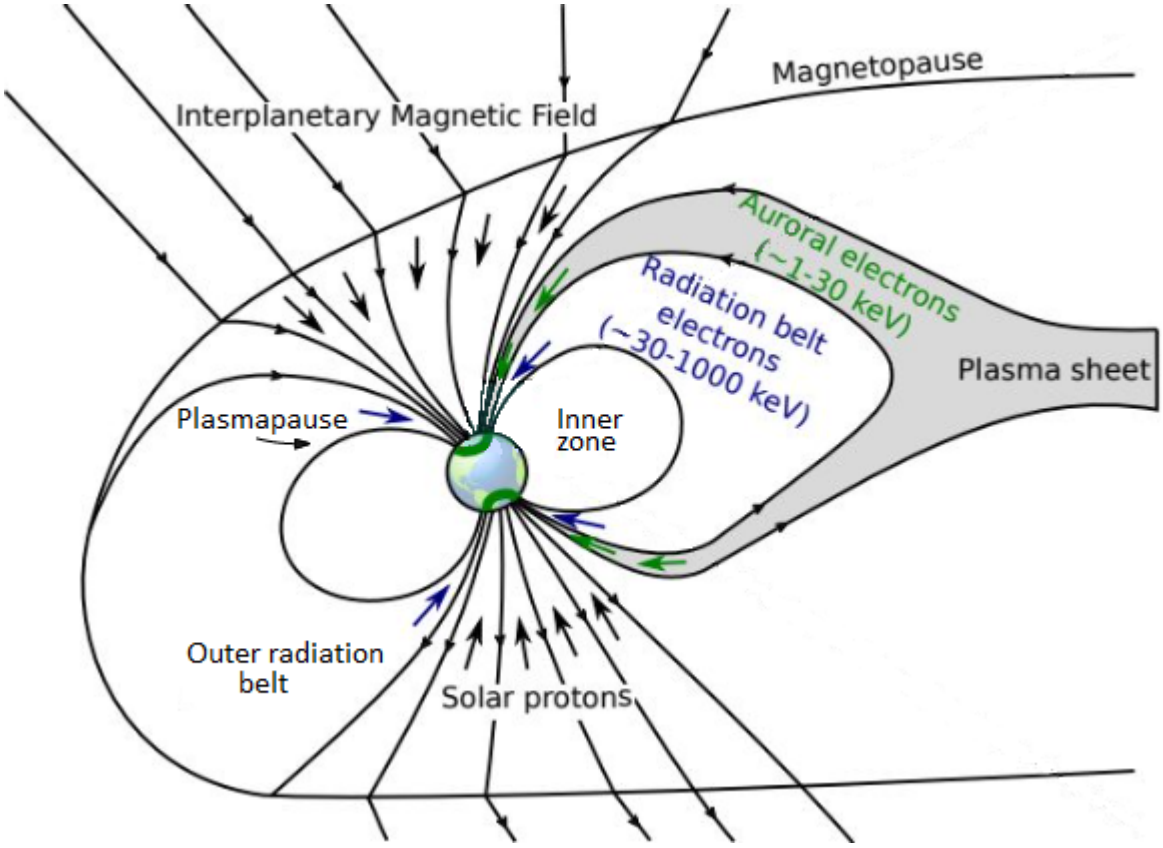

Figure 2.16: Illustration of the dominant particle precipitation zones in Earth's magnetosphere, adapted from [Thorne, 1980]

plasma sheet (see Figure 2.13)[*Baumjohann and Treumann*, 1996]. This sheet of plasma with enhanced electron and ion energy density has been observed at geocentric distances between 15-20 Earth radii, stretching from the dusk to the dawn boundaries of Earth's magnetosphere [*Bame et al.*, 1967]. At around 17 Earth radii, near the midnight meridian, the sheet has often a thickness around 4-6 Earth radii, while towards the dawn/dusk boundaries it is almost double [*Bame et al.*, 1967]. The plasma sheet extends far out with the magnetotail into the nightside [*Baumjohann and Treumann*, 1996; *Bame et al.*, 1967]. The plasma sheet near Earth reaches down to the high latitude ionosphere, where the particles precipitating produces the aurora. average plasma parameters for the plasma sheet are $n_e \simeq 0.5cm^{-3}$, $T_e \simeq 5 \cdot 10^6 K$ and $T_i \simeq 5 * 10^7 K$ [*Baumjohann and Treumann*, 1996; *Bame et al.*, 1967].

In Figure 2.16 the different regions are showed, including their particle populations and precipitation regions. The radiation belts are responsible for the medium energy electrons (30-1000 keV) that precipitate down into Earth's atmosphere at polar latitudes. The plasma sheet, is where the low energy electrons (auroral electrons), responsible for the aurora, precipitate from. These electrons are the focus of this thesis and their energies range from around 1-30 keV.

2.3 Geomagnetic storm

A geomagnetic storm is defined as a major disturbance to Earth's magnetosphere. It occurs when the reconnection rate is strong, meaning the transfer of energy between the solar wind and the magnetosphere is very efficient. This implies that a requirement for a geomagnetic storm is a southward IMF [*Gonzalez et al.*, 1999]. This leads to an enhanced reconnection rate which means more particles are injected into the ring current, making it stronger. The ring current's magnetic field is the opposite of the low-latitude horizontal component of the Earth's magnetic field. An enhancement of the ring current therefore leads to a depression of horizontal component and characterises the main phase of a geomagnetic storm [*Lakhina and Tsurutani*, 2016].

During solar maximum the main driver of geomagnetic storms is CMEs, while during solar minimum its CIRs [*Gonzalez et al.*, 1999]. The largest of the geomagnetic disturbances associated with these storms are due to CMEs. CIRs often have a fluctuating southward-northward component of the IMF, meaning the main phases of CIRs driven storms are weaker and more irregular [*Gonzalez et al.*, 1999]

A geomagnetic storm is often categorised into 3 phases: 1) initial phase, 2) main phase and 3) the recovery phase. The initial phase is characterised by an abrupt increase of Earth's magnetic field (measured by the DST index), where increased solar wind dynamic pressure compresses the dayside magnetosphere. Not all geomagnetic storms have a characterised initial phase. The main phase is the injection of particles into the ring current and enhancement of the ring current's intensity, leading to a depressed geomagnetic field. Lastly the recovery phase is when the injection slows down and the ring current looses energetic particles due to various processes [*Lakhina and Tsurutani*, 2016]. The recovery phase typically starts when the IMF turns less southward [*Gonzalez et al.*, 1999]. Geomagnetic storms are characterised and quantified by several indexes which will be described below.

2.3.1 Kp and Ap index

The Kp-index is a global index based on 3 hour ground-based measurements from magnetometers found at sub-auroral latitudes . They all report an K-index dependent on the geomagnetic activity at its location. The measurements are all calibrated with respect to their latitudes [*SpaceWeatherLive.com*, 2022]. The K-index is a 3h index with a quasi-logarithmic scale. For every 3h interval, a digit ranging from 0 to 9 is assigned to both the horizontal (H) and declination (D) component of the geomagnetic field at the station, according to the range of the magnetic fluctuations during this interval and after the regular diurnal variations have been removed. The larger digit during the interval is reported as the stations K-index. 0 corresponds to low geomagnetic and 9 is high geomagnetic activity [*Bartels et al.*, 1939]. The Kp-index is derived from the K-index through a algorithm that takes input from the reported K-indexes from every station. The global Kp-index also ranges from 0 (low) to 9 (high).

The Ap index is a daily average of the global level of geomagnetic activity. Since the K-index' is a non-linear scale, each 3 hour K-index will be transformed back to a linear scale,

called the ap-index. The ap index is a 3h index, and the average from the 8 ap-indexes that are retrieved each day then gives us the Ap-index. High Ap-index corresponds to high geomagnetic activity.

2.3.2 AE index

The Auroral Electrojet (AE) index is an index that quantifies the global auroral electrojet activity in the auroral zone. It is derived from measurements of disturbances in the horizontal component of the geomagnetic field from 12 different observatories, located in the auroral zone of the Northern Hemisphere. The index is normalised through a baseline, which is derived from the averages of the five most quietest days at the station. This baseline is then subtracted from each 1 minute value from that station during that month. Then from all the data from all the stations in a given time (UT) the largest and smallest value is selected [*Kyoto University*, 2022]

The goal of the auroral indices is to get a measure on the instantaneous maximum strength of the westward and eastward electrojets. Since the current changes quickly, a shorter time resolution (1 min) is given - compared to the 3h time resolution for the Kp. The largest value selected in each time from the measurements is the AU-index. It represents the maximum strength of the eastward electrojet. The lowest value selected is the AL-index. It represents the maximum strength of the westward electrojet. The AE index then represents the separation of the two and the overall activity level. It is defined as $AE = AU - AL$, with units [nT] [*Kyoto University*, 2022].

2.3.3 DST index

The Disturbance Storm-Time (DST) index is an index that measures the strength of the ring current. It is derived form measurements of the horizontal component of Earth's magnetic field from four low latitude observatories. The observatories selected are poleward of the magnetic equator (at least 20°) and far equatorward of the auroral zone, to reduce the influence of the equatorial electrojet and the auroral electrojets.

For each observatory a value, $D_i(t)$ is found, which is the derivation from the H-component from a quiet day baseline, compensated for diurnal and annual variations. The units of $D_i(t)$ is nanoteslas [nT]. Taking the magnetic dipole latitude of the observatory the DST is then:

$$DST = \left\langle \frac{D_i(t)}{cos(\phi)} \right\rangle_{i=1,4} \tag{4}$$

ϕ is the magnetic dipole latitude of the given observatory.

2.3.4 Substorms

A substorm is a short-lived disturbance of the magnetosphere where energy is released from the magnetotail into the high latitude ionosphere. It is controlled by the IMF, where

it stops when it is northward and appears when it turns south again [*McPherron*, 1979]. For the simplest case of a substorm, it is described to have 3 phases; a growth phase where energy from the solar wind is stored in the magnetotail, an expansion phase where the energy is released from the tail, and a recovery phase where the magnetosphere relaxes back to its initial state [*McPherron*, 1979].

Substorms are often considered distinct from geomagnetic storms in that they only last for a couple of hours, instead of days, and are observed primarily over the polar region, instead globally. However, a geomagnetic storm can consist of many substorms. Visually, substorms are observed as sudden brightening and increased movements of the auroral arcs. Substorms were first qualitative described by Kristian Birkeland [*Birkeland*, 1908].

2.4 Earth's atmosphere

The atmosphere of the Earth is the layers of gas trapped by Earth's gravity. It's properties changes with both altitude and season, and the atmosphere is divided into two parts, a neutral one and weakly ionised one.

2.4.1 The structure of the atmosphere

Figure 2.17 shows an illustration of the neutral atmosphere, its layers defined by their temperature profiles. The temperatures profiles of the layers vary with latitude and seasons.

The lowest layer is called the troposphere, from the Greek word *tropo* meaning change. It starts at the surface, and as seen in Figure 2.17 it's temperature profile decreases with altitude reaching a minimum, the tropopause. The tropopause's altitude varies with latitude, where its highest at equator (18-20km) and lowest at the poles (around 6 km)[*NOAA*, 2022]. Above the tropopause the temperature profile increases with altitude until it peaks at about 50km, known as the stratospause. This region is called the Stratosphere, from the Latin word *strato* meaning layered. The temperature increase is mainly due to absorption of UV from solar radiation by the ozone (O_3) found in this layer [*Kelley*, 2009]. After the stratospause, radiative cooling by CO_2, H_2O and OH causes a sharp decrease in the temperature profile until a minimum at around 85 km, known as the mesopause [*Kelley*, 2009]. This region is called the mesosphere, from the the Greek word *meso* meaning middle. Above the mesopause, the temperature profile again turns and increases dramatically. The increase is due to absorption of UV, EUV and X-ray radiation from the Sun. The temperature is often above 1000K [*Kelley*, 2009]. The absorption, however, is quite variable. This region is called the thermosphere, from the Greek word *thermo* meaning heat. The varied absorption also impacts its altitude peak, the thermopasue, which varies between 500-1000km altitude. Above the thermospause we have the exosphere, from the greek word exo meaning outside. In this layer atoms and molecules escape into space.

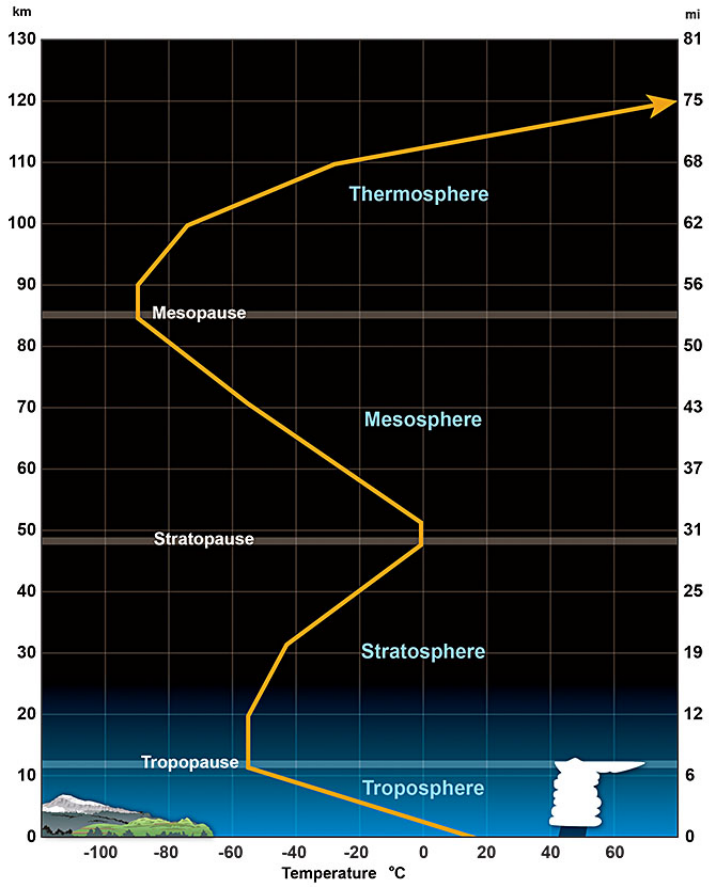

Figure 2.17: Illustration of the Atmospheric layers and their temperature profile, adapted from `https://www.weather.gov/jetstream/layers`

The atmosphere can also be layered by the composition of its constituents. Under around 100km altitude the atmospheric composition - due to variety of turbulent mixing phenomena - is relatively uniform. This region is called the homosphere. Chemically its made of about 78% Nitrogen, 21% oxygen, as well as small percentages of other molecules. The turbopause is located at ∼100km where the constituents of the atmosphere start to separate according to their various masses. Meaning heavier constituents, like nitrogen and oxygen, are found at lower altitudes. Lighter ions, like hydrogen and helium, are found more often at higher altitudes, where they can sometimes can escape Earth's gravitation (see plasmasphere, section 2.2.3). This region is called the heterosphere.

In this thesis we are concerned mostly with the lower thermosphere, corresponding to where auroral electrons deposit their energy. At the top of the mesosphere and lower thermosphere, the atmosphere can be directly affected by particle precipitation. Energetic particles ionise the various gasses here, creating the weakly ionised layer called the ionosphere. The ionosphere spans from 80-1000km, varying with solar activity, MLT etc. [*Kelley*, 2009] (See section 2.4.3).

2.4.2 Solar forcing:

Total solar irradiance (TSI) is the electromagnetic energy in the form of photons that hit the top of Earth's atmosphere. It can be found from integrating the entire solar spectrum and is about 1369 $W \cdot m^{-2}$ [*Bohren and Clothiaux*, 2008]. TSI is the best known and main source of solar forcing into Earth's atmosphere [*Seppälä et al.*, 2014]. TSI also provides the energy required for Earth's climate system [*Bohren and Clothiaux*, 2008; *Seppälä et al.*, 2014]. It influences the atmosphere through a bottom-up mechanism, Where solar irradiation is absorbed over the water on Earth, increasing evaporation. The following increase in moisture will converge in the precipitation zones, which leads to changes in precipitation patterns [*Seppälä et al.*, 2014]. Total solar irradiance is related to the Sun's activity, however, it changes quite slowly and relatively little, with research finding a peak-to-peak variation of around 0.1% during one solar cycle [*Willson and Hudson*, 1991]. Recent research estimates it has only increased about 0.05-0.1% since the 1600s [*Wang et al.*, 2005; *Krivova, N. A. et al.*, 2007; *Steinhilber et al.*, 2009]. Which is why it was known as the solar constant before, an unfortunate name given the recent interest in studying its variability [*Bohren and Clothiaux*, 2008].

investigating different part of the solar spectra, however, a much stronger variability with solar activity can be found. Solar specral Irradiance (SSI) is the solar irradiance measured at the top of the atmosphere per given wavelength and its units are $W \cdot m^{-2} \cdot nm^{-1}$. SSI forcing plays an important role in atmospheric dynamics through its interaction with atmospheric ozone, heating of the middle atmosphere and as a main driver of the top-down mechanism [*Seppälä et al.*, 2014]. The top-down mechanism refers to the connection between the stratosphere and the underlying troposphere and surface climate [*Gray et al.*, 2010]. It starts in the stratosphere, where solar UV radiation heats up the tropical stratosphere and affects the production rates of ozone in the upper atmosphere. Ozone is an important part to radiative heating, so it creates an additional feedback mechanism to the radiative heating [*Seppälä et al.*, 2014]. The dynamical responses to this heating extends the solar influences poleward and downward to the troposphere and surface [*Gray et al.*, 2010].

The solar forcing of most interest for this thesis is Energetic particle precipitation (EPP). The precipitating particles can be both protons and electrons. As discussed in section 2.2.4, and as can be seen in Figure 2.16, auroral electrons originates from the plasma sheet and precipitate almost continuously down in the atmosphere [*Rozanov et al.*, 2012]. They are typically accelerated to energies of around 1-30 keV in the plasma sheet and precipitate at the poles in the auroral oval. They deposit their energies at altitudes around 85 to 130km, meaning the upper mesosphere and lower thermosphere (see Figure 2.18). The strength of the auroral electron precipitation - defined as the total hemispheric energy flux - is related to geomagnetic activity, and reaches a maximum during the declining phase of the solar cycle [*Rozanov et al.*, 2012]. Medium energy electrons (typically 30 keV - 1 Mev) precipitate from the radiations belts into the sub-auroral latitudes [*Rozanov et al.*, 2012] and deposits their energies at altitudes between 55 and 85 km [*Turunen et al.*, 2009]. The energetic particles can also come from the Sun in large solar particle events (SPE)

[*Sinnhuber et al.*, 2012]. The particles are guided into Earth's atmosphere through Earth's magnetic fields.

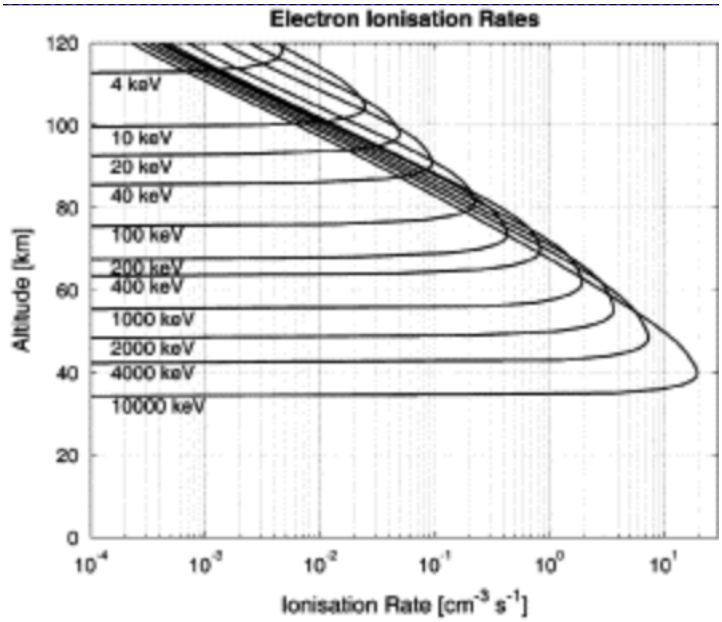

Figure 2.18: Electron ionisation rates for different energy bands plotted against altitude, from [Turunen et al., 2009]

The ionisation caused by the precipitating electrons leads to increased production of HO_x (H, OH, HO_2) and NO_x (N, NO, NO_2). These gasses play an important role in middle atmospheric dynamics through the destruction of ozone in the stratosphere [*Brasseur and Solomon*, 2005; *Seppälä et al.*, 2014; *Turunen et al.*, 2009]. The precipitation of the low energy electrons have been shown to enhance the production of NO_x-gasses in the lower thermosphere [*Turunen et al.*, 2009; *Sætre et al.*, 2004]. There is a strong increase of NO concentration from low latitudes, where NO is mainly formed by solar x-ray, to the higher latitudes [*Sinnhuber et al.*, 2012], where they are produced by the low energy auroral electrons [*Sinnhuber et al.*, 2012; *Seppälä et al.*, 2014; *Turunen et al.*, 2009]. Several studies have shown and established the relationship between production and concentration of NO_x in the polar regions and various indicators of Auroral precipitation [*Turunen et al.*, 2009; *Sinnhuber et al.*, 2012]. There is also, on average, a visible broad auroral oval-like structure of NO in the lower thermosphere, despite the variability of the thermospheric NO [*Sinnhuber et al.*, 2012; *Sætre et al.*, 2006], see Figure 2.19

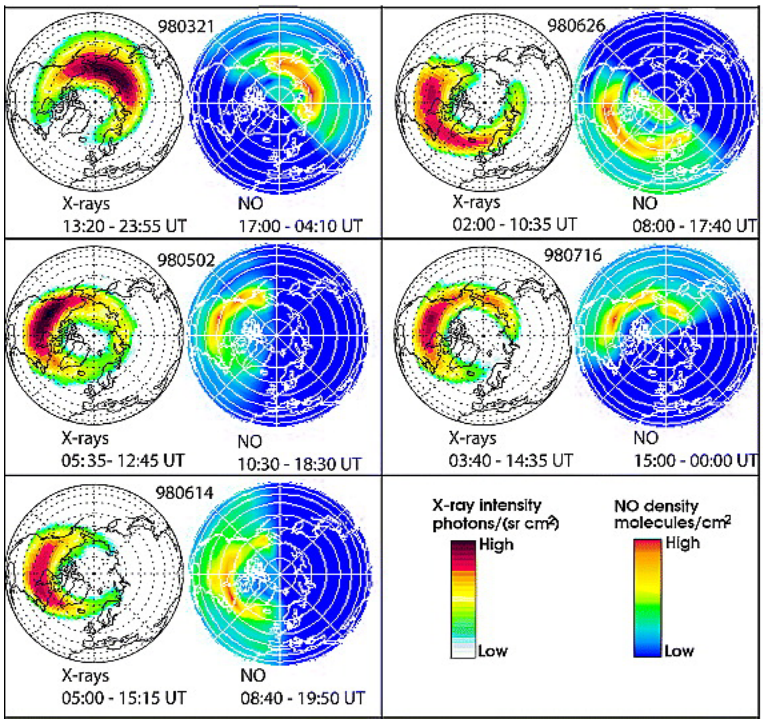

Figure 2.19: Time-integrated X-ray bremsstrahlung (∼2–9 keV) from PIXIE measurements (white globe) in photons/(sr cm^2), and nitric oxide density at 110 km altitude measured by SNOE/UVS (blue globe) in molecules/cm^2. Geographic coordinates, time ranges given under each plot. From [Sætre et al., 2006]

The lifetime of NO_x is dependent on altitude and they can have a lifetime of one to several days in the lower thermosphere during sunlit conditions [*Sinnhuber et al.*, 2012]. Under the polar winter however - due to the absence of sunlight - the lifetime of NO_x is longer [*Baumgaertner et al.*, 2009], up to months. In the polar winter the Brewer-Dobson circulation is downward, meaning the NO_x enhancement will travel downwards - inside the polar vortex - to the stratosphere [*Baumgaertner et al.*, 2009]. Hence, NO_x enhancement has and can be observed at stratospheric altitudes, far lower than their production altitude. In the stratosphere the NO_x enhancements will efficiently destroy Ozone through catalytic reactions. This is considered to be the indirect effect of EPP, opposed to the direct effect of enhanced NO_x and HO_x in the mesosphere and lower thermosphere [*Baumgaertner et al.*, 2009]. The change of ozone concentration in the stratosphere leads to perturbation of the radiative balance, which can impact the dynamics of the polar vortex which connects to the surface climate [*Rozanov et al.*, 2012].

2.4.3 The Ionosphere

The famous and high regarded German physicist Carl Friedrich Gauss postulated as early as 1839, an electrically conductive region of the atmosphere could explain the observed variations of Earth's magnetic field. By the early 1900s several scientist believed that the upper part of the atmosphere was partly ionised. Birkeland theorised that there were

electrical currents in the upper part of the atmosphere [*Birkeland*, 1908]. In 1901 Guglielmo Marconi, an Italian engineer, became the first person to send and receive a trans-Atlantic radio signal. Similar experiments would further indicate the existence of a ionised layer, and in 1924 and 1925 Appelton and Barnett proved the existence of a reflective layer in the upper atmosphere [*Ratcliffe*, 1975]. This layer in the atmosphere would later be called *the ionosphere*.

The ionosphere is a partially and weakly ionised gas that surrounds the Earth at altitudes of 80-1500km, and can be seen as a form of interface/connection between Earth's atmosphere and space [*Kelley*, 2009]. It is the first layer of the atmosphere where its possible to have plasma. The solar UV hitting the Earth's atmosphere ionises part of the neutral atmosphere. It is highly altitude dependent determined not only by the solar irradiation, but also the constituents of the atmosphere and its density [*Baumjohann and Treumann*, 1996]. Above altitudes of 80km, collisions between neutral molecules and the solar ionised ions are too infrequent to result in rapid recombination, and a more permanent ionised gas is formed - the Ionosphere [*Baumjohann and Treumann*, 1996].

The ionosphere is divided into 4 regions (see Fig 2.20) based on different characteristics and parameters related to altitude. The four regions are D, E, F1 and F2 [*Kelley*, 2009]. The **D-region** is created by solar irradiation and only exists on the dayside. Here recombination is very rapid due to the negative ion effect, and the layer only lives a couple of minutes after sunset [*Kelley*, 2009]. It is in the altitude range 70-90 km and its major constituents are NO+ and O_2+ [*Kelley*, 2009]. The **E-region** differs from the D-region

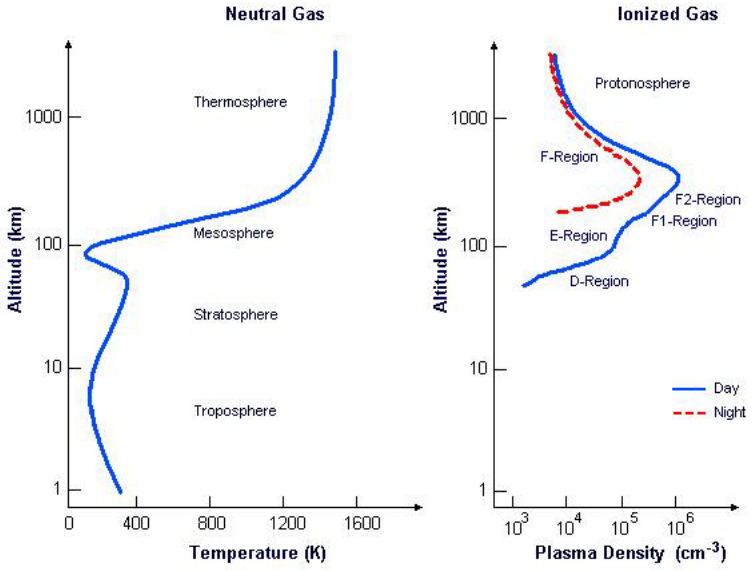

Figure 2.20: Typical profiles of neutral atmospheric temperature and ionospheric plasma density with the various layers named, adapted from [Kelley, 2009]

.

on density, effecting the type of photonionisation. The E-region recombines rapidly, but

significantly slower than the F-region, and often disappears after midnight [*Kelley*, 2009]. It is in the altitude range 90-140 km and has the same major constituents as the D-region [*Kelley*, 2009]. The **F-region** also differs from the E-region based on density. It is divided into to two, where F1 mostly recombines after sundown, however pockets of ionisation can remain, while F2 is persistent after sundown [*Kelley*, 2009]. F1 is in the altitude range 140-200 km while F2 is $\geq$ 200 km. The major constituents are O+ and NO+ for F1 and O+ for F2.

2.5 Recent research

Besides the general established theories in space physics, the current thesis is motivated by research that addresses challenges in respect to quantification of the precipitating auroral electron fluxes. The most relevant studies published the recent years are listed below.

[*Hendrickx et al.*, 2018] studies the production and transport mechanisms in the polar upper mesosphere and lower thermosphere applying both satellite observations and a chemistry-climate model. They made a detailed NO comparison in the antarctic between observations by the Solar Occultation for Ice Experiment (SOFIE) instrument on-board the Aeronomy of Ice in the Mesosphere (AIM) satellite and simulations performed by the Whole Atmosphere Community Climate Model with Specified Dynamics (WACCM-SD). They found the long term mean in WACCM to be too high, while the short-term variability is too low compared to the satellite observations. Furthermore, they discovered the peak NO density altitude was considerably higher in WACCM compared to SOFIE-AIM, particularly during winter.

[*Smith-Johnsen et al.*, 2017] targets the direct and indirect effect of energetic particle precipitation on NO production during an geomagnetic storm in April 2010 in the middle polar atmosphere. Using the Total Energy Detector (TED) and and Medium Energy Proton Electron Detector (MEPED) on board polar orbiting satellites, they obtained a full electron energy spectrum from 1-750 keV. This corresponds to energy deposition altitudes between 60-120 km. They find evidence of direct NO production down to 55 km. The energy deposition maximises between 100-120 km (the lower thermosphere).

[*Smith-Johnsen et al.*, 2018] examines the NO response of WACCM from the same April 2010 geomagnetic storm, compared to satellite observations. They find that WACCM overestimates the energy deposition in the lower thermosphere for low geomagnetic activity and underestimates for high geomagnetic activity compared to the energy deposition derived from the flux measurements from TED and MEPED. Consistently, they find the NO production in the lower thermosphere is overestimated during for low geomagnetic activity and overestimated for high activity compared to NO density satellite observations.

[*Smith-Johnsen et al.*, 2022] performs a sensitivity study on the mesospheric transport of NO in WACCM compared to satellite observations. Again, it is demonstrated that WACCM overestimates the NO production in the lower thermosphere during periods of low geomagnetic activity.

[*Tesema et al.*, 2020] studies electron precipitation during pulsating aurora and its chemical impact. They use the SSJ electron detector from DMSP satellites and TED from POES

satellites. They found relative coherence between the DMSP/SSJ and TED measurements at higher energies. NO_x enhancement, modelled form the precipitating electrons, were also found to peak around 100 km altitude.

[*Partamies et al.*, 2021] examines the characteristics of precipitating electrons during isolated, compound and multi-night substorm events, using measurements from DMSP/SSJ and POES/TED and MEPED. They find that during the expansionary phases of the substorms, DMSP/SSJ detects enhanced flux levels at energies of few keV. They further find the flux levels for energies up to 10 keV to be half an order of magnitude lower for the recovery phase compared to the expansion phase.

3 Data and Methods

3.1 Statistics

This study compares different auroral forcing estimates through the use of statistical methods. This section will be devoted to explaining these methods.

Averages and Errors:

There are several ways to define an "average" [*Bohren and Clothiaux*, 2008]. The arithmetic mean is most commonly referred to as an average, but you also have the median, the most probable value etc.. All of these can be considered an "average", but they represent different features. An average is often used to report central tendencies in data. For the arithmetic mean this can be problematic. Outliers can greatly influence it, and for skewed distributions it will not represent the typical value of the data set. Here the median gives a much better description of the central tendencies of the data, considering it is defined as the middle value. This implies, that when defining an average, one should always ask what the calculated value will represent. For much of observational and experimental data, the interest is often in finding an estimate for the mathematically typical value of the data set. For the arithmetic mean, every value in the data set affects the value of the mean, meaning there is no loss of information. This is unlike the median or most probable value, where outliers are ignored. The arithmetic mean also has the quality of further algebraic treatment. In this study the goal is to compare estimates of auroral forcing from different sources. No loss of information is therefore important, with "outliers" included in our averages. Due to this, the arithmetic mean is chosen to represent the averages in this study.

When computing averages there is always uncertainty and error involved. Standard practice is to report these deviations in form of ranges, error bars etc. The standard deviation (SD) is frequently applied and represents the spread of a data set. Quantiles can also show the spread of a data set. To show the uncertainty of the computed estimate of the mean, the standard error of the mean (SEM) is commonly used. The SEM shows the accuracy of the mean computation. Another way to display the accuracy of the estimated mean, is using 95% confidence intervals (CI). The 95% confidence means that if we were to repeat the experiment on random samples a 100 times and compute a 95% confidence interval for each sample, then 95 of the 100 confidence intervals will contain the true mean value of the population. For large N and approximately normal distributed data, the 95% confidence interval can be approximated to be:

$$CI_{95\%} = \bar{x} \pm 1.96 \cdot SEM \tag{5}$$

However, it is not always possible to assert any assumptions about the distribution of the underlying data/population. Here, one can use the Bootstrap method, first described by *Efron* [1979]. It is a simple but powerful technique, especially in the age of modern computers. The bootstrap method resamples, with replacements, your data set N number

of times, and then computes the effect size of interest on each of these resamples. For a 95% confidence interval, it calculates the mean for each of these samples and due to the Central Limit Theorem [*Kwak and Kim*, 2017], the distribution of the means will reach normality with increasing N, even if the underlying population is not normally distributed. With modern computers, one can easily run thousands to millions of resamples. This means one can calculate the 95% confidence intervals without making any assumptions about the underlying distribution of the data. In this thesis, the calculated averages are limited in the fact that they can't be below zero. With that in mind, and the lack of need to assume a distribution for the various data, bootstrap 95% CI is chosen to represent the uncertainties of the calculated averages.

3.1.1 Distributions

In this study electron flux energy spectra will be studied and their distributions will be looked at in reference to known distributions of precipitating electrons. This subsection will give a brief description of the three distributions the electron flux energy spectra are fitted with in this thesis; Maxwellian, power law and exponential. A short description of the values used to evaluate the goodness of fit of the three distributions will be given as well.

Maxwellian:

If electrons are in thermodynamic equilibrium of each other the distribution function is Maxwellian. The Maxwellian distribution is of the form [*McIntosh and Anderson*, 2014]

$$\frac{dN}{dE} = \frac{Q_0}{2E_0^3} E exp(\frac{-E}{E_0}) \tag{6}$$

dN/dE is the differential number flux, Q_0 is the energy flux $[eVcm^{-2}ster^{-1}s^{-1}]$ and E_0 is the characteristic energy (eV). The average energy of the Maxwellian distribution is equal to twice that of the characteristic energy, $\overline{E} = 2E_0$. The total number of flux of the Maxwellian distribution can be obtained through

$$N_0 = \frac{Q_0}{2E_0} \tag{7}$$

It is widely accepted that the spectra of electrons that can be characterised by a Maxwellian distribution are associated with diffuse aurora, whose particle source maps to the inner plasma sheet [*McIntosh and Anderson*, 2014]

Power law:

A Power Law is a function f(x) where the value y is proportional to some power of the input x:

$$F(x) = y = x^{-\alpha} \tag{8}$$

The power law distribution is a continuous positive-only distribution that describes a quantity whose probability decreases as a power of its magnitude. The AIMOS model, used in this study, assumes a power law distribution for the spectra of the electron flux it builds upon [*Wissing and Kallenrode*, 2009].

Exponential:

The Exponential distribution is a continuous positive-only distribution that describes the distribution of times between successive independent events in a Poisson process with an average rate of «λ» events per unit time. A Poisson process is a model for when a series of discrete events, where the exact timing of them is random, but the mean time between the events is known. The exponential distribution is given by the form:

$$f(x) = \lambda e^{-\lambda x} \tag{9}$$

Sum squared estimate of errors (SSE)

Sum squared estimate of errors or summed square of residuals is a statistics measure of the total deviation of the values from the fit to the observed values. It is often labelled SSE and is given by:

$$SSE = \sum_{i=1}^{n} (y_i - \hat{y}_i)^2 \tag{10}$$

where y are the values of the observed value to be predicted and $\hat{y}$ are the predicted value of the distribution/model. A value closer to 0 is a sign of "good fit", indicating the model has a small error and will be useful for prediction. However, like all goodness of fit values, the location where it goes from bad to decent to good is somewhat subjective and arbitrary. Still comparing two fits, the one with lowest SSE will be more useful for prediction and can be considered a "better fit".

R-square and Adjusted R-square

R-square is an statistical measure that measures how successful a model can explain the variation of the observed values. The R-square is the square of correlation between the observed values and the ones predicted by the model. It is defined by the ratio of two other statistical measurements, sum of squares of the regression (SSR) and the total sum of squares (SST). SSR is given by:

$$SSR = \sum_{i=1}^{n} (\hat{y}_i - \bar{y})^2 \tag{11}$$

$\hat{y}$ are again the values predicted by the model and $\bar{y}$ is the mean value of the observed values. SST is defined as SST=SSR+SSE, meaning R-square can be given as:

$$R - square = \frac{SSR}{SST} = \frac{SSR}{SSR + SSE} = 1 - \frac{SSE}{SST} \tag{12}$$

The R-square can take any value between 0 and 1, where closer to 1 indicates better explanation of the variation of the data. Like the SSE, what can be considered a "bad", "decent" or "good" fit is subjective.

The R-square has the issue where adding coefficients to a model will either increase it or have no change at all. This will happened even if the added coefficient doesn't in any practical form improve the fit. Here the adjusted R-square is introduced. The degree of freedom adjusted R-square adds a penalty for each added coefficient to the model. The residual degrees of freedom is defined as v=n-m, where n is the observed values to be fitted and m is number of coefficient. The adjusted R-square is then given by:

$$adjustedR - square = 1 - \frac{SSE(n-1)}{SST(v)} \tag{13}$$

Again, like with R-square, Adjusted R-square can fall between 0 and 1, where 1 indicates good explanation of the variation of the data and 0 indicates poor explanation.

3.2 NOAA POES and TED

The National Oceanic and Atmospheric Administration (NOAA) operates the Polar Operational Environment Satellites (POES), which carries instruments for measuring the influx of energetic electrons and ions precipitating into the Earth's atmosphere, as well as other climate related data. The SEM-2 package on board these satellites carry the Total Energy Detector (TED) used in this thesis.

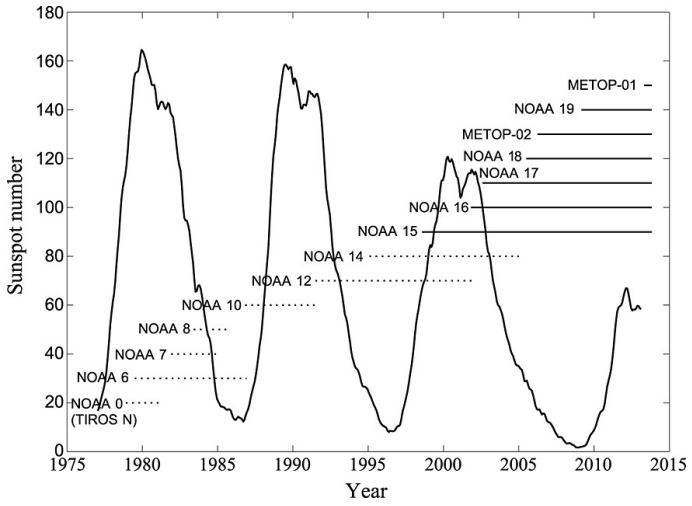

Figure 3.1: Lifetime of NOAA POES and MetOp satelittes carrying SEM1/SEM2, from [Sandanger et al., 2015]

The first satellite mounted with TED, as part of the SEM-1 package, was first launched in 1978. It has since been launched with 14 different satellites, 12 from the NOAA POES program and 2 from the MetOp program. Figure 3.1 shows the operational time periods of satellites carrying the TED instrument. SEM-2 was introduced with NOAA-15 in 1998 [*Evans and Greer*, 2004]. In the year 2010, the time period of interest for this thesis, six satellites were operational: NOAA15 - 19 and MetOp-02, all carrying the SEM-2 instrument package. The NOAA POES and MetOp satellites are low Earth orbit (LEO) Sun-synchronous polar orbiting spacecrafts [*Sandanger et al.*, 2015]. They complete around 14 orbits per day at altitudes ∼850 km. Figure 3.2 shows an MLT-CGMlat map of the coverage of the six satellites for the year of 2010.

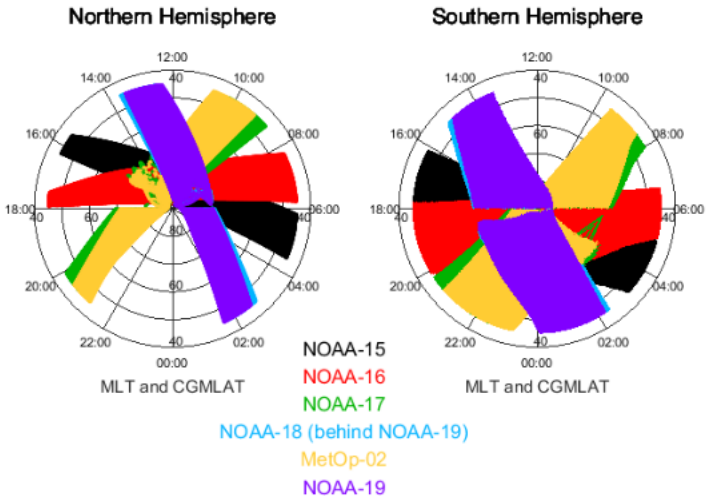

Figure 3.2: MLT-CGMlat coverage of NOAA15-19 and MetOp-02 for the year 2010, both NH and SH

The Total Energy Detector (TED) is an instrument for measuring the energy flux carried by auroral particles into the polar atmosphere. The auroral particles are positively charged ions (assumed to be protons) and electrons. [*Evans and Greer*, 2004].

The TED consists of two detector systems, one at 0° and one at 30° to the local vertical [*Søraas et al.*, 2018; *Smith-Johnsen et al.*, 2017]. The 0° detector is placed on the three axis stabilised spacecraft so that the centre of each detector field of view is outward along the local zenith, parallel to the Earth-centre-satellite radial vector (-X direction in spacecraft coordinates) [*Evans and Greer*, 2004]. The 30° detector is placed such that the field of view is centred at 30° to the Earth-centre-satellite radial vector (-Z direction in spacecraft coordinates) [*Evans and Greer*, 2004].

For each system there are four particle detectors. Of the four, two are devoted for measuring electrons in the energy range 0.05-20 keV, where one measures for energies between 0.05-1 keV and the other for energies between 1-20 keV [*Evans and Greer*, 2004]. The remaining two detectors are for protons, with one with an energy range between 0.05-1 keV and the other between 1-20 keV. In this thesis we use 4 differential electron energy bands shown in Table 1

Channel 1	Channel 2	Channel 3	Channel 4
0.154-0.224 keV	0.688-1.000 keV	2.115-3.075 keV	6.503-9.457 keV

Table 1: Table of the TED energy bands used in this study, named Channel 1, Channel 2, Channel 3, Channel 4

Table 2 shows how the data from the TED was binned. Each data point has a MLT value, a CGMLAT value and a flux value respectively. Column one shows the electron energy flux values, Column two the CGMLAT value and column three the MLT value. The data is then binned into MLT and CGMLAT sectors. Mostly in this study, the MLT sectors are defined as $0 \leq MLT < 3$ and etc to 24. For CGMLAT they are defined as $40 \leq CGMLAT < 41$ and etc to 89. The data also includes its geographic coordinates, binned in the same way as MLT and CGMLAT. The binning is the same for both the detectors.

Flux	CGMLAT	MLT
...	...	...
...	...	...
...	...	...
...	...	...

MLT	40 CGMLat	41 CGMLat	...
MLT0-3	FLux1	FLux2	...
MLT3-6	...	...	...
...	...	...	...

Table 2: Table showing how the TED data used in this study is binned

3.3 DMSP

The Defense Meteorological Satellite Program (DMSP) spacecrafts are a series of LEO satellites, whose mission is to observe the space environment using the precipitating energetic particle spectrometer SSJ/4 / SSJ/5 [*Redmon et al.*, 2017a]. The DMSP satellites travels through the ionosphere in Sun-synchronous orbit at around 840 km altitude [*Redmon et al.*, 2017a]. They complete around 14 orbits a day, with an orbit time of roughly 101 minutes.

The first DMSP satellite carrying SSJ/4 was F6, launched in 1982, with the last one being F15, launched in 1999. The first mounted with SSJ/5 was F16 which launched in 2003. In the year 2010 the DMSP satellites F15-18 were operational, as seen in Figure 3.3. This

means both satellites with SSJ/4 and SSJ/5 were operational in 2010. Figure 3.3 also shows the satellites orbits/trajectories in CGMLT-MLAT map for 2010 in the northern hemisphere

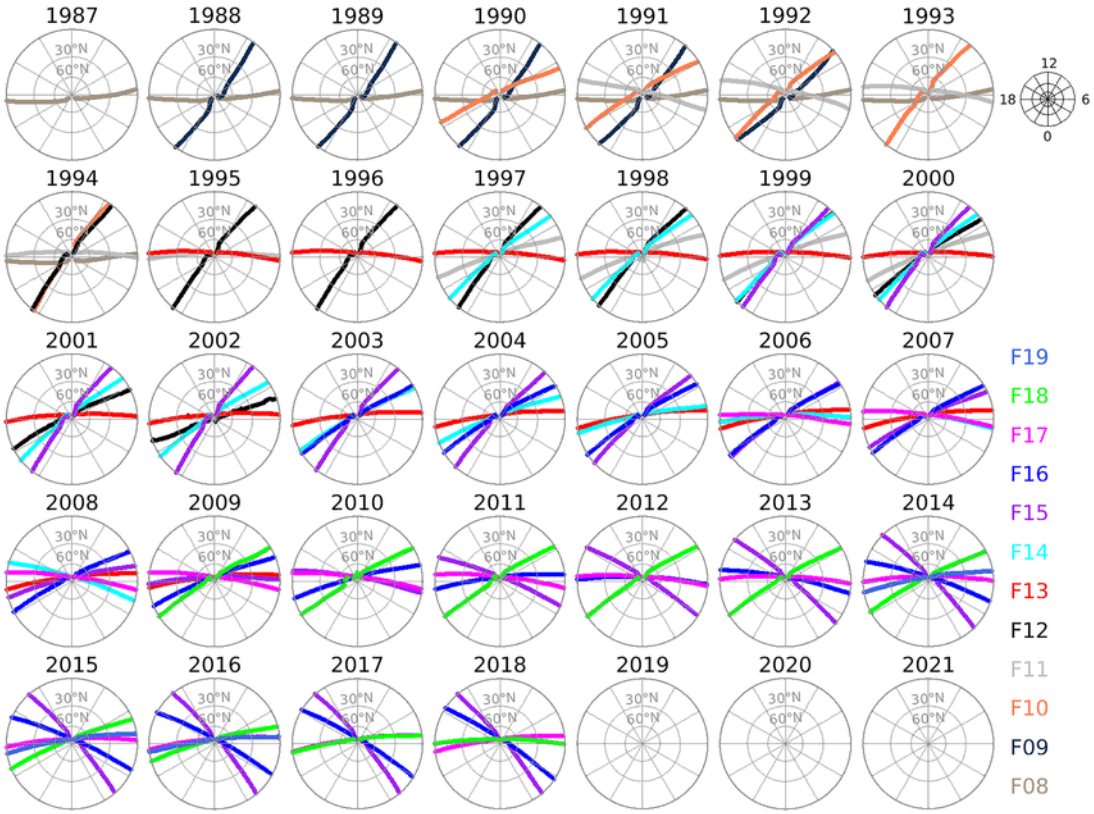

Figure 3.3: DMSP satellite Trajectories in the Northern hemisphere for CGMLT-MLAT by year, [Cai et al., 2019]

The SSJ/4 detector is an electrostatic analyser for electrons and protons. It measures the flux of precipitating electrons in the energy range 0.03-30 keV [*Redmon et al.*, 2017a]. It is made up of four detectors, one high energy and low energy detector for each particle. The low energy detector covers the range 0.03-1 keV, while the high energy one covers 1-30 keV. The detectors have 10 logarithmically spaced energy steps. The SSJ/5 was designed as a single triquadraspheric electrostatic analyser [*Redmon et al.*, 2017a]. It has a spherical geometry that provides 6 non-overlapping in-plane look directions, mounted such that the 90° total field of view covers the ram direction to zenith [*Redmon et al.*, 2017a]. Figure 3.4 shows an illustration of the SSJ/5 and it's field of view.

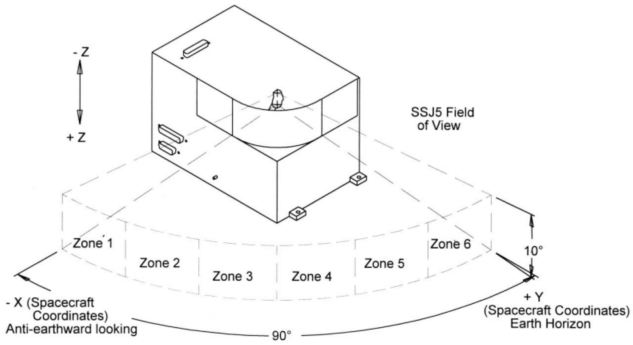

Figure 3.4: Illustration of the the SSJ/5 detectors field of view mounted on a DMSP satellite, from [College, 2022]

The energy range and channels for the SSJ/5 were made to specifically match the ones on for SSJ/4 [*Redmon et al.*, 2017a]. Figure 3.5 shows the central energies and channel spacings for the SSJ Detector. In this study, channels 4-15 (E_i=0.2-9.450 keV) are used and the data for the DMSP is binned similarly as for the TED, eg. Table 2.

Channel	**1**	**2**	**3**	**4**	**5**	**6**	**7**	**8**	**9**	**10**
E_i (eV)	30000	20400	13900	9450	6460	4400	3000	2040	1392	949
ΔE_i (eV)	9600	8050	5475	3720	2525	1730	1180	804	545.5	373
Channel	**11**	**12**	**13**	**14**	**15**	**16**	**17**	**18**	**19**	**20**
E_i (eV)	949	646	440	300	204	139	95	65	44	30
ΔE_i (eV)	373	254.5	173	118	80.5	54.5	37	25.5	17.5	14

Figure 3.5: SSJ sensor values for the channel central energy (E_i) and channel spacing (ΔE_i), from `https://apps.dtic.mil/sti/pdfs/ADA613822.pdf`

3.4 AIMOS

Atmospheric Ionization Module Osnabrück (AIMOS) is 3-D numerical model of atmospheric ionisation due to particle precipitation [*Wissing and Kallenrode*, 2009]. It is made of two parts: Monte Carlo simulations to calculate ionisation rates, and a sorting algorithm to assign particle fluxes at the top of the atmosphere from two polar orbiting satellites to horizontal precipitation cells. [*Wissing and Kallenrode*, 2009; *Funke et al.*, 2011]. AIMOS spans from the surface to the thermosphere. It is separated by different pressure levels, which roughly corresponds with different altitude regions, with the original grid having 67 equidistant levels. The energy range of the electrons are 0.154 to 300 keV, which implies direct ionisation in the altitude range from 70 km to 400 km. AIMOS 1.v6 is used in this thesis, and it allows for both geomagnetic and geographic grids, website: `https://aimos.physik.uos.de/`. The original time resolution is 2h, however, the model allows for a coarser ionisation rate output as well, eg. 12h, 24h.

The particle fluxes implemented at the top of the atmosphere is detected by the TED and MEPED instruments on POES 15/16 and the SEM instruments on GOES 10 as well

[*Wissing and Kallenrode*, 2009; *Funke et al.*, 2011]. The measurements are in-situ, so to get a global coverage, AIMOS uses the high energy particle fluxes from the GOES and the mean fluxes from polar crossing POES satellites inside an empirically determined polar cap. While outside this polar cap, particle precipitation depends on the geomagnetic latitude, geomagnetic activity, and local time [*Funke et al.*, 2011]. Therefore, average precipitation maps, based on the 4 year data sets from TED and MEPED, sorted by Kp and geomagnetic latitude, was produced for the model [*Wissing and Kallenrode*, 2009; *Funke et al.*, 2011]. These maps are used to represent the spatial distribution, e.g the movement of the aurora oval [*Funke et al.*, 2011]. Then, according to the recent Kp level, the average precipitation maps are selected and scaled to the observed POES particle fluxes. The spatial resolution is 96 zonal cells divided into 48 meridional sections [*Funke et al.*, 2011]. AIMOS uses the TED 0° detector and the energy bands listed in Table 1.

The Monte Carlo simulations are based on the GEANT4-simulation toolkit [*Wissing and Kallenrode*, 2009]. GEANT4 provides Monte Carlo algorithms to model energy ionisation from protons and electrons [*Funke et al.*, 2011]. To perform the convolution with the Monte Carlo results, a description of the incident particle spectra is needed. AIMOS assumes a power law spectrum [*Wissing and Kallenrode*, 2009].

The AIMOS data used in this thesis are based on daily resolved data. The model is run on both geographical and geomagnetic grid depending on the comparison. We limit the particle species to include only electrons, to avoid potential impact from energetic protons. Table 3 lists the criteria applied when running the AIMOS model for this study.

Time interval	particle specie	lower lat border	upper lat border	lower long border	upper long border	pressure lvl 1	pressure lvl 2
1	e	0	1	0	1	ionisation rate	ionisation rate
...	...	...	...	...	...	...	...

Table 3: Visualisation on how the AIMOS data is binned

3.5 WACCM

Whole Atmosphere Community Climate Model (WACCM) is a global numerical climate-chemistry model developed by the National Center for Atmospheric Research (NCAR). It is built upon the numerical framework of Community Earth System Model (CESM), as an atmospheric component that extends to the lower thermosphere [*Marsh et al.*, 2013]. It includes interactive chemistry and dynamics integrated from Community Atmosphere Model (CAM) physics [*Liu et al.*, 2010].

WACCM is a superset of CAM4, and has the same physics and includes all of the physical parameterisations of that model [*Marsh et al.*, 2013]. However, processes important for reproducing the observed mean meridional circulation in the stratosphere and mesosphere and the distribution of minor constituents are included as well [*Hurrell et al.*, 2013]. This includes the parameterisation of non-orographic gravity waves, molecular diffusion, EPP and non-local thermodynamic equilibrium radiative transfer [*Hurrell et al.*, 2013].

The version of WACCM used in this study is WACCM6, which was released in 2019.

WACCM6 was a major update of the whole atmosphere modelling capability in the CESM, included enhanced physical, chemical and aerosol parameterisations [*Gettelman et al.*, 2019]. It extends from the surface up to about 140 km altitude or $6 \cdot 10^{-6}$ hPa, with 88 differnet pressure levels. WACCM6 has a resolution of 0.9°latitude x 1.25°longitude.

WACCM6 includes ionisation rate forcing from both auroral particles and MEE. The ionisation rates are paramterised from different independent sources, so it is possible to only look at the effects from one or the other. For Aurora electrons WACCM6 uses the paramterised auroral boundary model of *Roble and Ridley* [1994]. The parameterisation of the energy deposited by the aurora electrons uses the Kp-index as input [*Smith-Johnsen et al.*, 2018; *Gettelman et al.*, 2019]. Kp represents the global level of geomagnetic activity and is used in WACCM6 to calculate the Hemispheric Power (HP) from the relationship established in *Zhang and Paxton* [2008], equation (14-15). HP is the estimated power deposited in the polar regions from EPP [*Smith-Johnsen et al.*, 2018]. HP is used to find the energy-flux distribution of the electrons. The energy-flux spectrum can then be used to calculate the ionisation rate as a function of altitude [*Roble et al.*, 1987]. WACCM assumes a Maxwellian distribution with an characteristic energy of 2 keV for the auroral electrons [*Smith-Johnsen et al.*, 2018]

$$HP(GW) = 16.82e^{0.32Kp} - 4.86 \; Kp \leq 7 \tag{14}$$
$$HP(GW) = 153.13 + 73.4(Kp - 7) \; Kp > 7 \tag{15}$$

The data from WACCM6 used in this study was provided by Christine Smith-Johnsen. The latitude-longitude resolution was the standard WACCM6 one (0.9 x 1.25 °). The data was binned into 4-D matrices (longitude x latitude x pressure level x date), with one matrix for the ionisation rate and a another one for the respective altitude. The ionisation rates at certain altitudes could then be picked out and plotted on geographical latitude-longitude maps.

3.6 Methods

For both TED and DMSP, the flux values are averaged over daily each Kp level, for each CGMlat band and each MLT sector for the year 2010. Log_{10} are taken of the Kp averaged flux values. They are then plotted onto various CGMlat-MLT polar maps and flux energy spectra.

For AIMOS, the data is converted to geomagnetic (CGMlat-MLT) when compared to TED/DMSP and geographic (latitude-longitude) when compared to WACCM. The ionisation rates at the pressure levels corresponding to the altitude of interest is then picked out. The ionisation rates are then averaged over each daily Kp level, for each latitude and latitude band or CGMlat band and MLT sector, depending if compared to WACCM or TED/DMSP. The $\log_{10}$ of these Kp averaged ionisation rates are then plotted onto various polar maps.

For comparison with WACCM the resolution for AIMOS is 24h, while for comparison with TED the resolution is 2h (lowest possible time resolution). Since AIMOS only gives out

geomagnetic coordinates in the form of latitude and longitude, the longitude is converted to MLT through a conversion program.

Similarly for AIMOS, the ionisation rates for WACCM at pressure levels corresponding to the altitudes of interest are picked out. The ionisation rates are then averaged over each Kp level, for each latitude and longitude band. The $\log_{10}$ of these ionisation rates is then plotted on various polar maps.

4 Results

4.1 Daily Kp for 2010

In this study the results is sorted by daily Kp levels for the year 2010. The 3h Kp levels were downloaded from `https://www.ngdc.noaa.gov/stp/GEOMAG/kp_ap.html` and converted to daily Kp averages. Figure 4.1 shows the daily rounded Kp levels for the year of 2010. The Kp levels are: Kp = 0 (66 days), Kp = 1 (184 days), Kp = 2 (84 days), Kp = 3 (23 days), Kp = 4 (5 days) and Kp = 5 (3 days). (The low statistic related to Kp-level 4 and 5 implies that resulting data will be interpreted with caution.)

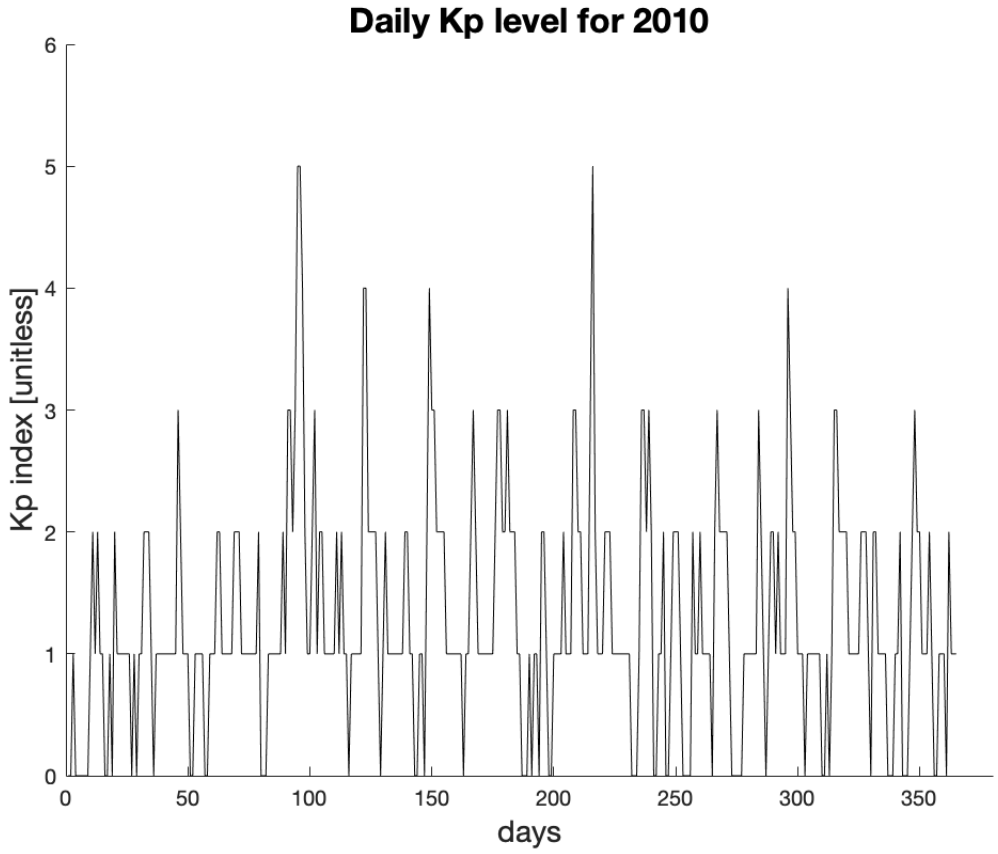

Figure 4.1: Daily Kp levels for the year 2010

4.2 TED vs DMSP

The goal of this section is to compare the electron flux levels observed by the TED detectors on board POES satellites to the SSJ/4 / SSJ/5 detectors on board DMSP satellites. The flux data is sorted according to magnetic local time (MLT), CGM latitudes, and daily Kp values throughout the year 2010. The resulting averages are then displayed as flux maps (MLT vs CGMlat) for the individual energy channels and explored to evaluate the

general behaviour of the EEP, as well as potential systematic differences between the flux level and behaviour detected by DMSP and POES. (The resolution is 3 hour MLT and 1° CGM latitude.) The following sections first focus on what the individual detectors observe for similar energy channels, before comparing the respective flux maps. Furthermore the electron energy flux spectra of the detectors will be plotted, studied and fitted with the distributions mentioned in section 3.1.1

4.2.1 TED

In this subsection the daily Kp average flux data from the two TED detectors for Channel 2 (0.688-1.000 keV), 3 (2.115-3.075 keV) and 4 (6.503-9.457 keV) are evaluated in respect to MLT, CGMLat- and Kp dependence. Differences between energy channels and 0° and 30° detectors are highlighted. Channel 2-4 is chosen due to observing electrons in energy ranges above 1 keV which will deposit their energy in the lower thermosphere.

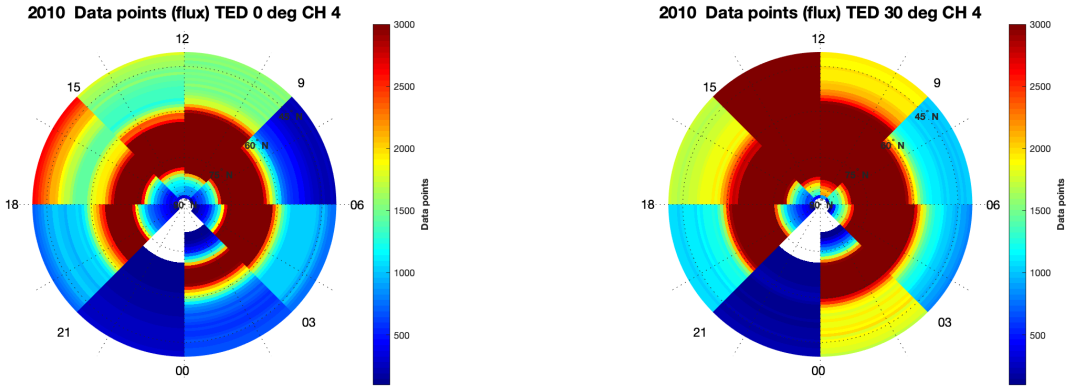

Figure 4.2: Coverage and statistics maps for TED 0° and 30° detectors for CH4 for the entire year of 2010

Figure 4.2 shows the number of data points for every MLT sector of the flux levels observed in Channel 4, for both 0° and 30° detector. The 21-00 MLT sector has poor data coverage, as also demonstrated in Figure 3.2, and will be ignored in the future comparison. Figure 4.2 shows, however, that the 30° has more data points above the respective threshold. This is particular true for the 80° CGM latitude.

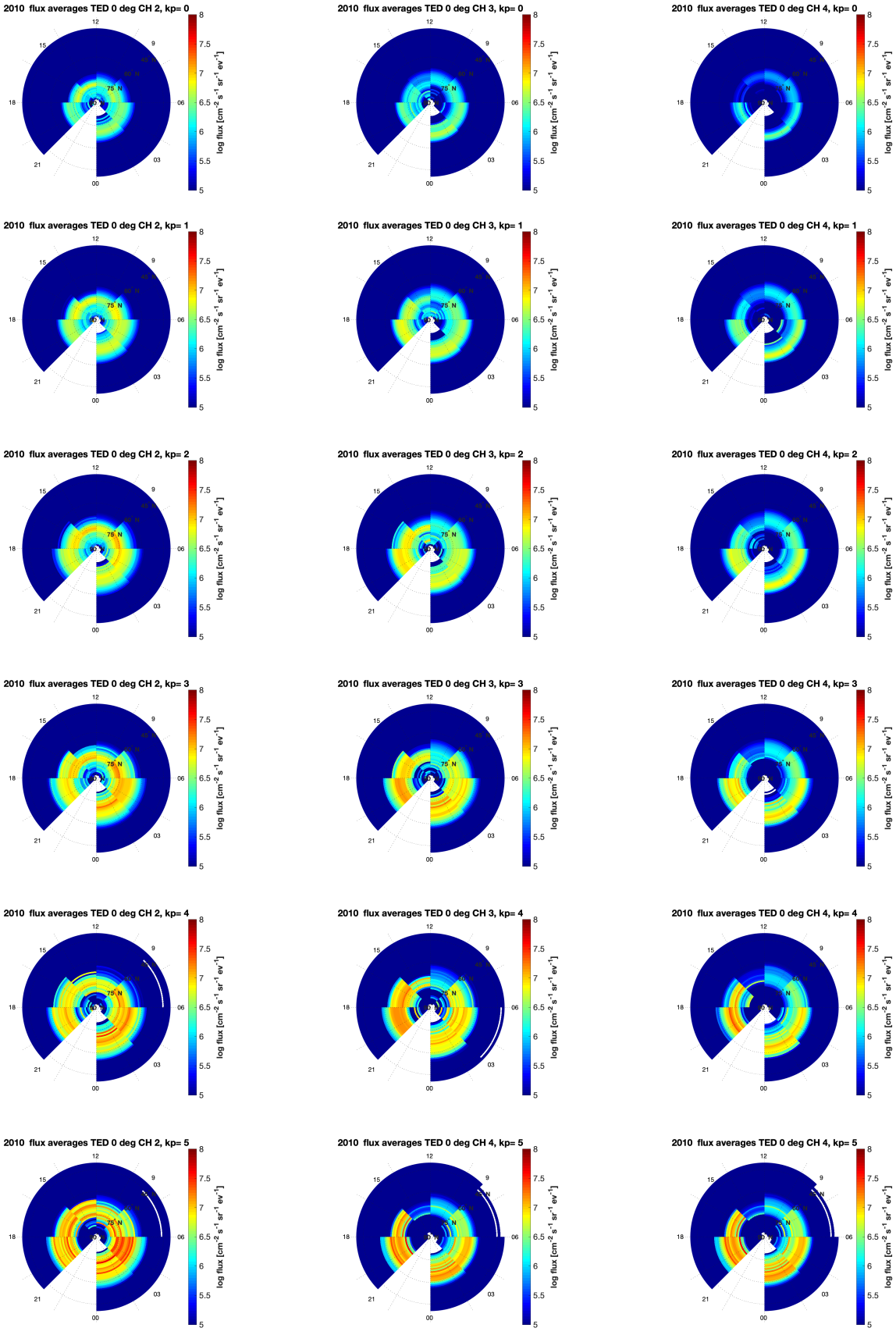

Figure 4.3: Average 1 CGMLAT-3MLT electron flux maps for the 0° TED detector for the year 2010, sorted by Kp, for energy channels 2-4 (see Table 1)

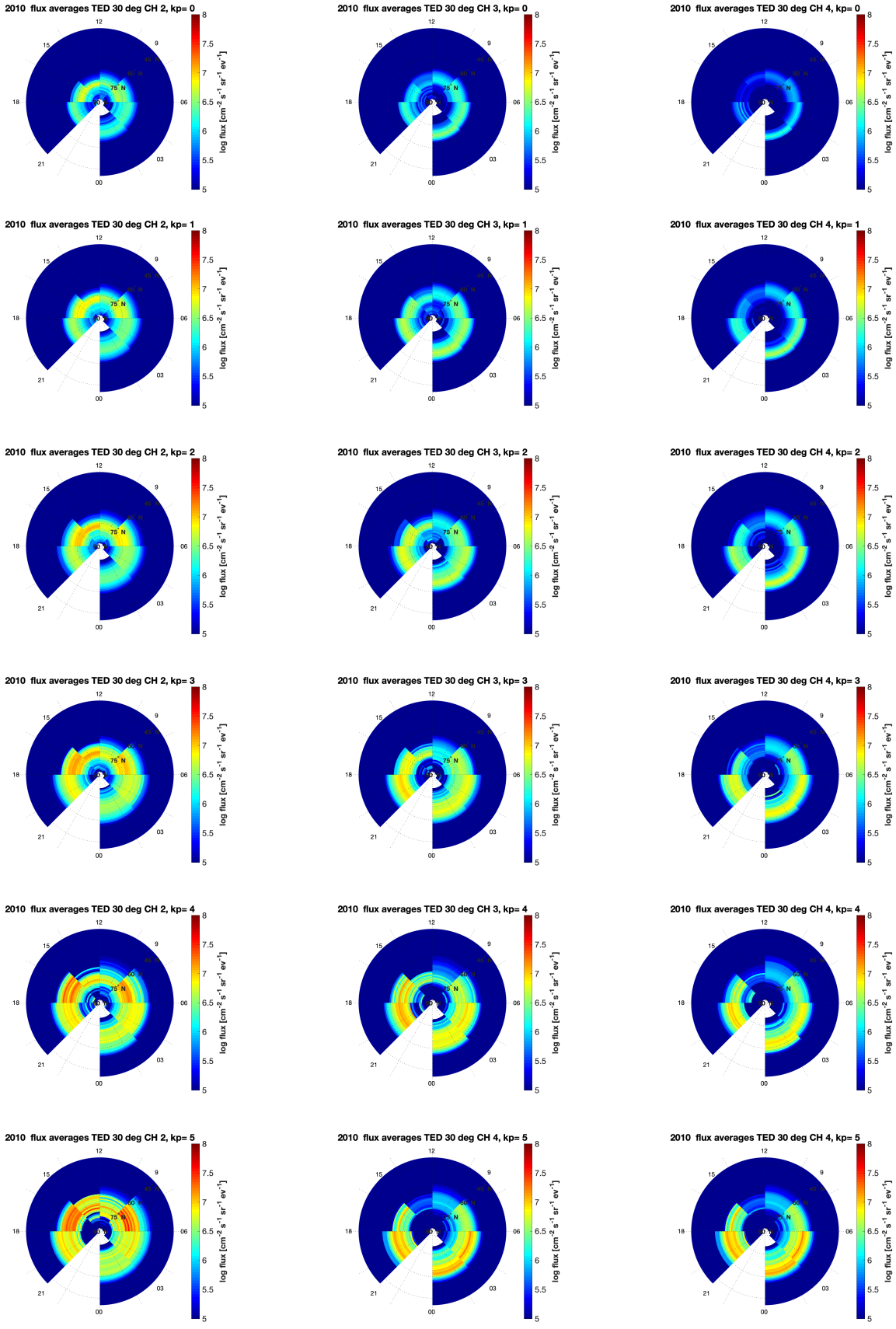

Figure 4.4: Average 1 CGMLAT-3MLT electron flux maps for the 30° TED detector for the year 2010, sorted by Kp, for energy channels 2-4 (see Table 1)

Figure 4.3 and 4.4 shows the electron flux maps for 0° and 30° TED detectors for Channels 2-4 for Kp 0-5 for the year 2010. In relation to the data a noise threshold at $\log_{10}(5)[cm^{-2}s^{-1}sr^{-1}eV^{-1}]$ is implemented. The threshold is chosen with respect to the median of each MLT sector, for both TED and SSJ.

As expected there is a strong relation between the flux and Kp-levels. Higher Kp means higher geomagnetic activity which is related to higher flux levels. Both the overall flux level as well as the latitudinal coverage of flux above the noise threshold increases across all MLTs. For the lower Kp levels (Kp=0,1) fewer latitudinal bands have flux levels higher than the threshold, so the "ring of activity"/auroral oval is significantly smaller and more diffuse than for the higher Kp levels (Kp = 4,5).

In Figures 4.3 and 4.4 there is a clear level of higher flux levels around 75° latitude for both detectors, for all channels, for all Kps, for all MLT sectors. This ring of higher flux starts around the 60° and ends around 80° latitude. Below 60° or close 90° latitude there is mostly just noise. This tracks with the expectations that these low energy electrons are guided in by the magnetic field lines at sub-auroral latitudes/near the poles.

For Channel 3 and 4, for both 30° and 0° detector, there are generally higher flux levels and a wider latitudinal coverage on the night side (18-6 MLT) compared to the dayside (6-18 MLT), which is expected since the auroral electrons originate from the plasma sheet. The lowest flux levels and most limited latitudinal coverage are found between MLT 9-15 for Channel 3 and 4 for all Kps. In particular, between MLT 12-15, there is very limited activity for Channel 4, even during high Kp levels. There is also significantly less activity for Channel 3 in that MLT sector. For Channel 2, however, there is more activity and stronger flux levels on the dayside than night for lower Kp levels. This is especially true for the 30° detector. In Figure 4.4 for TED 30° detector for Channel 2 for Kp=1 there is a clear band at around 75° latitude of higher flux levels over the entire dayside, which eventually breaks up on the nightside. This is in contrast to Channel 3 and 4. Channel 2 also differs from Channel 3 and 4 with respect to the 12-15 MLT sector. While the latitudinal area of activity is less for Channel 2, there is significantly more activity for all Kp levels than for Channel 3 and 4. This is true for both the 0° and 30° detectors. Based on the location and limited energy limit this might suggest that Channel 2 is influenced by precipitation in the cusp [*Heikkila and Winningham*, 1971].

	TED 0 Channel 4 Kp = 1			TED 30 Channel 4 Kp = 1		
MLT	Min $\log_{10}$(flux)	Max $\log_{10}$(flux)	Median $\log_{10}$(flux)	Min $\log_{10}$(flux)	Max $\log_{10}$(flux)	Median $\log_{10}$(flux)
0-3	4.37 [4.36, 4.38]	6.79 [6.76, 6.82]	4.49 [4.47, 4,52]	4.25 [4.17, 4.43]	6.60 [6.57, 6.64]	4.46 [4.41, 4.60]
3-6	4.37 [4.36, 4.38]	6.63 [6.61, 6.64]	4.50 [4.47, 4.53]	4.39 [4.36, 4.44]	6.50 [6.48, 6.51]	4.53 [4.47, 4.62]
6-9	4.45 [4.44, 4.46]	6.30 [6.28, 6.32]	4.50 [4.49, 4.53]	4.43 [4.425, 4.44]	6.28 [6.27, 6.3]	4.62 [4.56, 4.70]
9-12	4.50 [4.48, 4.56]	6.09 [6.08, 6.10]	4.63 [4.61, 4.65]	4.52 [4.51, 4.53]	6.00 [5.99, 6.01]	4.75 [4.71, 4.80]
12-15	4.47 [4.27, 4.49]	5.76 [5.75, 5.78]	4.57 [4.55, 4.59]	4.45 [4.44, 4.46]	5.66 [5.64, 5.68]	4.59 [4.57, 4.63]
15-18	4.42 [4.41, 4.45]	6.12 [6.00, 6.26	4.53 [4.51, 4.56]	4.44 [4.43, 4.45]	5.88 [5.79, 6.00]	4.58 [4.55, 4.63]
18-21	4.54 [4.53, 4.55]	6.56 [6.42, 6.71]	4.61 [4.59, 4.63]	4.49 [4.48, 4.50]	6.30 [6.23, 6.39]	4.71 [4.69, 4.76]

Table 4: Minimum, Maximum and Median $\log_{10}$ flux values with bootstrap 95% confidence intervals(CI) for all 3 MLT sectors for Channel 4 for both TED 0 and TED 30, for Kp = 1.

To investigate potential systematic differences depending on the detectors' pointing direction, a quantitative comparison is listed in Table 4. It lists the minimum, maximum and median log flux values with 95% CI for every MLT sector for both the 0° and 30° TED detectors for energy Channel 4 when Kp = 1. There is no significance difference between the minimum values for both detectors and MLT sectors, with the log flux values being around 4.4. For the median values there is a weak systematic difference, with the log flux values lying between 4.5-4.6 for TED 0° and 4.5-4.7 for TED 30°. For the maximum values, however, there is a clearer MLT pattern. The 0° detector observes systematically higher flux values (>6.5) compared to the 30°detector ($\leq$ 6.3) in the nightside MLT sectors, with no overlapping confidence intervals. It decreases from MLT 0-3 until the 12-15 sector before then increasing again.

Moreover, Figure 4.5 shows the difference, relative to their log value, between the 0° and 30° detector for Channel 2, 3 and 4, sorted by Kp. The left column in Figure 4.5 shows a systematic difference between the 0° and 30° detector for Channel 2 on the dayside, with the 30° detector generally seeing higher flux levels. Here the difference is around 0.2-0.5 or higher in relation to their respective log values. The lower latitudes in the 12-15 MLT sector, however, contrasts this. Here the 0° detector have higher flux levels than the 30° detector possible due to the significant more data points in the 30°detector seen in Figure 4.2. For Channel 3 and 4 there are less clear patterns of differences, however the 0° detector observes in general more activity near the poles on the nightside than the 30° detector. This also true for Channel 2. The difference patterns are clearer and more visible for lower Kps (Kp = 0,1,2), becoming "messier" with increasing Kp (Kp = 3,4,5). This might be due to less data points for the higher Kps, as well as the increase in Geomagnetic activity have the potential to cause issues for instruments and satellites [*Horne et al.*, 2013].

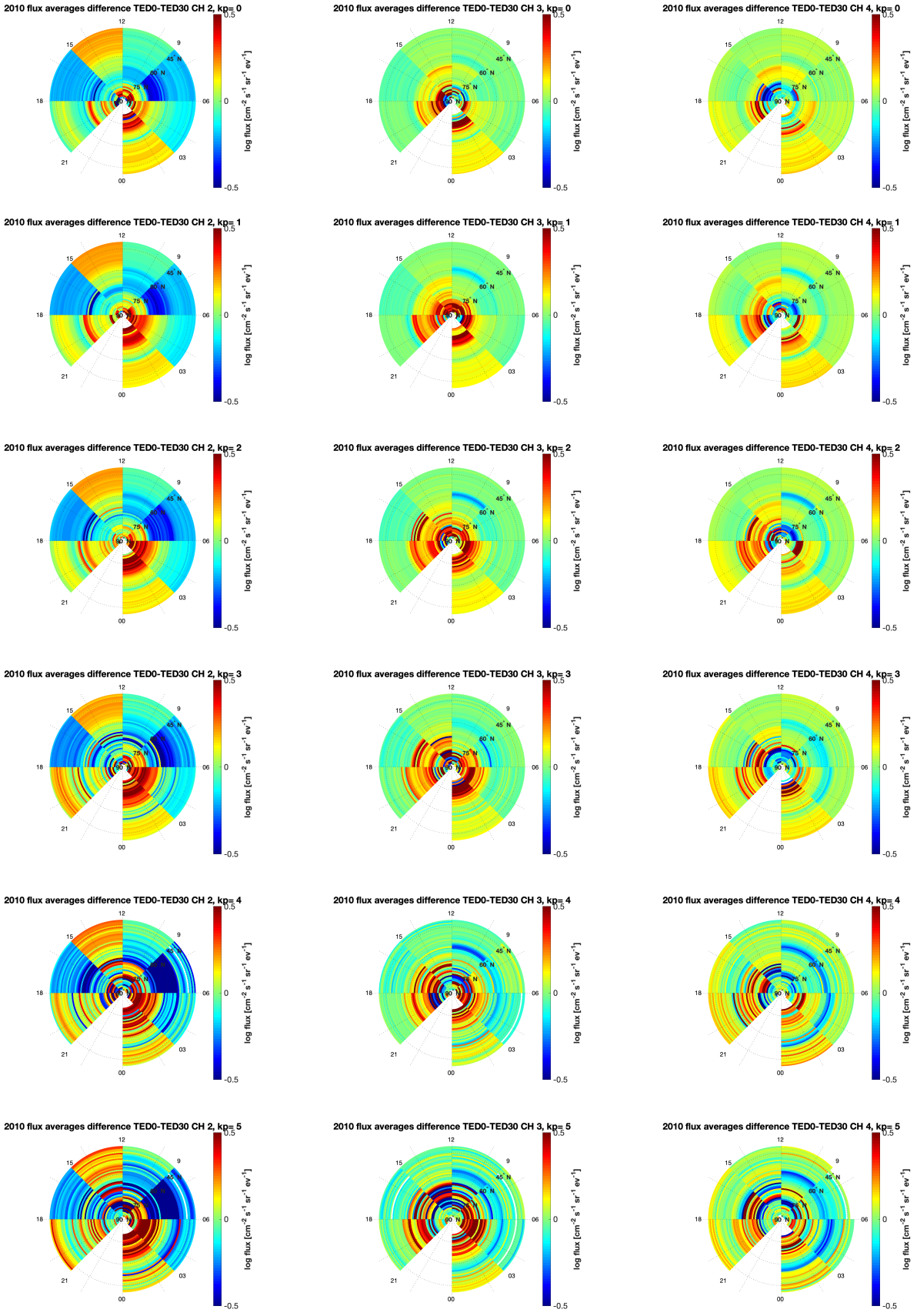

Figure 4.5: Flux difference, relative to their $\log_{10}$ values, TED0-TED30, for the year 2010, sorted by Kp, for Channel 2 (top row) Channel 3 (middle row) and Channel 4 (bottom row)

4.2.2 DMSP

In this subsection the daily Kp-averaged flux data from the DMSP SSJ/4 / SSJ/5 for energy channels 9.45 keV and 6.46 keV (See Figure 3.5) are evaluated in respect to MLT, CGM latitude and Kp dependence. Channel 9.45 keV and 6.46 keV ranges between 7.590-11.310 keV and 5.1975-7.7225 keV respectively. They are chosen due to overlapping energy ranges with Channel 4 for TED, and will for now on be referred to by their centred energy.

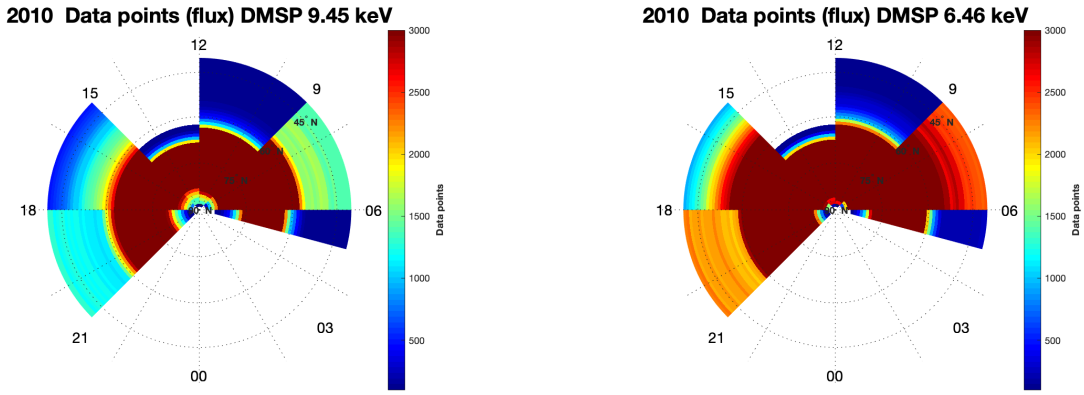

Figure 4.6: Coverage and statistics maps for DMSP/SSJ 9.45 keV (left) and DMSP/SSJ 6.46 keV (right) for the year 2010

Figure 4.6 shows the 1°MLAT and 3 hour MLT coverage for the DMSP/SSJ data during the year 2010 for energy channels 6.46 keV and 9.45 keV. Between 21-05 MLT there is no or relatively little DMSP/SSJ data. The poor coverage is also demonstrated by the satellite trajectories in Figure 3.3. There is also a lack of coverage for MLT sector 12-15 for latitude 60° and below.

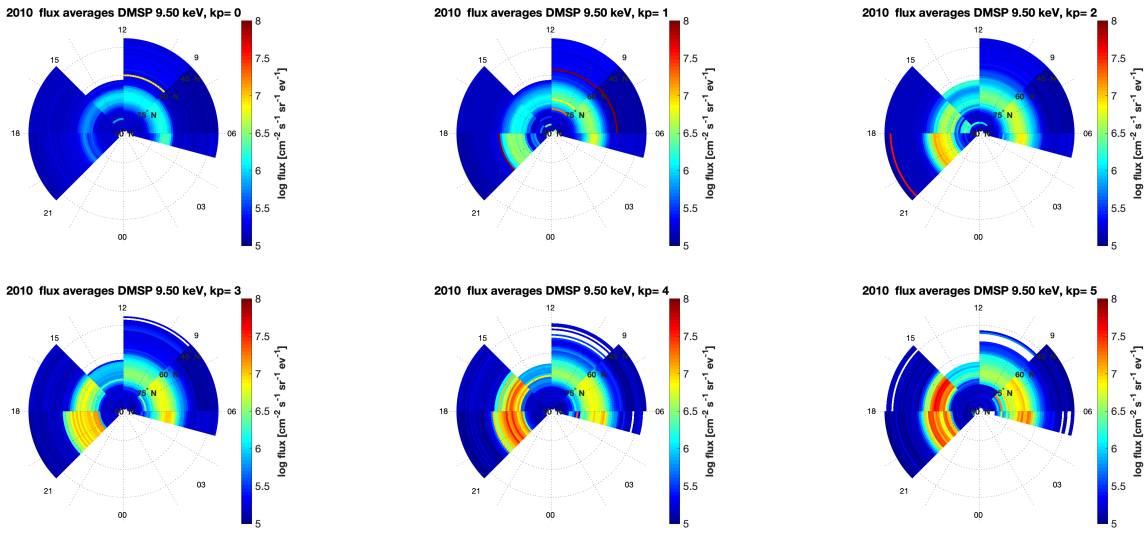

Figure 4.7: Average electron flux maps for the DMSP/SSJ 9.45 keV Channel for the year 2010 at 1° CGMLAT and 3 MLT resolution, sorted by Kp

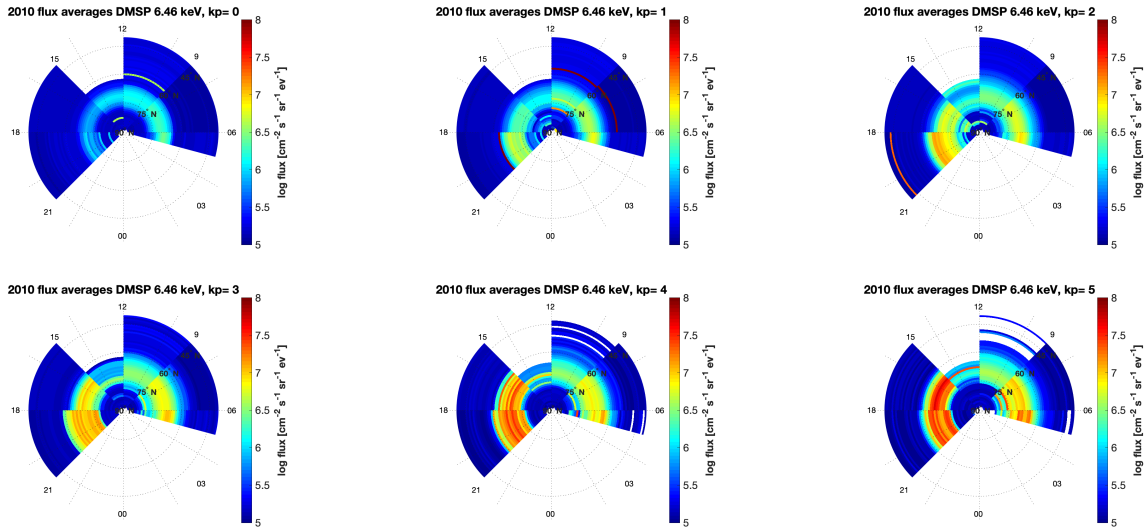

Figure 4.8: Average electron flux maps for the DMSP/SSJ 6.46 keV Channel for the year 2010 at 1° CGMLAT and 3 MLT resolution, sorted by Kp

Figure 4.7 and 4.8 show flux maps for the DMSP/SSJ channels 6.46 keV and 9.45 keV (see Figure 3.5) for the year 2010, sorted by Kp. They are plotted on an identical grid as the TED flux data, with the same noise threshold at around $\log_{10}(5)[cm^{-2}s^{-1}sr^{-1}eV^{-1}]$. Their energy ranges overlaps with Channel 4 for TED (6.503-9.457 keV, see Table 1). Analogue to the observed TED fluxes, and as expected, there is a strong positive relation between

Kp and the flux level. Both the strength of the flux levels and size of the latitudinal area show a pronounced increase with Kp, again similarly to TED.

Figures 4.7 and 4.8 shows that both energy channels detects significantly less activity and lower flux levels around noon (MLT sectors 9-12 and 12-15), than on the dusk side (15-18 and 18-21 MLT sectors) or dawn side (3-6 and 9-12 MLT sectors). For lower Kps (Kp=0,1) there is generally higher flux levels on the dawn side than on the dusk side. However, the dusk side has a stronger response to increasing Kp. Hence, for the higher Kps (Kp=4,5) the dusk side has the strongest and widest flux bands.

Figures 4.7 and 4.8 shows a clear band of enhanced flux levels for latitudes between 60° and 75° for all MLT sectors and all Kps. Which again corresponds with our expectation of these low energy electrons being guided into the atmosphere by the magnetic field at sub-auroral latitudes. Similarly to TED, there is mostly just "noise" for latitudes below 60°.

4.2.3 TED vs DMSP flux maps

In this subsection Kp-averaged flux values for the year 2010 from energy Channel 4 from POES/TED will be compared to energy Channel 9.45 keV and 6.46 keV from DMSP/SSJ. Potential MLAT and MLT differences, as well any difference in response to increased geomagnetic activity, will be explored. Differences in respect to flux intensity inside the auroral oval, the latitudinal width of the auroral oval or the response for specific MLT sectors will be highlighted.

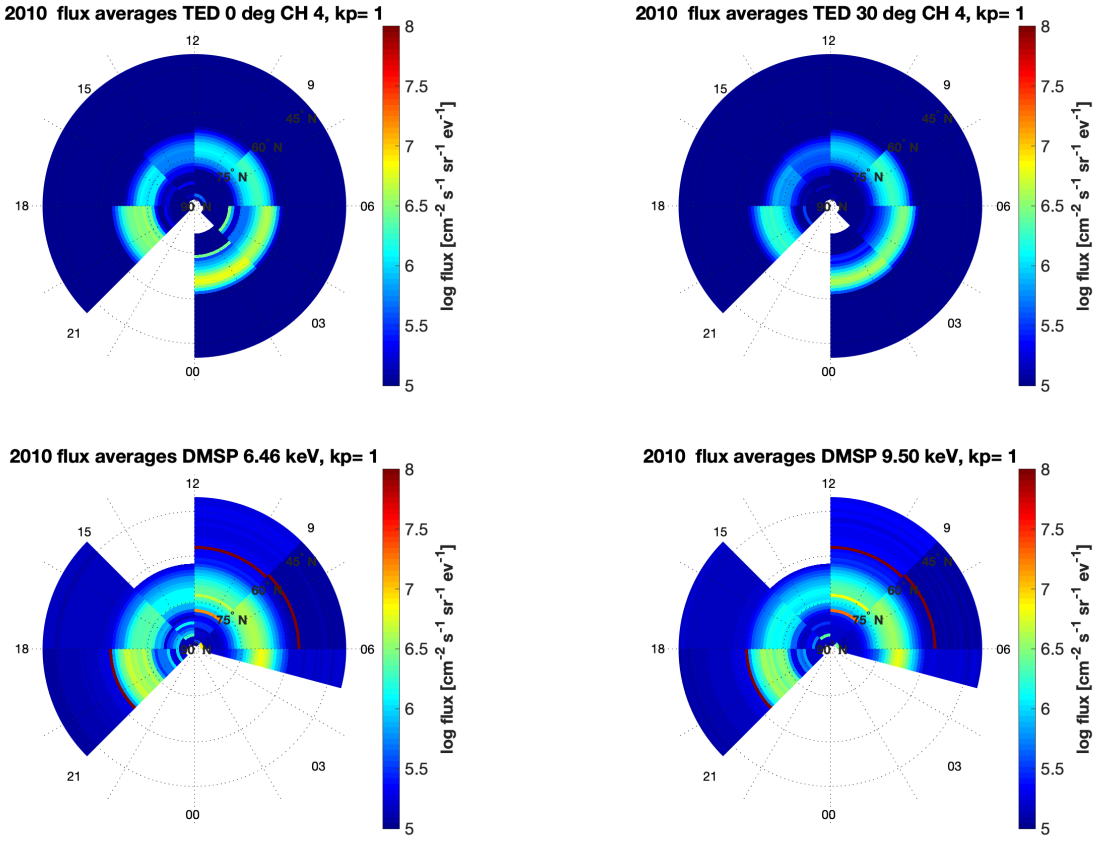

Figure 4.9: Average 1 MLAT vs 3 MLT electron flux maps for Kp = 1 for CH 4 TED 0° and 30° and DMSP/SSJ 6.46 keV and 9.50 keV

Figure 4.9 shows average flux maps for Kp = 1 for TED 0° and 30° (top row) for Channel 4 and DMSP/SSJ channels 6.46 keV and 9.45 keV (bottom row). Kp = 1 is the daily Kp level with best statistic, see Figure 4.1. Figure 4.9 reveals that the DMSP channels generally detects higher flux levels for latitudes below 60°, equatorwards of the auroral oval. Here the TED detectors detect $\log_{10}$ flux values between 4-5, while DMSP/SSJ observe $\log_{10}$ flux values above 5. Both POES and DMSP detectors measure higher flux levels for the night side (18-06 MLT) compared to the dayside. However, due to the lack of coverage in these sector by the DMSP one has to be careful not drawing too many conclusions. While both SSJ and TED observe weaker fluxes on the day side (6-18 MLT), there is a visible difference between the detectors. Both SSJ channels measure higher flux levels and more activity than the two TED detectors. The band including higher flux levels (between 60°-75° CGM latitude) from MLT 6 to MLT 18 in Figure 4.9 becomes smaller and significantly more diffused for both TED detectors, in particular for the TED 30° detector. For both 0° and 30° detector, the MLT sector 12-15 seem to disrupt the continuity of the band of stronger flux. This is less apparent in the DMSP detectors. While the flux band decreases in strength, the decline is less prominent compared to the TED detectors.

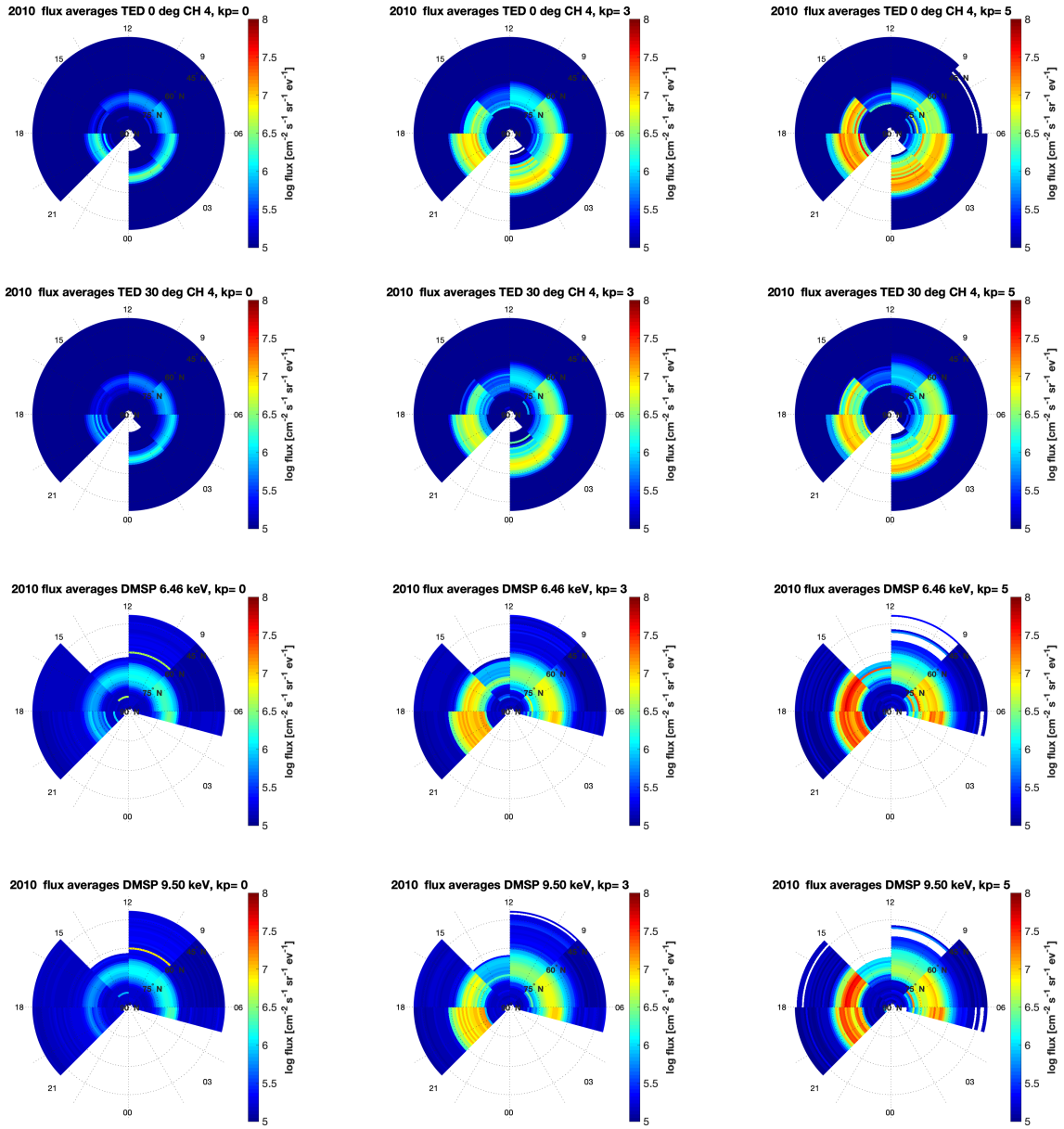

Figure 4.10: Average 1 MLAT vs 3 MLT electron flux maps for Kp = 0,3,5 for CH 4 TED 0° and 30° and DMSP/SSJ 6.46 keV and 9.50 keV

Figure 4.10 shows flux maps for Channel 4 for both TED detectors and both DMSP/SSJ channels for Kp = 0,3,5 to compare the difference in response to geomagnetic activity. Both the 9.45 keV and 6.46 keV SSJ channels observe stronger fluxes than Channel 4 at TED 0° and 30° detectors at all Kp-levels. Moreover, the SSJ detectors respond stronger to increasing Kp than the two TED detectors. Specifically for between MLT 15 and 21, the DMSP observations increase from flux levels close to the threshold, to three orders of magnitudes higher. The response is not just in intensity of the enhanced flux band, but

also the latitudinal extent. This implies that the DMSP satellite detect more activity for lower latitudes in these MLT sectors at higher Kp than TED.

There is also a systematic MLT-difference between the POES and DMSP measurements. For Kp = 0, DMSP/SSJ observes the strongest activity on the dayside, with a clear continuous band of higher than threshold flux levels below 75° latitude, which "disappears" and becomes more diffused entering the night time sectors (MLT 15-18 and 18-21). For Kp=0, the TED detectors observe stronger fluxes on the night side compare to the day side. Moreover, the sectors around noon (9-12 and 12-15 MLT) also shows noticeable difference in response to increasing geomagnetic activity (Kp=3,5). DMSP/SSJ experiences a noticeable increase in flux levels with increasing Kp. TED, in contrast, observe barely any increase in flux levels, both in terms of intensity and latitudinal extent, in the same MLT sectors.

To further compare the flux differences between the DMSP and POES detectors, difference maps, one relative to their respective log values and one as the relative difference between the detectors, have been made for MLTs between 6-21. The 6-21 MLT sector is chosen due to good coverage for both satellites. The difference maps makes it easier to study potential latitudinal differences between the detectors and energy channels, as well as their response to increase in geomagnetic activity. Figure 4.11 shows the log flux difference between TED 0°and the two DMSP/SSJ channels (the two uppermost rows), and TED 30°and the two DMSP channels (the two lowermost rows) for Kp = 0,3,5. The blue colour indicates that DMSP observes higher fluxes compared to POES and red colour mark the opposite relation. Figure 4.12 shows the relative difference between the two TED detectors and the two SSJ channels for Kp=0,3,5, normalised by the fluxes measured by the TED detectors, respectively. Hence, Figure 4.12 illustrates the percentage increase/decrease the fluxes observed by DMSP/SSJ fluxes are compared to the fluxes observed by the TED detectors. Again blue indicates $\text{flux}_{SSJ} > \text{flux}_{TED}$ and red indicates $\text{flux}_{SSJ} < \text{flux}_{TED}$. Tables with the relative differences, from the day- and nightside, between the detectors, inside the auroral oval, have also been made for further quantitative comparison. Table 5 and 6 show the relative differences between the DMSP/SSJ channels and TED detectors for CGM latitudes 65°-75°, MLT sector 6-9 and 18-21, for Kp = 1 and 5. The MLT sectors are chosen due to good overlapping coverage between the TED detectors and the DMSP/SSJ, and the fact they represent day- and nightside.

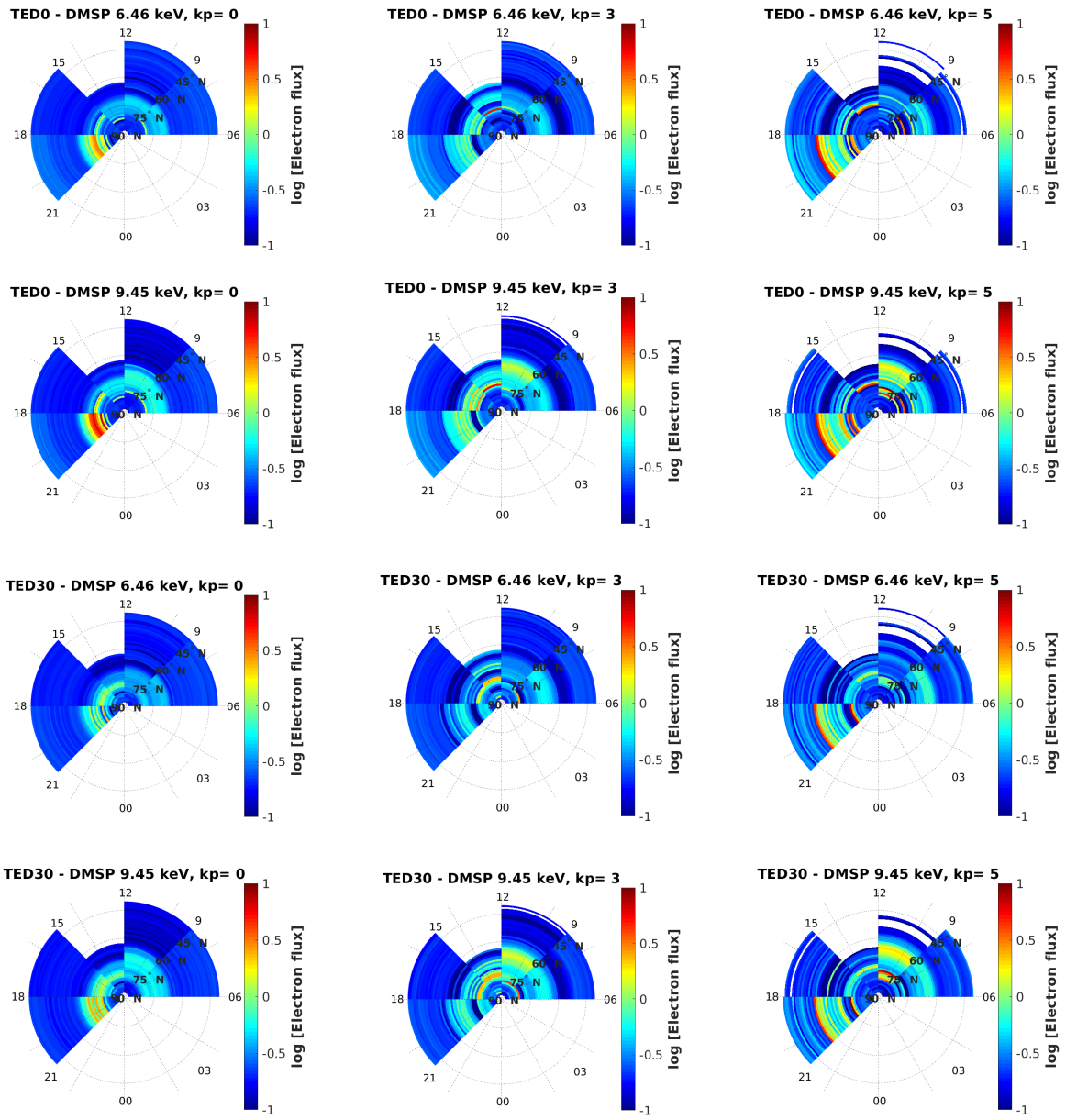

Figure 4.11: Difference, relative to their respective log values, between the two TED detectors and the two DMSP/SSJ channels. From the top row to bottom row: TED0-DMSP6.46 keV, TED0-DMSP9.45keV, TED30-DMSP6.46keV and TED30-DMSP9.45keV

The difference between the two detectors for day- and nightside low geomagnetic activity is highlighted in Figures 4.11 and 4.12. For MLT sector 18-21 and Kp = 0, the TED detectors detect consistently higher average flux values than those observed by the DMSP/SSJ for latitudes between 60° and 75° CGM, which corroborates the prominent features of Figure 4.10. Figure 4.12 quantifies it to be up to ∼10%. This difference is less prominent for higher levels of Kp. Table 5 and 6 validates that there is a significant contrast in respect

to the relative flux differences in the CGM latitude band 65°-75°. For Kp = 1, the relative difference in favour of the fluxes observed by DMSP/SSJ is minimum 4.6% for MLT 6-9. However, the relative flux difference can go as low as -1.3% in the MLT sector 18-21 compared to the TED 0° (minus meaning the TED 0° detector sees higher flux values than the DMSP/SSJ channel). For Kp = 5, a similar the pattern is found. The DMSP/SSJ detectors observe higher average flux values for MLT 6-9, while the difference becomes more equal for MLT 18-21, especially relative to the TED 0° detector.

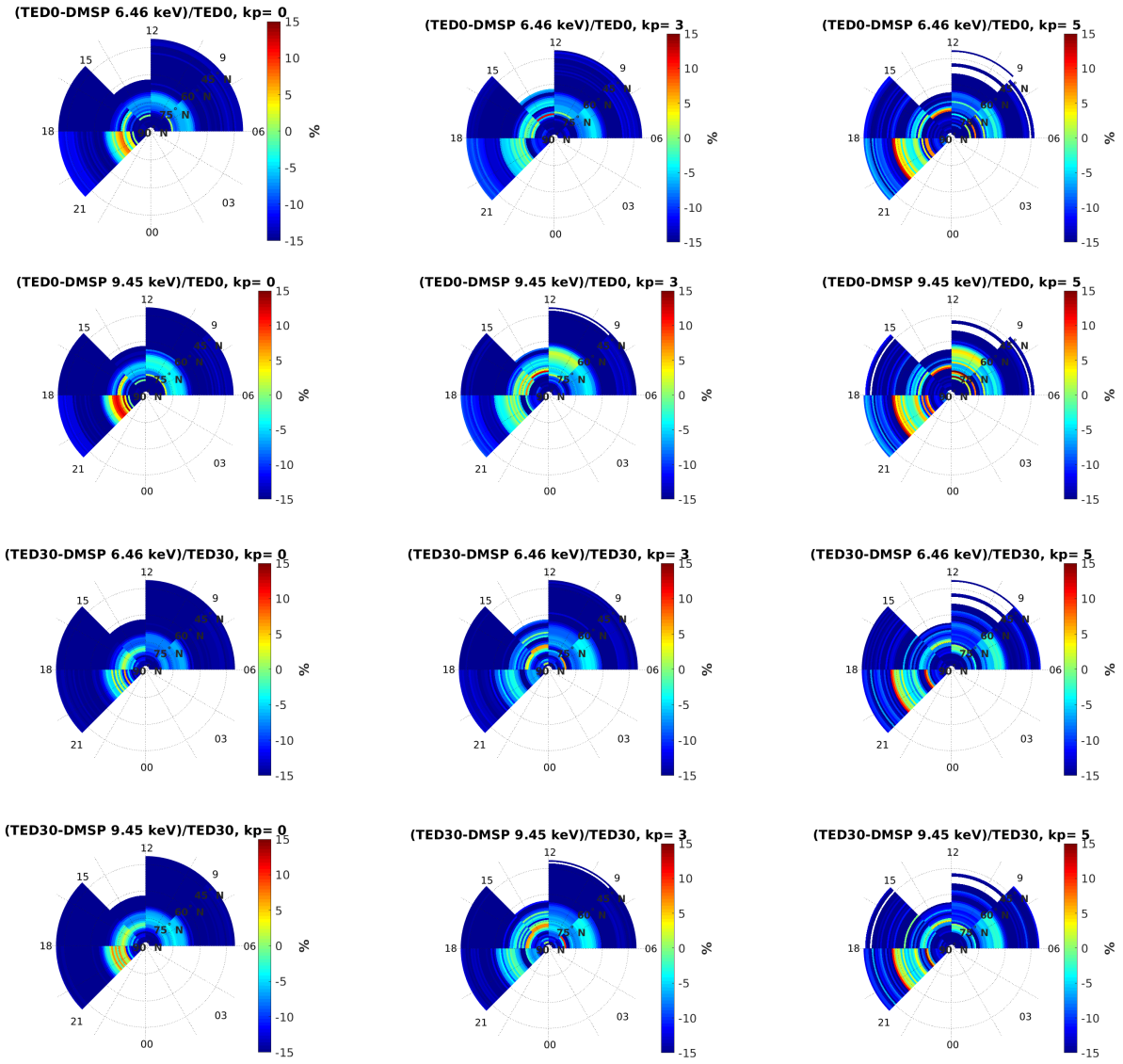

Figure 4.12: Relative difference between the two TED detectors and the two DMSP/SSJ channels. From the top row to bottom row: (TED0-DMSP6.46 keV)/TED0, (TED0-DMSP9.45keV)/TED0, (TED30-DMSP6.46keV)/TED30 and (TED30-DMSP9.45keV)/TED30

The consistently higher flux levels for the lower latitudes (below the aurora oval) for the

DMSP channels is shown in Figures 4.11 and 4.12, with the relative difference often 15% higher in favour of the DMSP/SSJ. Here the DMSP/SSJ channels sees $\log_{10}$ flux values $\sim$5, while TED observes $\log_{10}$ values $\sim$4. Moving towards latitudes between 60-80°, the sign is less consistent. The DMSP/SSJ observes on average higher flux values for most 1° CGMLat bands, especially for the 6.46 keV channel. However, between 60° and 80° CGM latitude, the sign becomes less clear, and there are several latitude bands where the POES observe higher flux levels, even for high Kp levels. For MLT 6-9, the relatively difference inside this band falls between 4-8% higher for DMSP/SSJ relatively to TED for Kp = 0, 1 and 3, seen in Figure 4.12 and Table 5. Relative difference of around 4-8% inside the auroral oval in favour of the DMSP/SSJ channels holds for almost all MLTs, except for MLT 18-21. Here the TED observes latitude bands with significantly higher flux values, especially for Kp = 0 and for DMSP energy Channel 9.45 keV.

Towards the boundaries (60° and 80° latitude), the DMSP/SSJ detects consistently higher flux values than TED. This corresponds with was seen in the average flux maps, where the DMSP/SSJ, with the exception of MLT sector 18-21, observed more response to geomagnetic activity towards the auroral oval boundaries, see Figure 4.10.

	MLT 6-9 Kp = 1				MLT 6-9 Kp = 5			
MLAT°	D6-T0/T0 [%]	D9-T0/T0 [%]	D6-T30/T30 [%]	D9-T30/T30 [%]	D6-T0/T0 [%]	D9-T0/T0 [%]	D6-T30/T30 [%]	D9-T30/T30 [%]
65	8.2	8.9	7.1	7.8	2.6	3.2	2.1	2.72
66	5.7	6.1	5.5	5.9	3	3.5	2.8	3.2
67	5.2	5.3	5	5.2	6.7	6.9	5.7	5.95
68	4.6	4.5	4.6	4.6	6.2	5.7	5.8	5.3
69	4.9	4.6	5.1	4.8	5.9	5.5	5.4	5
70	4.95	4.3	5.2	4.5	3.8	3.2	5.95	5.34
71	5.98	4.9	6.1	4.9	9.1	6.8	9.7	7.4
72	6.7	5.2	6.8	5.3	-1.7	-2	7	6.7
73	7	5.1	7.4	5.4	9.6	9.9	7.8	8.1
74	6.7	4.4	7.4	5	12.9	8.5	14.1	9.7
75	7.5	5.1	7.8	5.4	17	16.4	20.3	19.7

Table 5: Difference between DMSP/SSJ and TED relative to TED (in percentage), MLT sector 6-9, latitudes 65-75°, for Kp = 1 and 5. D6 = DMSP 6.46 keV, D9 = DMSP 9.45 keV, T0 = TED 0° and T30 = TED 30°

The difference maps further shows the increased response of the DMSP/SSJ channels compared to TED to increasing geomagnetic activity. The fluxes observed with DMSP/SSJ increase relative more than TED as seen in the maps in Figures 4.11 and 4.12, where the flux difference becomes bluer with increasing Kp. Table 5 and 6, show a contrast for the relative differences for the two ends in response to increased geomagnetic activity. For Kp=5 the discrepancy significantly increases polewards, while decreasing equatorward. At 75° latitude for MLT 6-9, the relative difference increases from between 5-8% to between 16-20%. For MLT 18-21 the relative difference to TED 0° increases from under 2% to between 10-13%, while relative to TED 30° the difference goes from 7.5% to between 10-13%. For 65° however, the relative difference significantly decreases. From 7-9% to 2-3% for MLT 6-9 and from 7.4-12.7% to under 4% for MLT 18-21. This implies the POES/TED and DMSP/SSJ has a latitude dependent response to increased geomagnetic activity. The decrease of the relative difference might suggest pitch angle isotropy at these latitudes during strong activity implying that the fluxes observed a less dependent on the detector's

pointing direction. Similarly, and increase of the discrepancy might suggest strong pitch angle anisotropy where the different pointing directions of the detectors result in different flux observations. This explanation is given further credibility by the discrepancy between the two TED detectors for MLT 18-21, which can be seen in Table 6 and Figures 4.11 and 4.12. The differences relative to TED 0° is consistently lower than the difference relative to TED 30°. This discrepancy holds for almost all latitudes for Kp = 1 and Kp = 5, which affirms the patterns seen in the TED difference maps, see Figure 4.5. At the equatorward end (65° and 66°) for Kp = 1, the difference relative to the 0° detector is between 5.1-7.9%, while for the 30° detector the relative difference is between 10.2-13.1%. Towards the poleward end the relative difference to TED 0° is around 0-1% and for TED 30° its over 7%. In the middle of this latitude interval, the difference relative to TED 0° hovers around 0% for DMSP 9.45 keV and 1-2% for DMSP 6.46 keV. For the relative difference to TED 30° it is above 4% for DMSP 9.45 keV and above 5% for DMSP 6.46 keV.

	MLT 18-21 Kp = 1				MLT 18-21 Kp = 5			
MLAT	D6-T0/T0 [%]	D9-T0/T0 [%]	D6-T30/T30 [%]	D9-T30/T30 [%]	D6-T0/T0 [%]	D9-T0/T0 [%]	D6-T30/T30 [%]	D9-T30/T30 [%]
65	7.8	7.4	12.7	12.2	3.7	3.7	3.8	3.8
66	7.9	5.12	13.1	10.2	2.9	2.2	6.4	5.7
67	4.2	2,2	10	7.8	3.7	2.4	3.2	1.9
68	5	3.6	8.3	6.8	4.5	2	7.7	5.1
69	3.8	1.5	7.1	4.75	-0.18	-0.4	2.7	2.5
70	2.5	0.7	6.2	4.4	-1.71	-5.6	0.5	-3.4
71	2	0.7	5.3	4	-0.49	-5	4.4	-0.3
72	0.8	-1.3	5.2	3	5.5	3.9	9.6	8
73	0.4	-0.51	5.2	4.3	12	10.6	16	14.5
74	1.7	-0.3	8.8	6.7	-2.4	-6.8	14	8.8
75	1.8	1.9	7.5	7.6	12.9	9.9	13.6	10.6

Table 6: Difference between DMSP/SSJ and TED relative to TED (in percentage), MLT sector 18-21, latitudes 65-75°, for Kp = 1 and 5. D6 = DMSP 6.46 keV, D9 = DMSP 9.45 keV, T0 = TED 0° and T30 = TED 30°

4.2.4 TED vs DMSP electron flux spectra

To further explore differences and similarities between the DMSP/SSJ and POES/TED observations, electron flux energy spectra are created for each MLT sector, for all daily Kp levels and for latitudes 60° and 75°. The latitudes are selected to potentially unravel features related to different magnetospheric origin, e.g. plasma sheet versus ring current or radiation belts. Figure 4.13 shows electron flux energy spectra for MLT 6-9, sorted by Kp. The points with an "o" around them represents the 60° and the ones without represents 75°.Red is TED0, blue is TED30 and black is SSJ. The POES/TED channels 1-4 (see section 3.2 and Table 1) covers the similar energy range as DMSP/SSJ channels 4-15 (see section 3.3 and Figure 3.5). The error bars along the x axis represents their energy range, centred on each channels respective middle energy. The error bar along the y-axis represents the bootstrap 95% confidence intervals (see section 3.1) for the calculated averages.

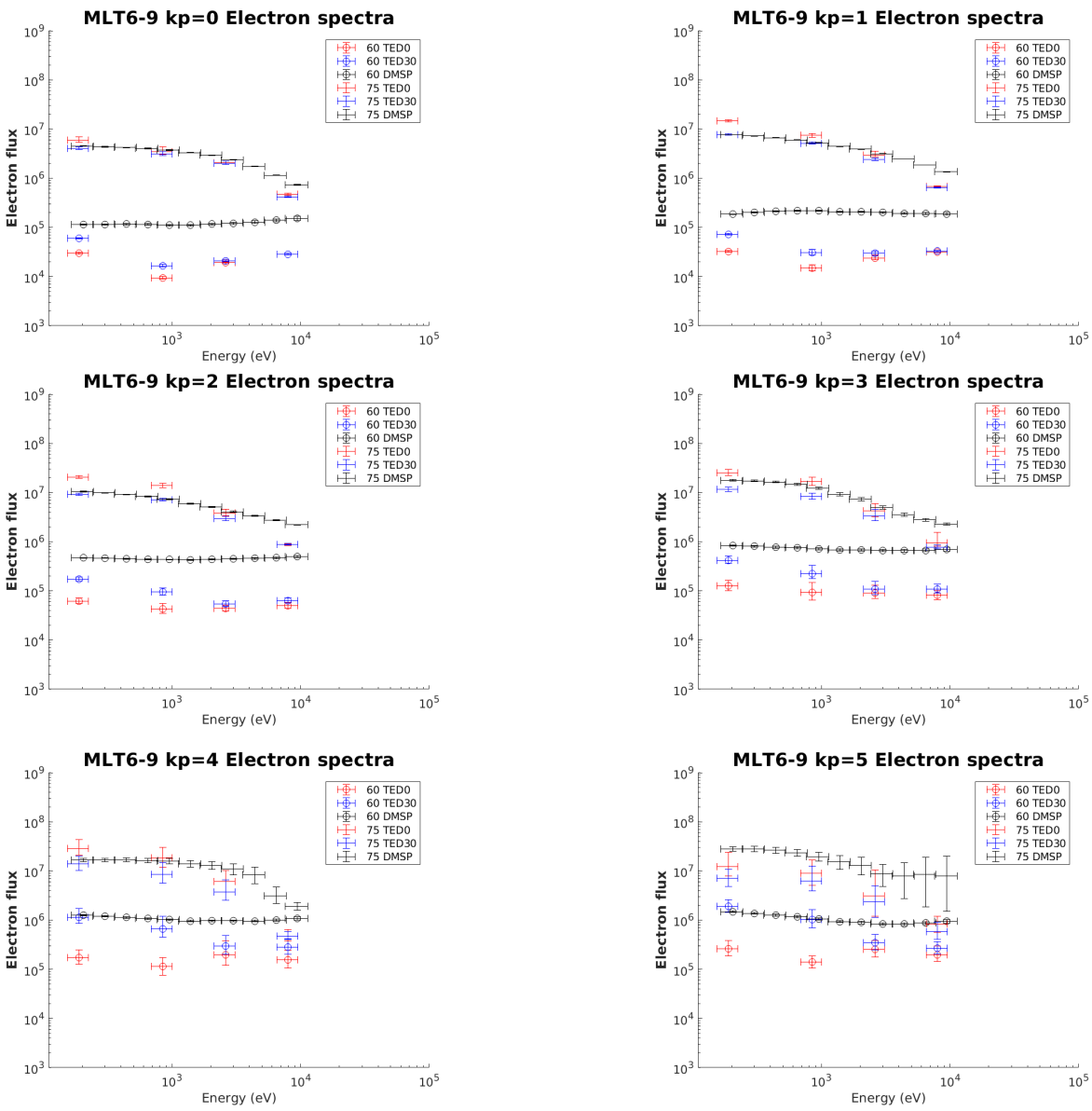

Figure 4.13: Electron flux energy spectra for MLT sector 6-9, for latitudes 60° and 75°, for all daily Kps (0,1,2,3,4,5). The points with an 'o' around them is 60°, while the ones without are 75°. Red represent TED 0, blue TED 30 and black DMSP. Channels 1-4 (see Table 1) are plotted for TED 0° and 30°, while for DMSP energy channels 4-11 (see Figure 3.5). The error bars along y-axis are 95% confidence intervals, and the error bars along x-axis are the range of the respective energy channel.

Consistently for all Kps, the DMSP/SSJs observes higher flux values compared to the POES/TED 0° and 30° for the 60° latitude averages, by more than half an order of magnitude. Independent of the Kp-value the energy spectra resemble a fairly flat distribution consistent for all three detectors. While the DMSP/SSJ flux levels is consistently higher for 60° latitude for all Kp, the gap between them is, however, decreasing with Kp, in

particular for TED 30°. At 75° latitude there is not a consistent trend in regard to which detector, SSJ or TED, measures the highest fluxes, neither for the entire energy bands nor for different Kp levels. There is, however, a consistency between the TED detectors, in that the TED 0° observe higher fluxes than the TED 30° for 75° latitude, for all Kps and channels. There is noticeable energy dependence between the TED detectors and the DMSP channels, distributions. The DMSP has a stronger "tail", while the TED drops off more steeply with increasing energy. For increasing Kp, the tail is weakened for TED and the fall between the lower energy channels (Channel 1,2,3) and the "high" energy Channel 4 steepens.

The latitude bands, 60° and 75°, falls on the edge of best coverage for all three detectors, see Figure 4.2 and 4.6. Hence, electron flux spectra for a latitude band that target the best statistics, and the heart of the auroral oval has been made. Figure 4.14 shows electron spectra for latitude 67° for MLT 6-9 for all Kp levels. Similarly for Figure 4.13, TED 0° is red, TED 30° is blue and DMSP/SSJ is black.

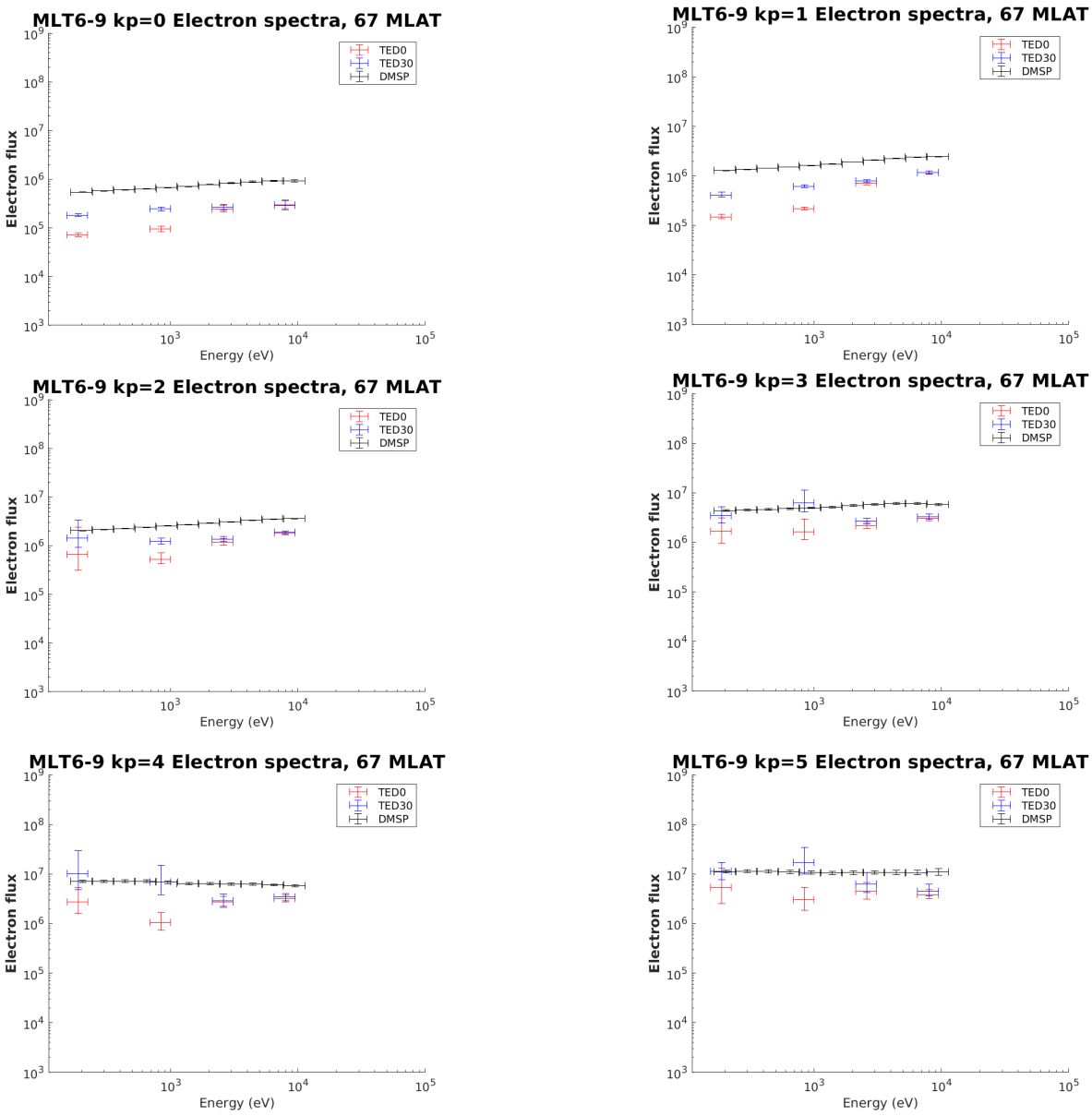

Figure 4.14: Electron flux energy spectra for MLT sector 6-9, for latitude 67° for all daily Kps (0,1,2,3,4,5). Red represent TED 0, blue TED 30 and black DMSP. Channels 1-4 (see Table 1) are plotted for TED 0° and 30°, while for DMSP energy channels 4-11 (see Figure 3.5). The error bars along y-axis are 95% confidence intervals, and the error bars along x-axis are the range of the respective energy channel.

Here, the slope as function of energy acts differently between the lower Kp levels (0,1,2) and the higher (3,4,5), consistently for all three detectors. For the lower Kp levels flux levels slope upwards with increasing energy. Meaning the high energy channels (Channel 4 for TED and 9.45 keV for DMSP) for all three detectors sees higher average flux levels than the lowest energy channels (Channel 1 for TED and 0.204 keV for DMSP). In other

words the peak average flux value is located at the high energy channels for Kp = 0, 1 and 2. For the higher Kp levels, the peak is more around the middle energy, 1-2 keV, and the flux level somewhat decreases on either end.

For Kp = 0 and Kp = 1 DMSP is consistently higher for all energies than the two TED detectors. For the higher energy channels (TED Channel 3 and 4), this stays true for Kp levels above 1. The DMSP also sees higher flux levels than TED 0° for all energies and Kp levels. For TED 30°, however, the low energy channels (1 and 2) sees flux levels above or similar to the DMSP in the same energy ranges for Kp above 1.

The shape of the electron spectra for all MLT sectors is examined applying a best fit assuming of a Maxwellian, power law and exponential distribution (see section 3.1.1). Their goodness of fit were evaluated on their respective SSE and adjusted R-square values (see section 3.1.1). The best fit was selected based on the lowest SSE and highest adjusted R-square. In this study, however, most emphasis is put on the fits SSE values, as the distributions usefulness for prediction of the electron flux spectra are of most interest. Often in studies looking at fits for electron flux spectra, only SSE (or variations of it) is reported, e.g. *McIntosh and Anderson* [2014]. The fits are done over the entire energy spectrum for each MLT sector and Kp level.

Figure 4.15 shows examples of good fits for the different distributions. Figure 4.16 shows best fits as a percentage of all MLT sectors at the latitudes 60°, 67° and 75°. Table 7 shows the best fits as a percentage of all Kp levels for each MLT sector for CGM latitude 75°

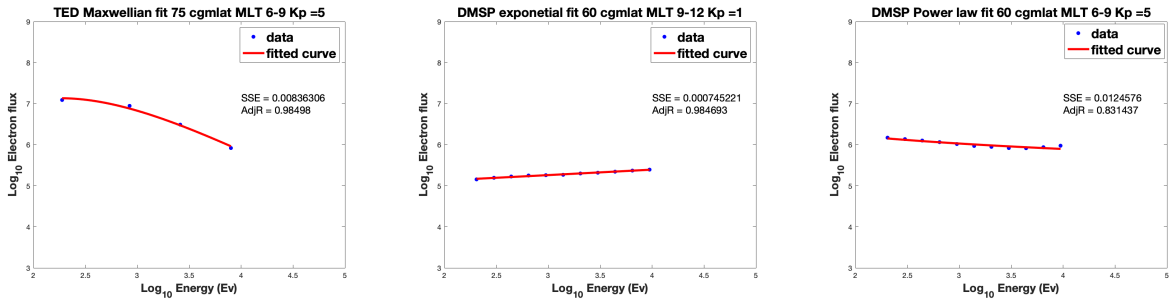

Figure 4.15: Examples of best fits for Maxwellian, exponential and Power law distributions with their respective SSE and adjusted R-square values

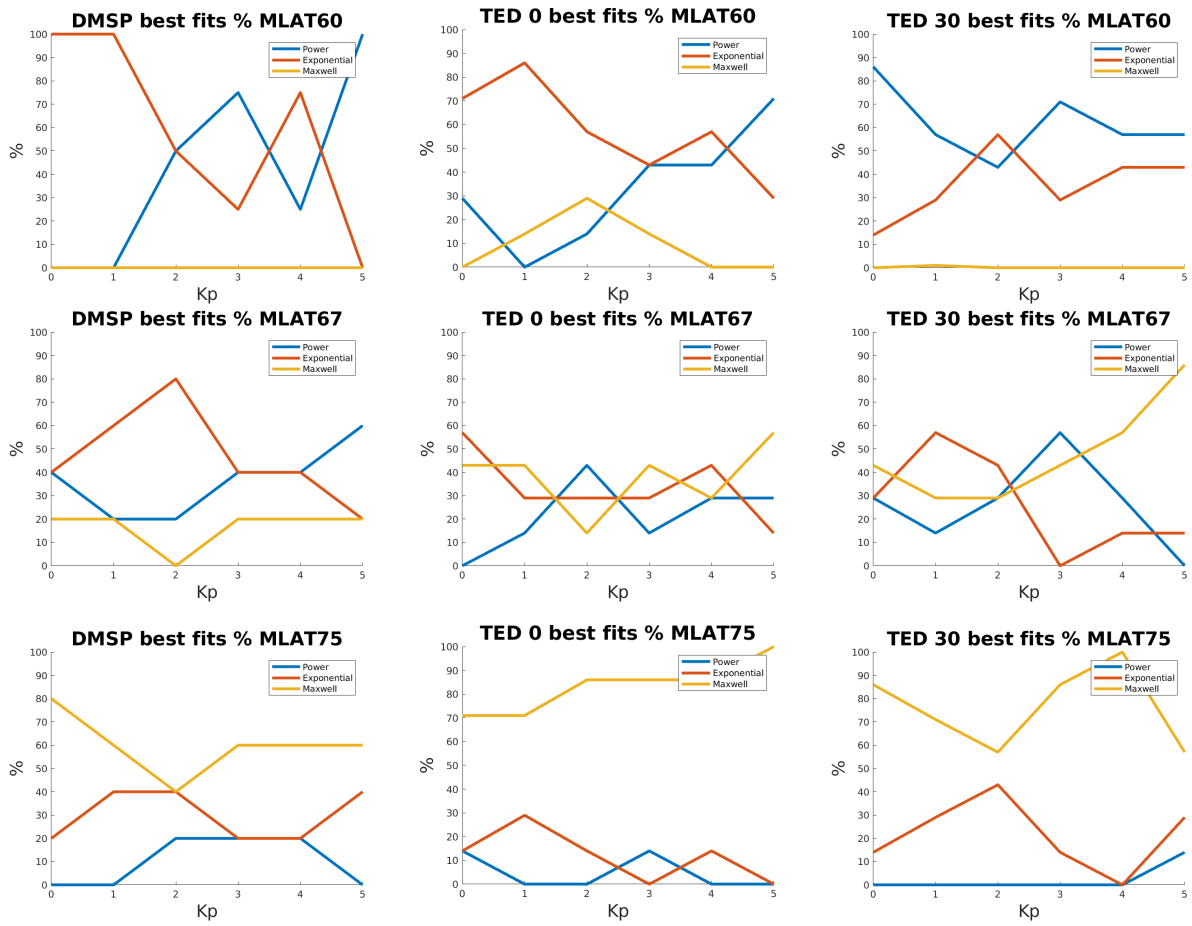

Figure 4.16: Best fits to electron spectra as percentage of Kp for DMSP (left), TED 0° (middle) and TED 30° (right) for CGM latitude 60° (top row), 67° (middle row) and 75° (bottom row). The distributions fitted with is Maxwellian (yellow), exponential (red), power law (blue).

In Figure 4.16 there is a clear contrast between 60° and 75° for the Maxwellian distribution. For all Kp levels and all detectors, the Maxwellian goes from being the distribution with least amount of best fits for 60° to the one with most amount of best fits for 75°. For the majority of MLT sectors and Kp levels the Maxwellian distribution provides the best fit for latitude 75°. Here the average goodness of fit values for the Maxwellian was for SSE $<$ 0.01 and for adjusted R-square $>$ 0.9. Meaning the Maxwellian fit has a low random error component and good explanation of the variation seen in the data at 75°. For latitude 75° there is no apparent Kp pattern. Moreover, the best fit shows a clear MLT dependence as demonstrated in Table 7. For all three detectors, the MLT sectors 9-12 and 18-21, only had 1 to 3 Kp levels where the Maxwellian was the best fit. The MLT dependence might reflect the magnetospheric origin, both in terms of region as well as acceleration source. Focusing on MLT 15-18 or MLT 6-9, the Maxwellian distribution is the best fit across all Kp levels for all three detectors, in contrast to MLT sectors 9-12 and 18-21 This MLT discrepancy was especially prominent with DMSP/SSJ, where the Maxwellian distribution was only the best fit for only Kp$=$ 0 for MLT 9-12 and Kp $=$ 0 and 5 for MLT 18-21.

	DMSP/SSJ			TED 0			TED 30		
MLT	Maxwellian	Power law	Exponential	Maxwellian	Power law	Exponenital	Maxwellian	Power law	Exponential
0-3	NaN	NaN	NaN	100%	0%	0%	67%	0%	33%
3-6	NaN	NaN	NaN	100%	0%	0%	100%	0%	0%
6-9	67%	0%	33%	100%	0%	0%	100%	0%	0%
9-12	17%	33%	50%	33%	17%	50%	33%	17%	50%
12-15	83%	0%	17%	83%	0%	17%	83%	0%	17%
15-18	100%	0%	0%	100%	0%	0%	100%	0%	0%
18-21	33%	17%	50%	67%	17%	17%	50%	17%	33%

Table 7: Maxwellian, Power law and exponential percentage of best fits for each MLT sector for CGM latitude 75°

As mentioned, for 60° CGM latitude, exponential and power law were the most likely to have the best goodness of fit values. For Kp=0,1, the exponential spectral shape is the best fit for all DMSP/SSJ profiles. An exponential spectrum best describe >70% of the TED 0° detector, while the power law is the dominant spectrum for the TED 30° detector. This suggest that the energy spectrum are dependent on the pointing direction of the detectors relative to the magnetic field. There appears to be a slight a trend in which the power law distribution becomes more relevant for DMSP/SSJ and TED 0° detector with increasing Kp. Power law is most often the best fit for Kp = 5 for all three detectors. For 60° CGM latitude, all the distributions often had quite good SSE values, generally below 0.1, meaning all the fits showed low random error component and usefulness for prediction. The adjusted R-square however, was more varied. Nonetheless, it was often above 0.8 for the best fit. At higher Kp levels (Kp= 4,5) for MLT 9-12 and middle Kp levels (Kp = 2,3) for MLT 15-21, none of the best fits had adjusted R-square values above 0.3. Implying that neither of the distributions could fully explain the variations in the flux spectra. At all other MLTs the best fit had adjusted R-square values above 0.7

For 67° latitude, there is a clear MLT variability of the best fit spectra for the two TED detectors. For both TED detectors, the Maxwellian is more often the best fit for nightside MLT sectors than dayside MLT sectors, independent of Kp level. On the nightside, the Maxwellian fits often have SSE below 0.01 and adjusted R-square above 0.7. MLT sectors 6-9, 9-12 and 12-15 sees the least amount of Maxwellian best fits. For the DMSP, there unfortunately isn't enough nightside coverage to draw any conclusion over a nightside-dayside discrepancy. It should, however, be noted that MLT sector 18-21 is the one with most Maxwellian best fits for the DMSP/SSJ. For all three detectors, the exponential is the best fit for most Kp levels in the dayside MLT sectors, almost mirroring the Maxwellian. Meaning MLT sectors 6-9, 9-12 and 12-15 is where the exponential distribution has the largest amount of best fit independent of the Kp level. Here the exponential fits have SSE values below 0.1 and adjusted R-square over 0.8. For power law, it is hard to establish a Kp or MLT trend consistently for all detectors, however there is appears to be a slight increase of its occurrence rate with Kp for DMSP/SSJ. Moreover, for the TED 30° detector it is only the Maxwellian fit that shows any visible Kp trend, becoming more dominant with increasing Kp. For TED 0° the best fit percentages go up and down in a non-systematic way.

Overall, the best fits have consistently better adjusted R-square values for the DMSP/SSJ

spectra compared to the TED detectors for all three latitude bands, especially for 60°. This discrepancy between the two TED detectors and DMSP might be due to the more data points (energy channels) for the DMSP, which gives a more continuous spectrum. For all latitudes, the Maxwellian, power law and exponential distributions all showed low SSE values, 0.1 and under, for all MLT sectors and Kp levels. Meaning the three distributions all showed to be useful for prediction of the various spectra.

4.3 AIMOS vs TED

This section presents a qualitative analysis between the ionisation rates calculated by the AIMOS model in the lower thermosphere and the observed particle fluxes of the high energy channel of TED, Channel 4 (6.503-9.457 keV). Due to the different units, ionisation rate [ion pairs $m^{-3}s^{-1}$] and particle flux [$cm^{-2}s^{-1}sr^{-1}eV^{-1}$], a quantitative comparison can not be made as well. Still, a strong correlation is expected in terms of intensity and occurrence in time and space. Therefore, the analysis highlights differences in terms of intensity distribution and location, as well as response to different levels of Kp-activity.

For the qualitative comparison, maps for the AIMOS simulated ionisation rates have been made. Similar to the flux maps made in section 4.3, the data is sorted according to CGMlat and MLT and averaged over daily Kp for the year of 2010. The resolution is 1°CGMlat x 3MLT. Figure 4.17 displays the $\log_{10}$ Kp averaged ionisation rate calculated by an AIMOS simulation at 112 km altitude, sorted Kp. Based on *Turunen et al.* [2009] electrons with energy 6.503-9.457 keV will have an ionisation peak in the altitude range from 100 to 115 km. The threshold in the maps is $\log_{10}$ (7) [ion pairs $m^{-3}s^{-1}$], and is chosen in respect to the medians in every MLT sector for every Kp, analogue to the noise level threshold in the POES/TED maps.

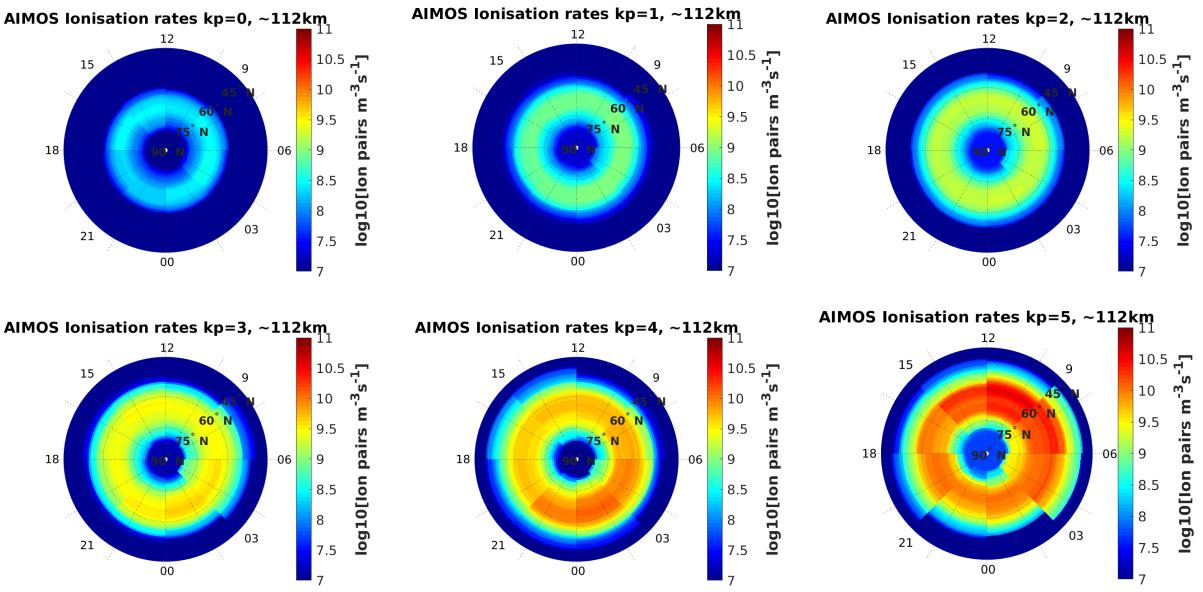

Figure 4.17: AIMOS log_{10} ionisation rates maps [ion pairs $m^{-3}s^{-1}$] 112 km altitude. 1°CGMlat x 3MLT. Top row, from left to right: Kp = 0, 1 and 2. Bottom row, from left to right: Kp = 3, 4 and 5

Figure 4.17 illustrates how the ionisation rate increase significantly with Kp. The ionisation rates starts around 8-8.5 for Kp = 0 to up to 10-11 for Kp = 5 inside the auroral oval. Similarly, the TED fluxes in Figure 4.3 and 4.4 vary over the 5.5-8 from Kp 0 to 5. The response to increased geomagnetic activity is not just in the form of increased intensity of the auroral oval, but also in latitudinal extent. The width of the auroral oval increases both polewards and equatorwards with Kp, increasing from between 60° and 75° latitude for Kp = 0 and 1 to between 50° and 80°. For Kp=5 the oval is widest in the morning sector from 3-9 MLT covering CGM latitudes from ∼80° down to 45°.

There appear to be a distinct in the MLT variability in AIMOS as function of Kp. For Kp = 0 the ionisation rate across most MLT sectors are at around 8.5, with the exception around 18-00 MLT where the enhanced ionisation rate band is below 8.5. For Kp = 1 and 2, the auroral oval includes a continuous level of ionisation rates across all MLT channels, with the log_{10} ionisation rates being about 9 in the centre and 8.5 at the auroral oval boundaries. For Kp = 3 and especially for Kp = 4, there is stronger intensity in the midnight to morning sectors (21-06 MLT). Here the log_{10} ionisation rate is up to 10, while for the other MLT sectors it is ∼9.5. For Kp = 5, however, the MLT sectors with the strongest band falls between the morning and afternoon sectors, from 6-9 MLT to 12-15 MLT. In these MLT sectors the log_{10} ionisation rates are around 10.5-11+, while being between 9.5 and 10 for the other MLT sectors. In other words the MLT sectors with strongest level of ionisation switch between the various Kp levels. This contrasts what was seen from TED and DMSP/SSJ in section 4.2, see Figure 4.10, where the increase in flux was consistently higher for specific MLT sectors (18-21 for an example) than other

compared to other sectors.

As the AIMOS ionisation rates and the TED electron fluxes are given in different units, maps with relative change from the median has been made for easier qualitative comparison. The data has been subtracted and normalised by the median in each MLT sector. Here the latitudinal variance of AIMOS and TED can be studied and compared. Figures 4.18 and 4.19 shows the relative change for AIMOS and TED from the respective medians in each MLT sector for Kp = 0 to Kp = 5.

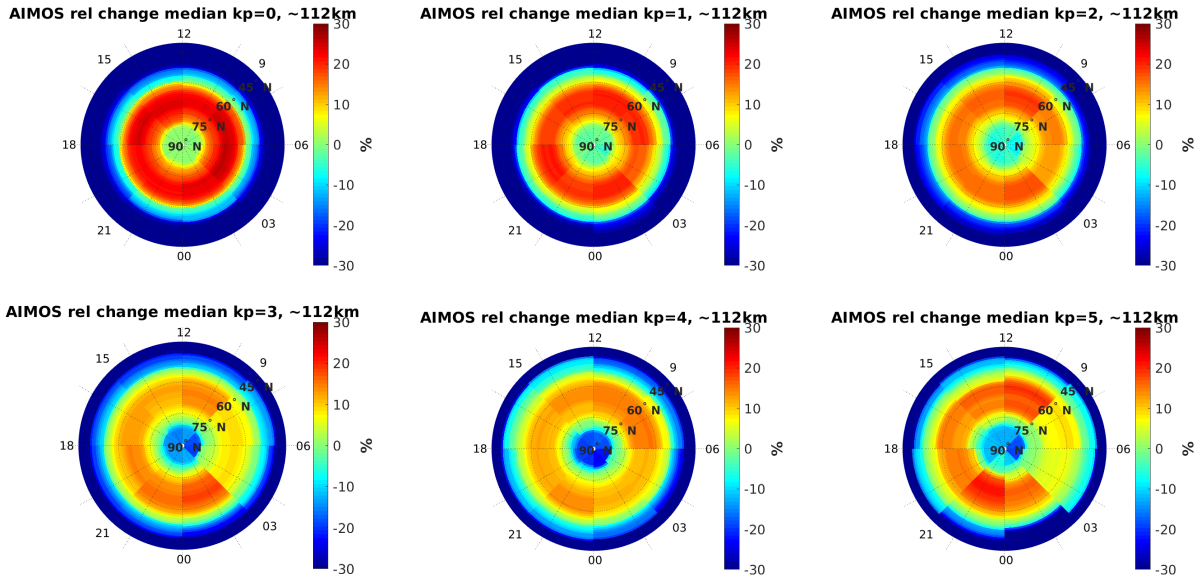

Figure 4.18: AIMOS relative change from median in each MLT sector ((AIMOS-median(AIMOS))/median(AIMOS))). Top row, from left to right: Kp = 0, 1 and 2. Bottom row, from left to right: Kp = 3, 4 and 5

First noticeable discrepancy between the maps in Figures 4.18 and 4.19, is in the borders between the values around the median (around 0% relative change) and the ring of higher relative change. For TED, especially at low Kp, the latitude bands below 60° and above ° 75-80° are all around the median. The relative change is around 0%. For latitude bands between 60° and 75°, the relative change ranges from between 20% to above 30%. For AIMOS, however, the relative change at lower latitude is below -30%, or technically -100% since the ionisation rate here is often 0. The area covering latitudes with values higher than the median is significantly larger for AIMOS than TED.

The gradient for values relative to the mean is significantly steeper for AIMOS than TED at the equatorwards border of the oval. At the poleward border of the auroral oval, the gradient in AIMOS and TED are similar for all Kp levels, except Kp = 4. Meaning AIMOS sees significantly more ionisation near the magnetic pole than lower latitudes, despite TED detecting similar levels of flux near the pole and for lower latitudes. In fact, for the for latitudes below 45° the ionisation rate for AIMOS is often zero even though TED detects

$\log_{10}$ flux levels around 4-5 at these latitudes.

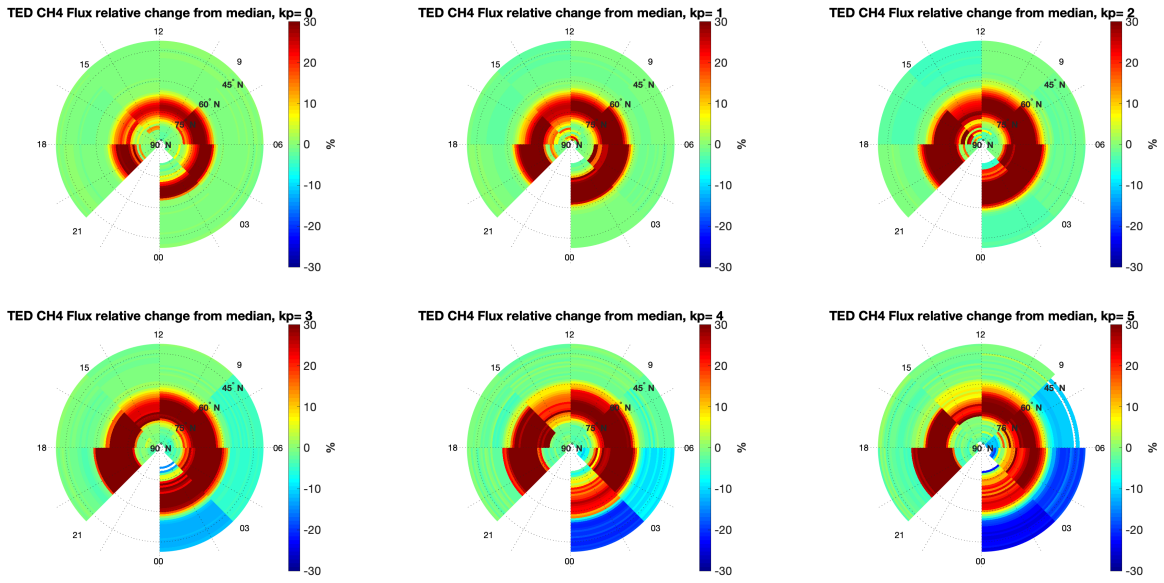

Figure 4.19: TED Channel 4 (6.503-9.457 keV) relative change from median in each MLT sector ((TED-median(TED))/median(TED))). Top row, from left to right: Kp = 0, 1 and 2. Bottom row, from left to right: Kp = 3, 4 and 5

4.4 AIMOS vs WACCM

In this section the aim is to compare the daily ionisation rates applied as default in the frequently used chemistry climate model WACCM with the ionisation rates calculated by AIMOS. The ionisation rate data is sorted by geographic longitude, latitude, and altitude (pressure level), and is averaged for each daily Kp level in the year 2010, see Figure 4.1. The averages are plotted onto ionisation rates maps (latitude vs longitude) for chosen altitudes. The aim is to compare and evaluate any systematic difference in ionisation rate level, latitudinal coverage, and behaviour between the two models. The coordinates are in geographic form and the resolution is 0.9° latitude and 1.25° longitude.

Figure 4.20 shows Kp averaged $\log_{10}$ ionisation rates [ion pairs $m^{-3}s^{-1}$] for AIMOS simulation for altitude ∼112 km, for Kp = 1 to 5, for the year 2010. (It is the same ionisation rate data shown in Figure 4.17 now displayed in a geographic grid). The maps have a noise threshold of $\log_{10}$ 7 [ion pairs $m^{-3}s^{-1}$] chosen in respect to the average and median values of each longitudinal band for both AIMOS and WACCM. The longitudinal coordinates in the maps goes from east to west, which means 90° = 90° east and 270° = 90° west.

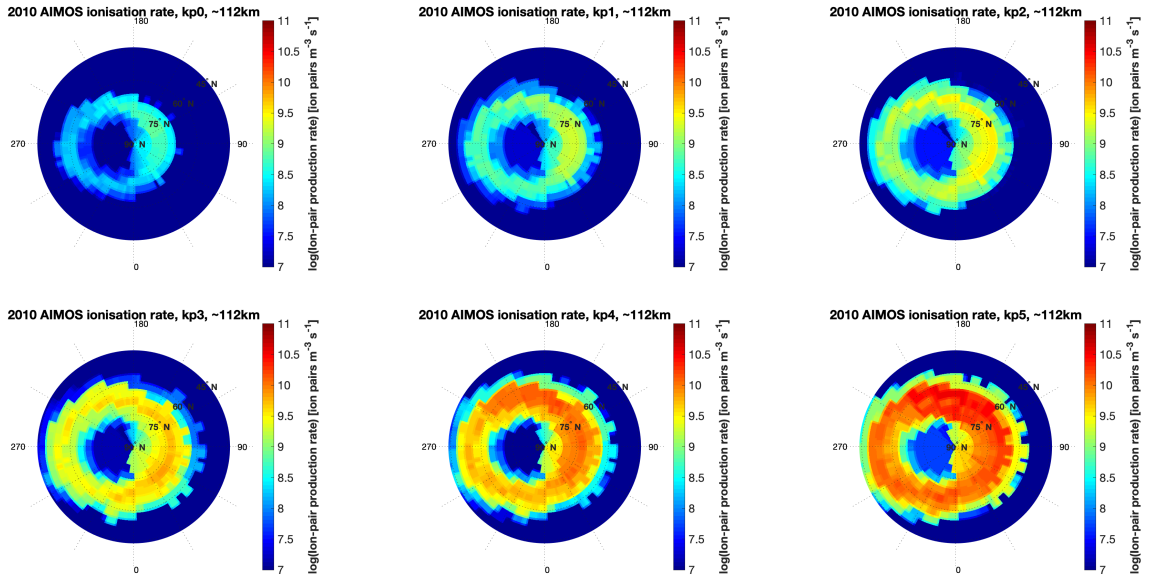

Figure 4.20: AIMOS $\log_{10}$ ionisation rates maps [ion pairs $m^{-3}s^{-1}$] 112 km. 0.9 geographic latitude 1.25 longitude. Top row, from left to right: Kp = 0-2. Bottom row, from left to right: Kp = 3-5

For all Kp levels, Figure 4.20 shows a general equatorward shift in west (270° longitude) for the auroral oval, consistent with the offset of the geomagnetic pole. Here the latitudinal bands with highest ionisation rates are found between 50-70° latitude. In the east, however, the latitudinal bands with highest ionisation rates are found between 60-80° latitude. For all Kp levels the eastern sector (0-180°) has on average higher ionisation rate levels than the western sector (180-0). For the areas around 0° and 180° longitude, however, there is a discrepancy in the ionisation rate levels. Around 180° longitude the ionisation rate is consistently higher for all Kp levels than for around 0°. For Kp = 0, the rate is between 8.5-9 around 180° longitude and ∼8 around 0°.

AIMOS experiences a noticeable change in both max level of ionisation and latitudinal width of the auroral oval with increasing Kp. For Kp = 0, the max $\log_{10}$ ionisation rates is ∼9, while for Kp = 5 it increases to over 11. For increasing Kp the longitudinal maximum of the ionisation rates are found between 135° and 225 °E. Here the ionisation rate is consistently around 10.6 or higher for Kp = 5. The auroral oval expands with Kp both equatorwards and polewards for all longitudinal bands. On the western side it expands towards 45° and to 70°N latitude. In the eastern sector (0-180°E longitude), AIMOS' auroral oval expands from 70°-80° to 60°-80+°.

As shown in Figure 4.17 AIMOS sometimes calculates elevated flux levels within the polar cap, linked to open field lines. In Figure 4.20 for latitudes above 85°N, inside the arctic circle. Electron ionisation rate levels in the lower thermosphere within the polar cap are both unexpected and inexplicable, and might be related to the model itself, since it does not match with the flux levels observed by the TED shown in Figure 4.3.

Figure 4.21 shows the daily Kp averaged $\log_{10}$ ionisation rates [ion pairs $m^{-3}s^{-1}$] for WACCM simulation for altitude $\sim$ 112 km, for Kp = 1 to 5, for the year 2010. The grid and threshold is same as for AIMOS, with the threshold at $\log_{10}(7)$[ion pairs $m^{-3}s^{-1}$].

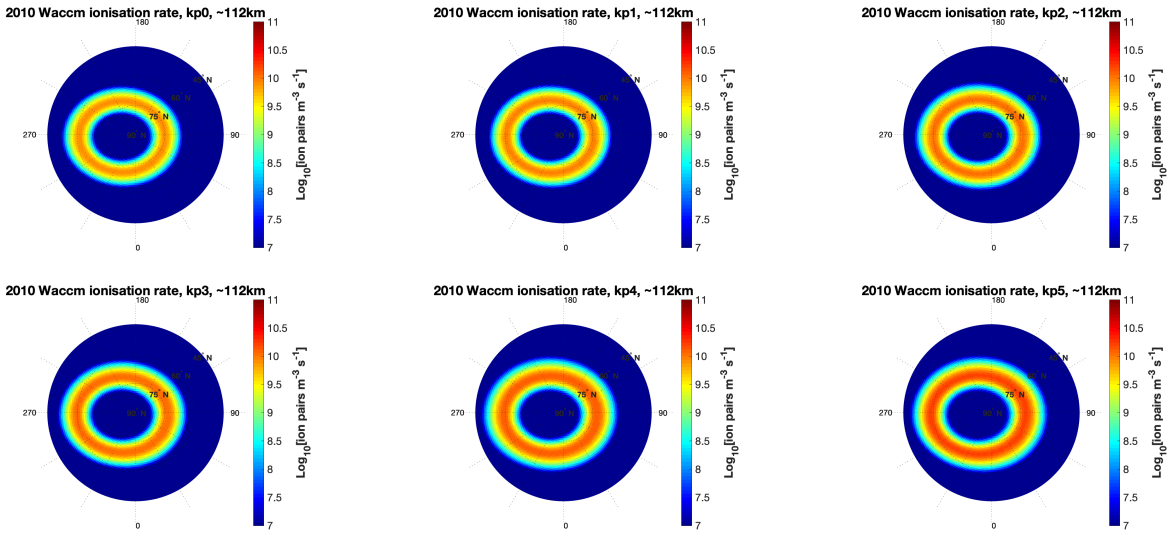

Figure 4.21: WACCCM $\log_{10}$ ionisation rates [ion pairs $m^{-3}s^{-1}$] maps 112 km. 0.9 geographic latitude 1.25 longitude. Top row, from left to right: Kp = 0-2. Bottorm row, from left to right: Kp = 3-5

Similarly to AIMOS, WACCM also sees a noticeable equatorward shift for the auroral oval towards 270°E longitude. Meaning again the auroral oval is found at lower latitudes between 180-360° E than between 0-180° E. For the western sector the auroral oval covers the latitude band between 55-65°N, while for the eastern sector the auroral oval latitude band falls between 70-80°N. The auroral oval implemented in WACCM displays a continuous level of ionisation rate for all longitudes, meaning WACCM includes no variance with longitude/MLT.

As expected, the ionisation rate increases with Kp as well as the latitudinal size of the auroral oval. However, both the widening of the auroral oval and intensity increases only moderately with each Kp level compared to e.g. the AIMOS model in Figure 4.20. For Kp = 0, the max ionisation rate is ~9.5, while for Kp = 5 it has only increased to ~10.5, increasing only one order of magnitude. As pointed out above, AIMOS increased approximately two orders of magnitude over the same Kp-levels. The widening only increases with a 2-3 ° polewards and equatorwards. The relative weak response to increased Kp hints towards either an overestimated level of ionisation rates during quiet periods of geomagnetic activity, or an underestimation during active time or both by the WACCM simulation.

In Figures 4.20 and 4.21 there is a clear contrast in the auroral oval for lower Kps (Kp=0,1) between the models. WACCM includes considerably higher ionisation rates for low levels

of geomagnetic activity, and therefore estimates a more pronounced oval than AIMOS. For Kp = 0, AIMOS's ring of higher ionisation rate, between 70-80° latitude in the eastern side and 60° latitude in the western side, has $\log_{10}$ ionisation rates around 8-8.5. For WACCM there is a continuous band of $\log_{10}$ ionisation rates of ∼9.5 from 75° N latitude in the east to 60°N in the west.

Figure 4.22 shows the Kp averaged ionisation rates for both AIMOS (top row) and WACCM (bottom row) for Kp = 0,3 and 5 for altitude 95 km. Here, the main ionisation rates are caused by electrons in the energy range 10-20 keV as shown in Figure 2.18 by *Turunen et al.* [2009]. Important to note, the noise threshold is now at $log_{10}6$ [ion pairs $m^{-3}s^{-1}$], due to the lower rates of ionisation close to the mesopause than at ∼112 km altitude.

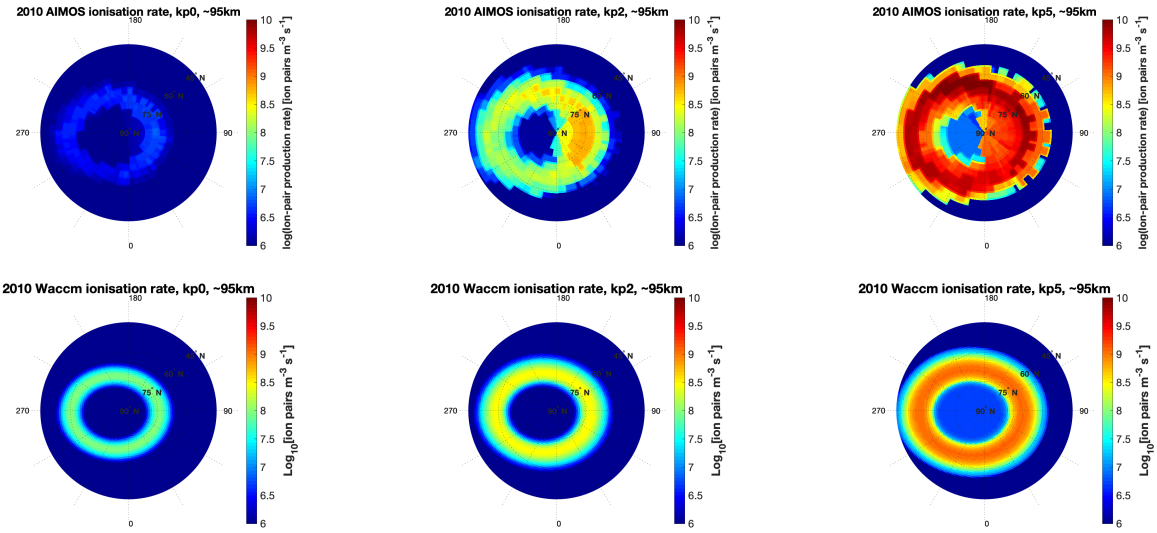

Figure 4.22: Top row: AIMOS ionisation rates at altitude around 95 km. left-right Kp=0,2,5. Bottom row: WACCM ionisation rates altitude around 95 km. Left-right Kp=0,2,5

At 95 km the difference between AIMOS and WACCM for low Kp is even more pronounced than at 112 km . For Kp=0 for AIMOS (top left) the oval is barely visible with ionisation rates close to the threshold of $\sim log_{10}6$. For WACCM, however, (bottom left) there is a clear and visible oval, with ionisation rates $\sim log_{10}$ 7.5. This shows that in WACCM estimates considerable higher ionisation rates for days of low geomagnetic activity compared to AIMOS. This is evident both at ∼112 km altitude and close to the mesopause at ∼95 km altitude. For Kp = 2 there seems to be a better agreement between the two models at ∼95 km altitude. This is not the case for ∼112 km, where WACCM shows a general stronger intensity oval than AIMOS until the Kp level exceeds 3. This might be due to WACCM overestimating ionisation for lower geomagnetic activity, and/or a shift in the ionisation rate peak. For Kp=5 the difference between AIMOS and WACCM at ∼95km is striking. The size and intensity of the oval is both wider and stronger in AIMOS compared to WACCM.

To further explore the ionisation response to increased geomagnetic activity for AIMOS and WACCM, relative difference maps for both ∼112 km and ∼95 km have been produced. Figures 4.23 and 4.24 shows the relative difference between AIMOS and WACCM for Kp = 1 to 5 for altitudes ∼112 and ∼95 km. Red indicates ionisation rates (IR) $IR_{AIMOS} > IR_{WACCM}$, while blue indicates $IR_{AIMOS} < IR_{WACCM}$.

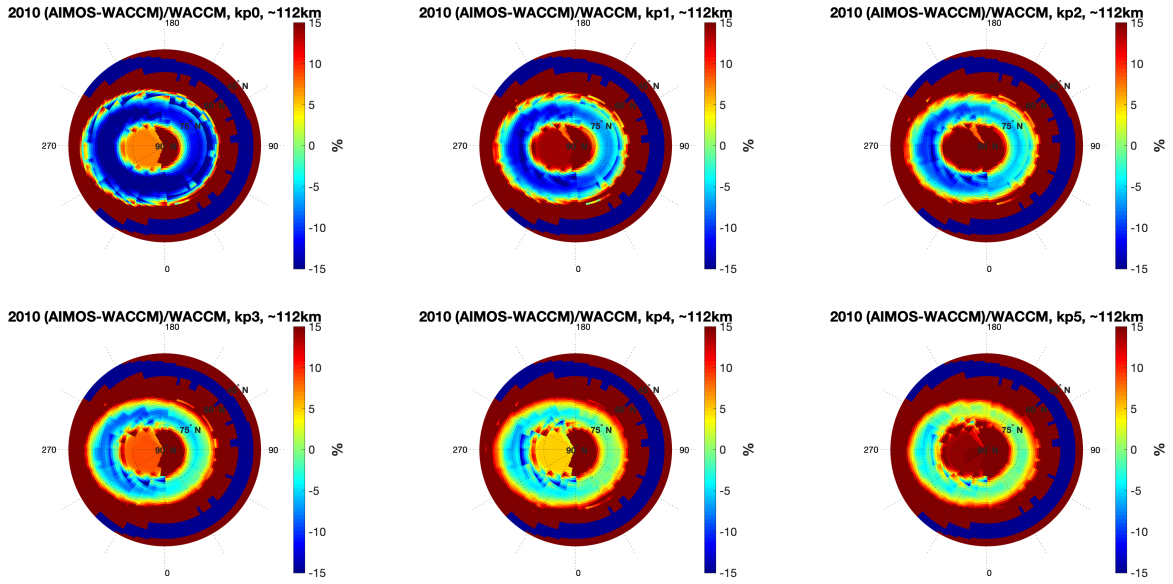

Figure 4.23: Relative difference between AIMOS and WACCM for Kp = 1 to 5 for altitude ∼112 km, (AIMOS-WACCM)/WACCM. Top row, from left to right: Kp = 0-2. Bottorm row, from left to right: Kp = 3-5

In both Figure 4.23 and 4.24 there is a two coloured pattern for the low Kp-levels. The region corresponding to the area covered by the WACCM ionisation rates are blue, while the polar cap and the equatorward edge is dark red. For Kp = 0, the difference inside WACCM's oval of enhanced ionisation (WACCM's auroral oval) rate (between 65-80 °N latitude) is ≥-15% at ∼95 km and ∼112 km altitude . This difference are more consistent with longitude at 95 km. This implies that inside the WACCM auroral oval, WACCM includes significantly higher ionisation rate than AIMOS for Kp = 0 throughout the lower thermosphere.

For Kp = 5, the relative differences significantly increases inside the WACCM aurora oval and display a different behaviour for the two altitudes. At ∼112 km altitude, the relative difference inside the WACCM auroral oval is around -2% to 5%. This implies that the ionisation rates estimate more similar levels for high Kp-levels compared to low Kp-levels at this altitude. This also further confirms a higher sensitivity in the AIMOS ionisation rate response to increased geomagnetic activity compared to the estimate included in WACCM. Still, the relative difference at ∼95 km altitude is still significantly higher compared to ∼ 112 km. Inside the oval, the relative difference is continuously between 5% and 15% for high activity. In Figures 4.20 and 4.22, inside the area covered by the WACCM auroral

oval, the relative difference significantly decreases as the AIMOS ionisation rates increases more with geomagnetic activity compared to the WACCM ionisation rates.

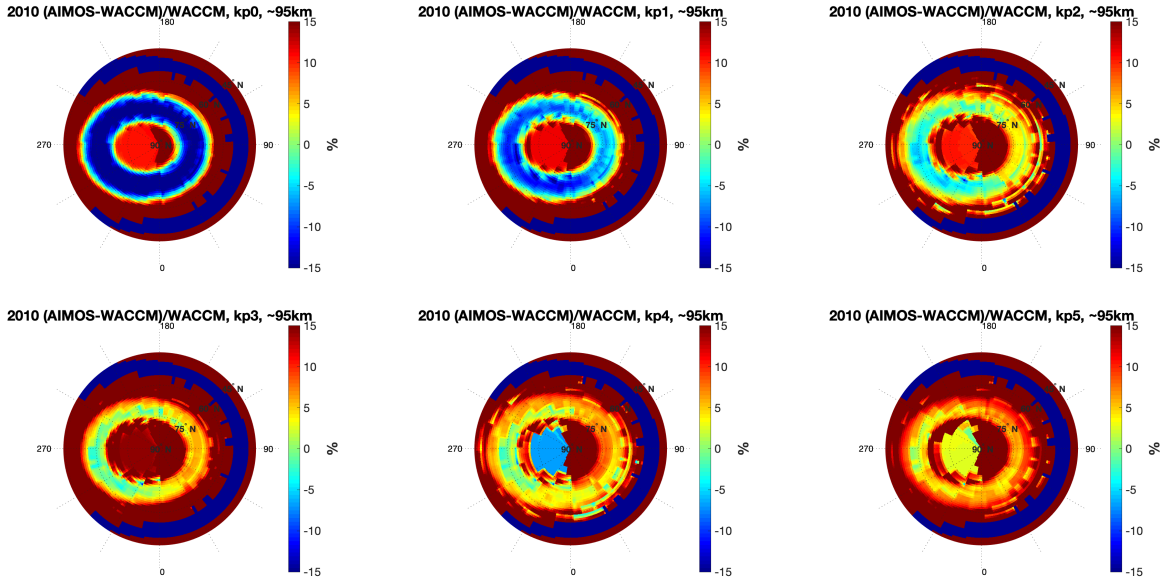

Figure 4.24: Relative difference between AIMOS and WACCM for Kp = 1 to 5 for altitude ∼95 km, (AIMOS-WACCM)/WACCM. Top row, from left to right: Kp = 0-2. Bottom row, from left to right: Kp = 3-5

In Figures 4.23 and 4.24 there is a visible latitudinal difference between the two models. Within the polar cap and in particular the equatorward edge, AIMOS is >15% for both altitudes all Kp values. For Kp < 4 this area however fall outside the WACCM auroral oval. For Kp = 4 and 5, AIMOS' latitudinal area of higher ionisation rate goes from the pole to 60°N in the east and 65°N to ∼45°N in the west. For WACCM, however, there is only a moderate increase of the latitudinal coverage with Kp. Most of the response comes from strengthening of the continuous ring of enhanced ionisation around 75°N in the eastern sector and 60°N in the western sector.

In the arctic circle, above 80° latitude, AIMOS consistently calculates significantly higher ionisation rates than WACCM. This particularly true for the eastern side, where the relative difference is above 15% for all Kp and altitudes. As discussed, the high level of ionisation rate in AIMOS in this area is unexpected given that the electrons are guided in at lower latitudes (∼75°).

Figures 4.23 and 4.24 display a difference in the models for longitudinal continuity. For AIMOS the eastern sector (0-180° longitude) is consistently higher for all Kp levels, as seen in Figures 4.20, 4.22. For Kp = 1 and altitude ∼95 km, for an example, the relative difference inside the auroral oval towards 90° E longitude falls between 0-5%, while towards 270° E it falls between -5% and 0%. The eastern-western discrepancy is caused by the longitudinal variance for AIMOS inside the auroral oval. For WACCM the aurora oval

has continuous level of ionisation from east to west for all Kp levels and both altitudes. Meaning inside their respective auroral ovals, AIMOS experiences a longitudinal variance for the ionisation rate, while for WACCM the rate is consistent, depending only on latitude and Kp level instead.

5 Discussion

The overarching research question of this thesis is: How does the auroral electron fluxes depend on geomagnetic activity? Or more specifically: How does the *observed* auroral electron fluxes vary in terms of geomagnetic activity? In other words, our results depend on the timing, location, and quality of the observations themselves. Based on the results presented in Chapter 4 there appear to be a systematic higher flux level detected by the DMSP/SSJ particle detectors compared to the POES/TED particle detectors. In the following sections we will discuss to which degree this discrepancy might be explained in terms of different spacecraft charging, different longitudinal sampling, and/or the detectors' pointing directions relative to the local magnetic field. Moreover, we will assess the differences found in terms of the electron spectra, and how their shape and occurrence rates fits previous studies. Ultimately, both the pitch angle distribution and the energy spectra can provide information on the magnetospheric origin and associated processes. Finally, as our overall motivation is to understand the energy input and its consequences for the atmosphere, the difference between the ionisation rate estimates implemented in WACCM will be further discussed in the context of previous research.

5.1 Spacecraft charging

Satellites passes through different regions of plasma. The charged energetic particles has the potential to cause issues for both the satellites and instruments onboard. One of these challenges is a phenomena called spacecraft charging. In this subsection a brief and short description of what spacecraft charging is alongside potential consequences for the electron flux observations will be given. In particular, literature around spacecraft charging specific for DMSP/SSJ and POES/TED are presented and evaluated in respect to the 2010 flux observations.

A spacecraft interacts with the environment and plasma around it. In consequence, the spacecraft can accumulate excess amount of electrons or ions [*Lai*, 2011]. The excess amount of charged particles causes a net voltage charge on the spacecraft, which generates an electric field in accordance with Gauss' law [*Griffiths*, 2017]. The electric field generated by the charge will then "attract" more particles of opposite charge of the spacecraft from the neutral space plasma surrounding it, in an effort to neutralise the generated electric field [*Lai*, 2011]. As the ambient electrons have significantly lower mass than the ambient ions, the electrons are more easily accelerated and will gain a higher velocity compared to the protons. Therefore, the spacecraft will receive a higher ambient electron flux than that of the ions. In consequence, the spacecraft are more likely to gain a negative voltage than positive voltage [*Lai*, 2011]. The resulting electric field will then attract ions towards the spacecraft to neutralise the charge. A negatively charged spacecraft could then experience an increase of proton flux and potentially a decrease in electron flux until the charge is neutralised. If spacecraft charging events for DMSP / POES appears to happen relatively often or over long time periods, it could potentially affect the measurements and depress the electron flux detected by the SSJs and/or TED.

The likelihood of spacecraft charging increases with increasing geomagnetic activity. As such it is related to the Kp-level. However, due to how localised a spacecraft charging event is, both in respect to duration and location [*Lai*, 2011], the Kp-index is not a reliable predictor of charging events. Figure 5.1 illustrates how spacecraft charging can occur.

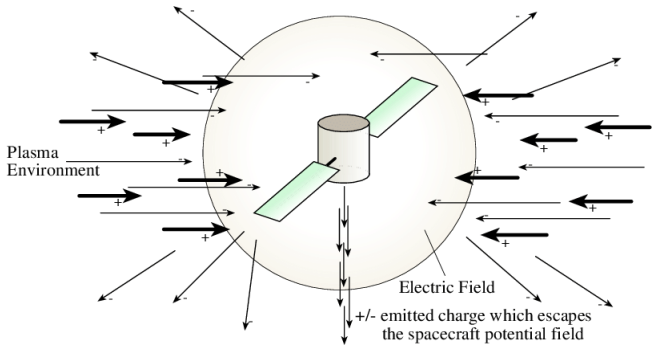

Figure 5.1: Simple illustration of how spacecraft flying through plasma can be experience spacecraft charging, from [Jones and Schaub, 2013]

The effects of spacecraft charging can generally be categorised into two types [*Lai*, 2011]:

(1) Damage to on-board electronics

→ Harmful to health of on-board electronics, and in severe cases affect operations, navigational systems, controls and terminate the mission of the spacecraft

(2) Interference with scientific measurements

→ Can affect on-board measurements of space plasma properties. The charged spacecraft can cause a plasma sheath to form around the spacecraft with a higher density of opposite charged particles.

Several studies have targeted spacecraft charging events and their characteristics for low Earth orbit (LEO) satellites such as DMSP and POES, e.g [*Gussenhoven et al.*, 1985; *Anderson*, 2012; *Anderson and Koons*, 1996; *Frooninckx and Sojka*, 1992; *Colson and Minow*, 2011; *Redmon et al.*, 2017b]. *Gussenhoven et al.* [1985] was the first to show that the DMSP spacecrafts could experience significant voltage charging, under -100 V. This occurred when the energetic electron fluxes was very large, while the thermal density was very low. The study postulated two requirements necessary for a charging event: (1) Current density above $\sim 10^{-1} nAcm^{-2}$ and (2) The integral number flux for electrons with energies over 14 keV exceed $10^{8} cm^{-2} s^{-1} sr^{-1}$. These requirements have been adopted as the standard for characterising charging events [*Anderson*, 2012; *Colson and Minow*, 2011]. In *Anderson* [2012] a 11-year study of spacecraft charging events in LEO is presented. Using the requirements from *Gussenhoven et al.* [1985], they found ∼1600 significant charging events (<-100V) over the 11-year old period for DMSP spacecrafts [*Anderson*, 2012].

In this master thesis, auroral forcing estimates are studied for the year of 2010. *Anderson* [2012] found that spacecraft charging events happens more frequently towards solar minimum.

2010 is two years after the solar minimum in 2008, which implies there could be a higher frequency of charging events in 2010 compared to average. *Anderson* [2012] further finds that spacecraft charging events predominately occurs between 65-75° CGMlat during 18-02 MLT. This hot spot co-inside with our area of latitudinal interest, but falls, however, partly outside of the MLT zone covered by DMSP as shown in Figure 3.3.

In section 4.2.3 a comparison is made between MLT sector 18-21 for latitudes 65-75° for TED and SSJs. The findings from *Anderson* [2012] implies that spacecraft charging could've potentially affected the observed fluxes from both detectors and potentially help explain some of the discrepancies observed. However, *Anderson* [2012] finds that the average event only last eight seconds, with the maximum duration of two minutes. *Colson and Minow* [2011] looks at charging events for DMSP spacecrafts F16, F17 and F18 for the month of June in 2011. In the study they find 17 events for F16, six events for F17 and seven events for F18 [*Colson and Minow*, 2011], with the average duration being between 14-21 seconds long. The longest event lasted 71 seconds [*Colson and Minow*, 2011]. In summary, the studies did not reveal any truly long lasting events. In this thesis the flux observations are averaged based on the daily Kp level. This implies that the spacecraft charging needs to be both significantly high and long lasting to have a noticeable effect on the average flux levels. Neither *Colson and Minow* [2011] nor *Anderson* [2012] found that to be the case. Moreover, to our knowledge, no study mentions eventual issues regarding electron flux measurements. We therefore assume that spacecraft charging likely doesn't have any measurable effect on our estimates. However, due to the fewer days with Kp levels=5 (3 days) and 4 (5 days), spacecraft charging could potentially have some effect on the measured flux inside the auroral oval, between MLT 18-02. Still, due to how localised spacecraft charging events are, this would only affect specific MLT times and latitude bands. Since the estimates have a broad MLT resolution (3 MLT), any effect from spacecraft charging are likely to be minimal.

5.2 Bias in the geomagnetic field

The POES and DMSP spacecrafts (and MetOp) are Sun-synchronous orbiting polar satellites. Sun-synchronous means the satellites will pass over any given point on Earth's surface at the same mean solar time, which implies also a limited MLT zone. Inside an MLT sector, however, the different satellites might have different coverage of the same geographical areas of the Earth. Due to the dipole geomagnetic field longitudinal variance in the northern hemisphere [*Zawedde et al.*, 2016; *Barth et al.*, 2001], this could potentially affect our observed flux levels. This subsection, targets the geographic sampling distributions from DMSP and POES for MLT 6-9. Differences in the majority sampling regions are discussed in respect to a potential effect on the averaged flux data. MLT 6-9 is chosen due to good overlapping coverage here between the spacecrafts, see section 4.2 and Figures 4.2 and 4.6.

Figures 5.3 and 5.4 shows the geographic sampling distribution for DMSP/SSJ 9.45 keV and TED 0° Channel 4 on a 1°latitude-15°longitude geographic grid. The longitudinal coordinates are given in respect to east (90° longitude = 90° E, 270° = 90° W). The samples are the ratio between the number of hits in 1° latitude - 15° longitude sector and

the sum of hits for an latitudinal band over all longitudinal sectors.

Figure 5.3 illustrates how the main sampling regions vary with latitude for DMSP/SSJ for Channel 9.45 keV. Near the poles, 75-83° N latitude, the highest sampling area is between 335° and 90° E longitude, >10%, for all Kp levels. For latitudes between 60° and 75° N, the maximum sampling zones are located between 270°-15° East longitude and 75-90° East longitude, with sampling rates ∼5-6% and above. Below 60° N to 45° N latitude, the highest samplings rates are found over the western sector. Below 45°, towards the equator, DMSP/SSJ samples only from the eastern sector (15-165° E longitude). Meaning here the sampling rate is 100%. This is most likely an artefact of the orbit of the satellite

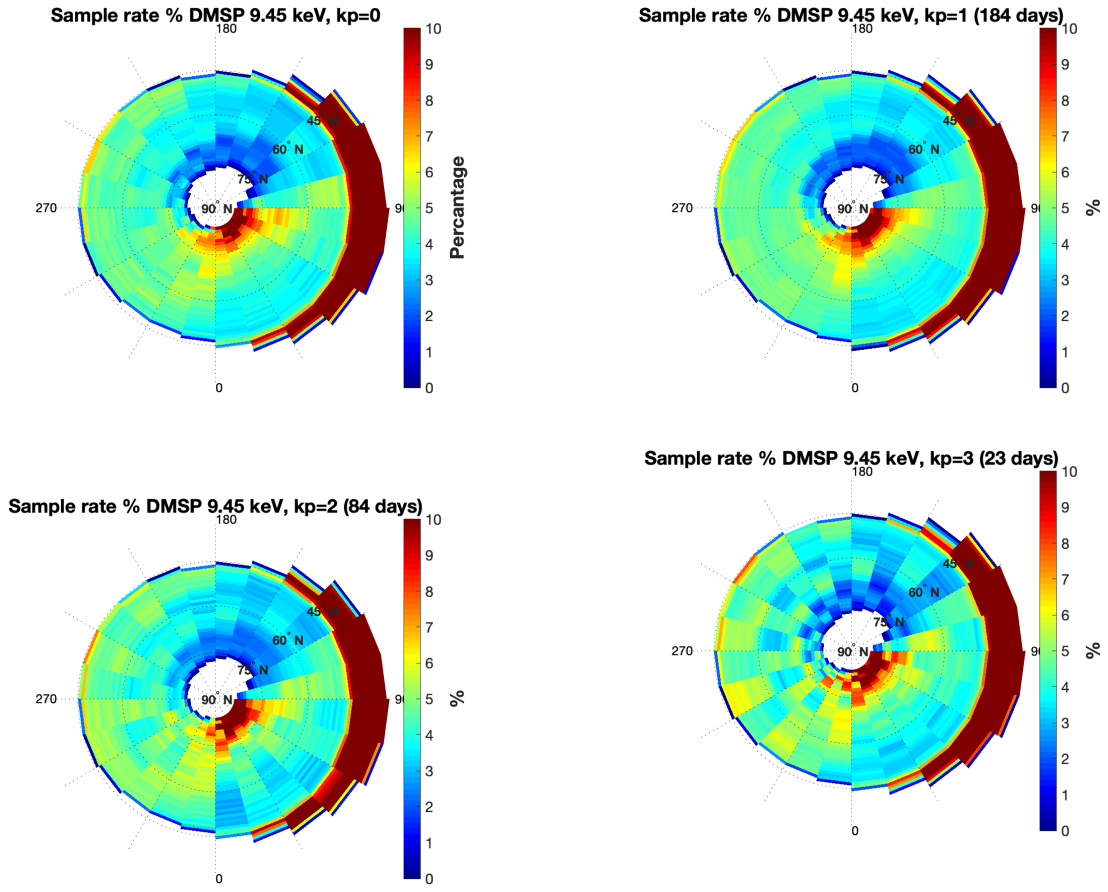

(a) Figure continues on the next page

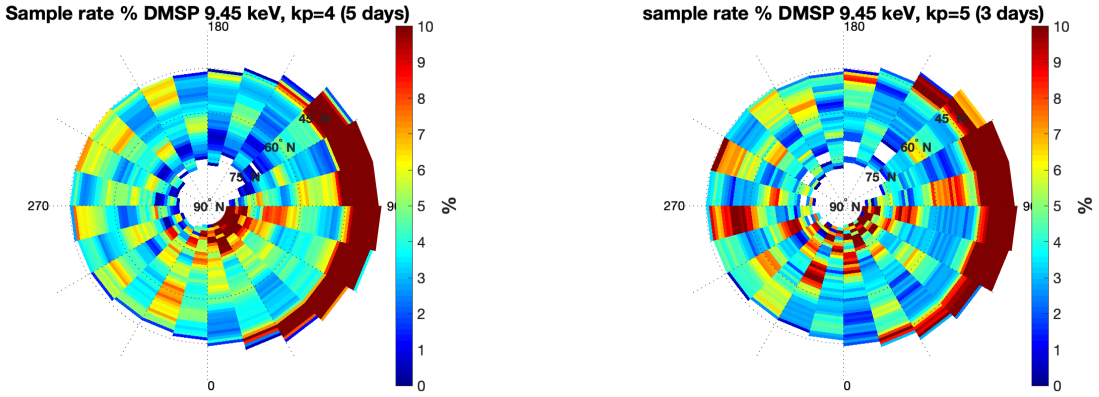

Figure 5.3: Geographic sampling rate for DMSP/SSJ 9.45 keV on a 1° latitude - 15° longitude grid, for daily Kp=0-5, for MLT sector 6-9 in the year 2010. sampling rate is given by the ratio between hits for one latitude-longitude sector and sum of hits over the entire latitude band.

The sampling rate pattern holds for all Kp levels for DMSP/SSJ, however, it becomes more "messy" or "choppy", where some sectors observes significant increase in sampling rate with Kp. For Kp=5, the western sector under 60° sees considerably higher sampling rate than for Kp=0,1,2,3. This is most likely due to the fewer days for Kp=5 (3 days), resulting in poor coverage and fewer data points, see Figure 4.1.

Figure 5.4 shows the samplings rate for POES/TED 0° Channel 4 analogue to Figure 5.3. For POES/TED the sampling rates are consistently highest in the longitudinal sector 90° and 180° East, for Kp=0-3, . The highest sampling rates are at around ∼6%, compared to 3-4% for the other regions. The pattern holds for Kp=0 to 3, becoming more pronounced with less days for the Kp levels. The pattern is also visible for Kp=4, however, somewhat more "choppy" due to a poorer coverage (5 days). The pattern switches side of the 180° meridian for Kp=5, where the longitudinal region between 180° and 270° experiences the highest samplings rate. Note, that the fewer days for higher Kp means there is less coverage for all latitudes and longitudes, and the contribution to the total sampling is more localised.

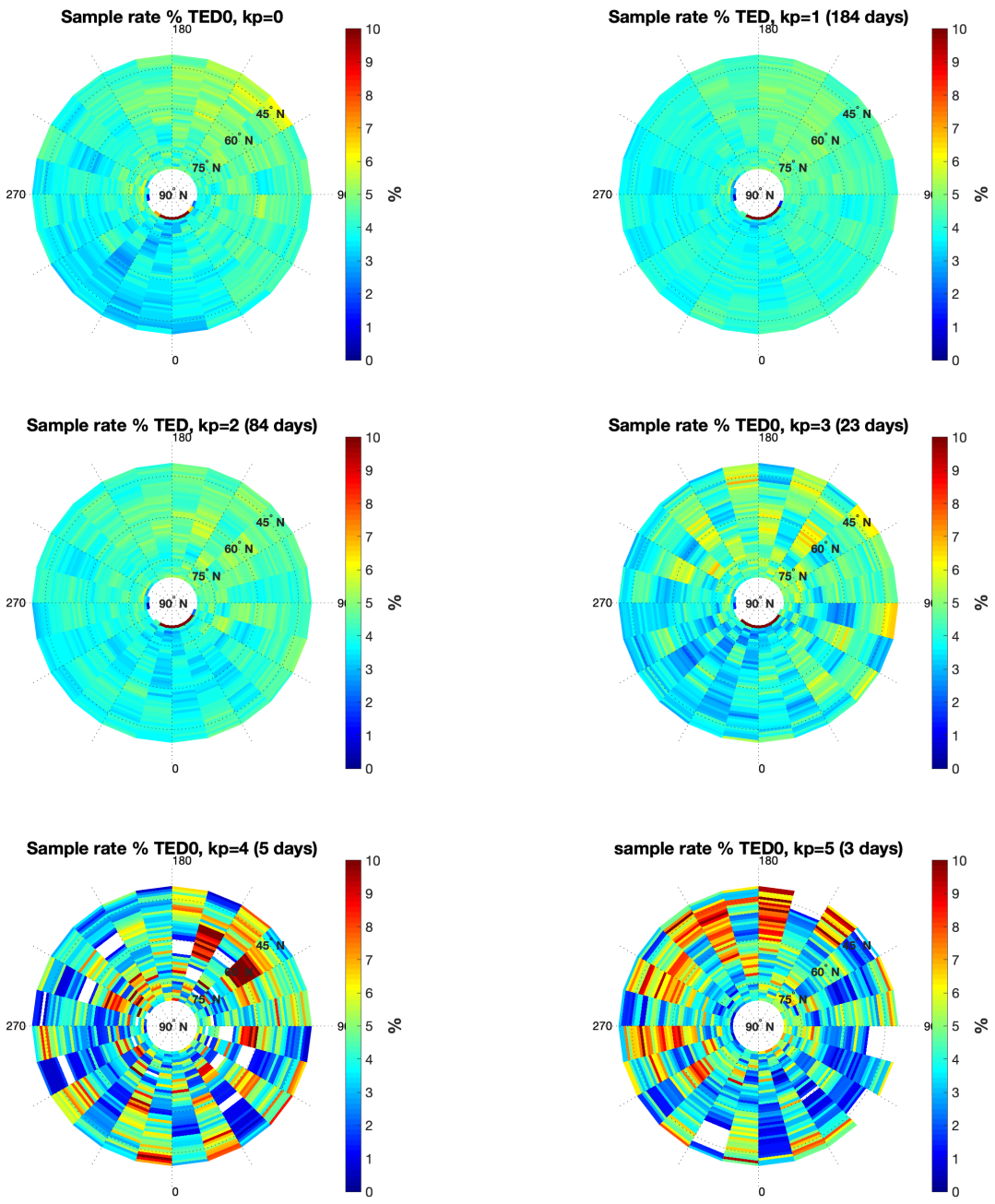

Figure 5.4: Geographic sampling rate for TED 0° Channel 4 on a 1° latitude - 15° longitude grid, for daily Kp=0-5, for MLT sector 6-9 in the year 2010. sampling rate is given by the ratio between hits for one latitude-longitude sector and sum of hits over the entire latitude band.

The effect of geographic auroral precipitation has been examined in multiple studies. *Barth et al.* [2001] investigated the geomagnetic longitude dependence observed in NO_x produced by auroral electron at 106 km altitude. They found a minimum region above Scandinavia and Greenland which could be explained as a consequence of the asymmetries of the

Earth's magnetic field. Electrons bouncing around the Earth along the weak magnetic field associated with the South Atlantic anomaly region are lost to the atmosphere, as they have to travel further down to reach the magnetic mirror point [*Barth et al.*, 2001; *Zawedde et al.*, 2016; *Baumjohann and Treumann*, 1996]. The parallel velocity of the charged particle's moving along the magnetic field is given by:

$$v_{||} = v\sqrt{1 - \frac{B}{B_m}} \tag{16}$$

B is the strength of the magnetic field, v is the velocity of the particle and B_m is the value of the magnetic field where the angle between the magnetic field and velocity vector, the pitch angle, is 90° and the particle has no velocity along the field [*Baumjohann and Treumann*, 1996]. The weaker field corresponding to e.g. the South Atlantic anomaly implies that the mirror point will be located lower in the atmosphere, where the particles are more easily lost through collisions [*Baumjohann and Treumann*, 1996]. Hence, the bouncing electrons will be depleted passing over anomaly region [*Zawedde et al.*, 2016]. *Barth et al.* [2001] implies that this will affect the precipitating fluxes in the Northern hemisphere. They suggests that we are seeing "normal" levels of electron precipitation west of the region linked to the South Atlantic anomaly, while a much weakened precipitation will be observed inside the weak magnetic field region and east of it. *Zawedde et al.* [2016] studied this theory for both NO and OH production. They plotted the square root ratio between the magnetic field in the north and the south, Figure 5.5. The theory then states that there will be more precipitation in the regions where $B_{south} > B_{north}$ and weaker levels of precipitation $B_{south} < B_{north}$ [*Zawedde et al.*, 2016].

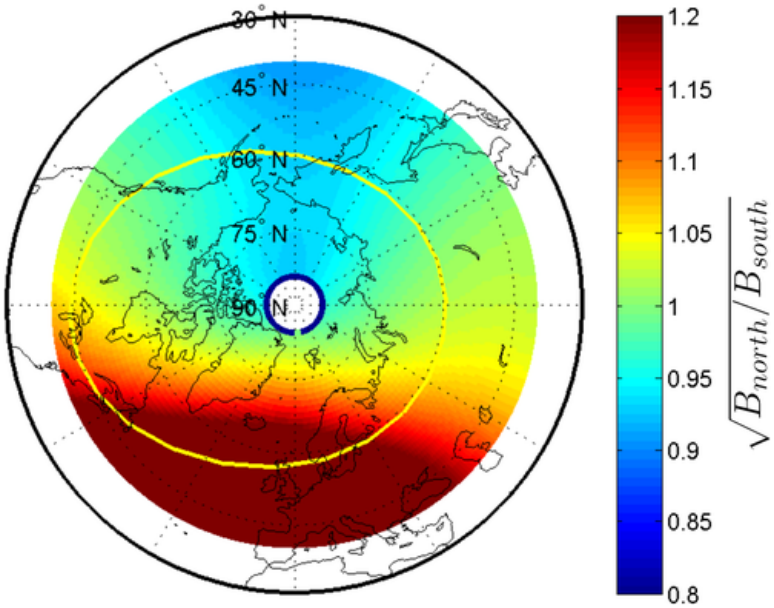

Figure 5.5: Square root of the ratio between the magnetic field strength in NH and SH found by magnetic field tracing using the IRGF, from [Zawedde et al., 2016]

Considering the geographic coverage in Figures 5.3 and 5.4, there is a difference in the sampling distribution between POES/TED and DMSP/SSJ. Highlighted even more in Figure 5.6, which shows the ratio between the sampling rate for TED and SSJ (ratio= $\frac{TED}{SSJ}$). For Kp=0-4 TED samples consistently more in the longitudinal sector between 90° and 180° East. This co-inside partly inside the region with weakest magnetic field in the NH. In other words, inside the region where one would expect more flux of electrons. For Kp=5 POES/TED samples most between 180-270° E, which is also partially inside the region of weakest NH magnetic field. DMSP/SSJ has the highest sample rate between 335-90° E for higher latitudes, in an area of where the ratio is around 1. For lower latitudes DMSP samples most frequently from longitudinal area between 75-90° E and 285-0° E. For all latitudes DMSP/SSJ has a clear pattern of lower samples rates between 100° and 180° E longitude. DMSP/SSJ then samples both from the regions where the ratio is 1 and from the regions of stronger magnetic field in the NH than SH.

Since the detectors sample from two different regions, the theory proposed by *Barth et al.* [2001] could then potentially explain discrepancies between the Kp-averaged flux levels from TED 0° observations and from DMSP/SSJ 9.45 keV observations. Based on the differences in the sampling rate distribution we expect to observe the DMSP/SSJ flux levels to be depressed compared to POES/TED. However, as Figure 4.12 and Table 5 shows, the DMSP/SSJ consistently detects higher flux levels than POES/TED for MLT 6-9, opposite to what we would have expected based on the different sampling distributions. Figure 5.6 might help explain some of it. While it clearly shows POES/TED sampling more from the region of weaker NH magnetic field, it also POES/TED sampling at a higher rate above Scandinavia than DMSP/SSJ. The pattern hols for Kp levels 0 to 4. For Kp=5, the pattern of which detector has higher sampling rate is more random. Figure 5.6 shows then that while POES/TED best sampling area co-insides inside the region of weaker region of magnetic field, it still has higher sampling rates compared to DMSP/SSJ over parts of the region with stronger field. Another likely reason is the relative small difference between sampling rates over the grid for both detectors. For both detectors, between 75° and 45° N latitude, the sampling rates lie between ∼3-6% for all longitudinal sectors. Meaning the ratio between 0.5 and 1.5 between POES/TED and DMSP/SSJ found in 5.6 translates only to differences between 1-3% in sampling rates between POES/TED and DMSP/SSJ. The relative uniformity of the sampling distributions found both detectors for Kp≤3 in Figures 5.3 and 5.4, further implies a considerable even geographic contribution to our estimated flux levels. While 5.6 illustrates a clear geographically longitude pattern in sampling rates between POES/TED and DMSP/SSJ, the uniformity of the sampling rates shown in Figures 5.3 5.4 means the the longitudinal difference in contribution to the estimated flux levels are minimal. Furthermore, 5.6 showed that both detectors had higher sampling rates inside the region of stronger magnetic field compared to the other. It is therefore concluded that for MLT sector 6-9 the bias in the geomagnetic field most likely didn't affect our results.

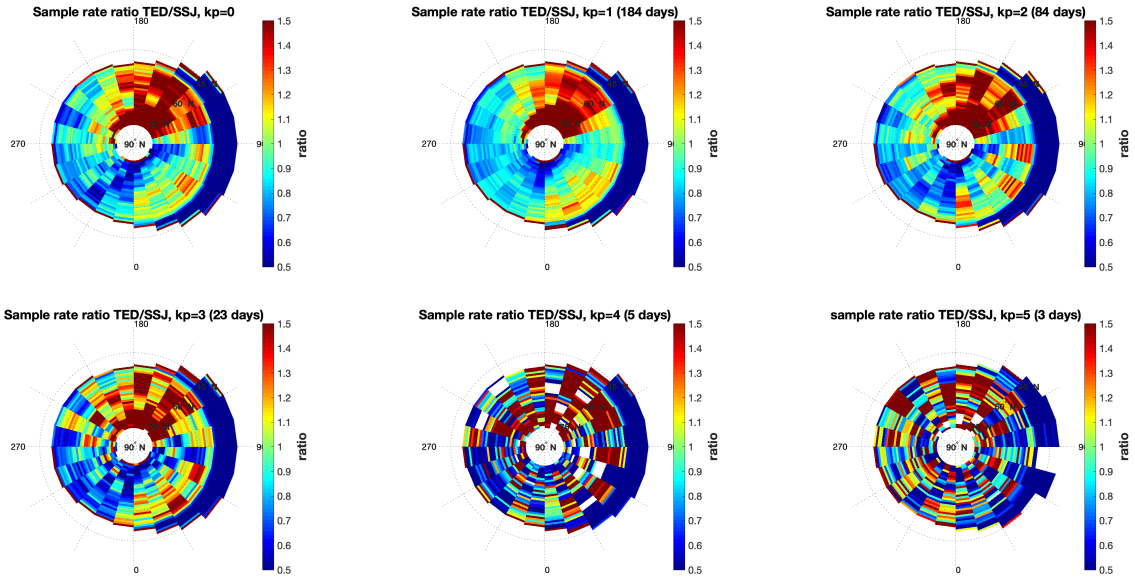

Figure 5.6: Geographic sampling rate ratio between TED 0° CH 4 and DMSP/SSJ 9.45 keV $(\frac{TED}{SSJ})$

5.3 Electron flux spectra and best fits

In order to convert the observed electron fluxes into a realistic ionisation rate profile, an accurate description of the energy spectrum are needed. This section addresses the different shapes of the spectra and how their occurrence rates fits previous studies. Moreover, potential dependence on latitude, MLT, and geomagnetic activity can provide information on the magnetospheric origin and the associated acceleration processes.

Systematic latitude differences in the shape of the electron energy spectra can potentially unravel features related to the magnetospheric origin of the electrons. The comparison in Figures 4.13 and 4.14 shows three different the average energy spectra for three different CGM latitudes, 60°, 67°, and 75° N for the morning MLT sector 6-9. For high latitudes, 75° N the Maxwellian spectra provide the best fit for the energy spectra, while at low latitudes 60° N the Maxwellian spectra rarely can describe the energy flux spectra. The low latitudes are most likely associated with the ring current and/or the radiation belts, with relative more fluxes at the higher energy range. The lack of the Maxwellian spectra for low latitudes appear in contrast to *McIntosh and Anderson* [2014]. The statistic might, however, not be directly comparable considering that they do not consider power law or exponential. On the other hand, the occurrence rate at high latitudes appear to be better in line with the findings of *McIntosh and Anderson* [2014]. The same applies to the midlatitude spectra at CGM latitude 67° N.

Table 7 revealed a systematic best fit tendency for all three detectors for CGM latitude 75°. For all three detectors, MLT sector 9-12 had a significant decrease of Maxweliian best fit and increase in exponential best fit. The same pattern can also be seen for MLT sector

18-21, however, it is less severe for the two TED detectors. For CGM latitude 67°, there is no MLT pattern for all three detectors, however the specific detectors experience individual MLT variations. For TED 0° Power law or Maxwellian is the best fit for nightside MLT sectors (0-3, 3-6, 18-21) plus MLT sector 15-18, while exponential is the best fit for the two morning sectors (6-9, 9-12 MLT). For TED 30° a similar pattern could also be found, however it was less consistent. DMSP/SSJ observed the exponential spectra to most often provide the best description of the energy flux spectra for all MLT sectors except 15-18 and 18-21. For CGM latitude 60°, only TED 30° had a systematic MLT trend, where power law provided the best description of the energy spectra for all MLT sectors besides 0-3 and 18-21 MLT. For 0-3 and 18-21 MLT, the exponential distribution provided most often the best fit. That there is MLT variations for the spectra is not surprising, considering that common wave particle interactions typically have strong MLT variability, with the exception of ULF waves [*Baker*, 2021].

In our results, there was no general Kp dependency over the three CGM latitudes, detectors and distributions. Meaning Kp, in and of itself, would not be a reliable predictor of the shape of the flux spectra. However, for specific distributions, at specific CGM latitudes, Kp trends could be found. At 60° CGM latitude, for an example, the power law showed to be the best fit for all three detectors at Kp = 5. For the Maxwellian, with the exception of POES/TED 30° at 67° CGM latitude, there was low Kp dependency. This corresponds with the results found in *McIntosh and Anderson* [2014], see their Table 2, which characterised over 30 million precipitation maps from DMSP/SSJ either with Maxwellian or Kappa fits, or monoenergetic or broadband precipitation. They found Maxwellian was the best fit 42-49% of bins for Kp=0-5, meaning Maxwellian fits had low dependence on Kp level, consistent with our findings.

Smith-Johnsen et al. [2018, 2017] fits TED channels 2-4 (0.688-9.457 keV, see Table 1) with either a Maxwellian or an exponential spectra, depending on the ratio between Channel 2 and 3. If Channel 2 > Channel 3, then an exponential form were assumed, if Channel 2 < Channel 3, they applied a Maxwellian fit. Our results did not confirm this qualifier when fitted over the entire TED energy spectrum, Channel 1-4 (0.154-9.457 keV). Whether Channel 2 or Channel 3 had the highest flux levels had no bearings on which distribution between Maxwellian and Exponential provided the best fit. The best fit depended more strongly on which latitude band and MLT sector. Meaning the potential different magnetospheric sources of the electrons, is the most probable explanation for which distribution would be the best fit. Moreover, considering that the chemistry climate model, WACCM, assume a Maxwellian spectra over the entire auroral oval, systematic discrepancies might be expected for mid and low latitudes based on the best fit statistic in Figure 4.13.

In this study the goodness of the different fits were evaluated against each other on the basis of their SSE values and adjusted R-square values. A critical look on these goodness of fit values is therefore important. SSE is the sum of squares errors between the observed values (the plotted flux spectra) and the predicted values (from the fit function). It is a commonly used goodness of fit evaluator, where most programming languages having

automated functions to calculate it. However, it has some drawbacks. Since it takes the sum of square errors, it is considerably sensitive to outliers. For TED 0° and 30°, where there is only 4 data points, an outlier could have significant ramifications for the SSE value, as a single point represents 25% of the data. SSE is therefore often used with the goal of minimising the error by removing outliers. However, just continuing removing outliers would eventually make the fit redundant. Considering that we are looking at spectra from averaged fluxes, it is not easy to credibly call a data point in the spectra an outlier. The estimated flux levels have decent statistics behind them, with the averages calculated from 100-3,000+ data points (see Figures 4.2 and 4.6). For both SSE and adjusted R-square, what constitutes a good fit is subjective and dependent on what the model/fit is predicting. For instance, an adjusted R-square value below 0.3 could still constitute a "good fit", depending on what is being fitted. Similarly, an SSE of 1-2 could still be considered a "good fit" depending on the data. In this study, however, we are 1) comparing different fits to each other, and 2) the goodness of the fits generally had SSE values close to zero and adjusted R-square values close to 1. Hence, there was not essential to make specific assumptions on what values constituted a "good fit".

5.4 Pointing direction of the detectors

In section 4.2.3, latitudinal discrepancies between the DMSP/SSJ channels 9.45 keV and 6.46 keV, POES/TED 0° and POES/TED 30° were found in response to increased geomagnetic activity. In Table 5 and 6, there was a notable difference found between the relative difference as function of Kp for CGM latitudes 66° and 65° compared to 75°. For the equatorward edge of the CGM latitude interval, the relative difference decreased significantly from Kp=1 to Kp=5, while for 75° the relative difference increased. Figure 4.11 and 4.12 show that for Kp=0 the difference favours POES/TED towards 75° latitude and favours DMSP/SSJ towards 60° in MLT sector 18-21,. For Kp=5, however, the area around 60° latitude favours the POES/TED detectors, while the difference towards 75° slightly favours the DMSP/SSJ channels.

This latitudinal discrepancy in response to increased geomagnetic activity could potentially be explained by the different pointing directions of the detectors relative to the local magnetic field. The pointing directions of the detectors will matter when we have strong pitch angle anisotropy [*Nesse Tyssøy et al.*, 2016]. This potential explanation is given further credence by the discrepancy in response found between the two TED detectors at these latitudes. The relative difference in favour of the DMSP/SSJ is considerably smaller for POES/TED 0° at Kp=1 for CGM latitudes 65° and 66°, as seen in Table 6, at 7.4-7.8% vs 12.4-12.7%. The relative difference however shrinks to the same level for Kp=5, at 3.7-3.8%. Meaning TED 30° detected a higher flux response compared to TED 0° at these latitudes for MLT 18-21, which can also be seen in Figure 4.5. For the most part, the auroral electrons (1-30 keV) precipitating down to the lower thermosphere from the magnetospheric plasma sheet are often assumed to be isotropic, however studies have shown this isn't always the case [*Walsh et al.*, 2013; *Dombeck et al.*, 2018]. *Nesse Tyssøy et al.* [2016] looks at this problem regarding the other SEM-2 instrument MEPED. However, due to the fact that MEPED detects electrons >30 keV, their technique does not apply to

our study, since the pitch angle distributions for auroral electrons can be accelerated by the parallel electric field [*Kaufmann et al.*, 1976]. However, the findings in *Nesse Tyssøy et al.* [2016], that the direction of detector will determine the flux levels observed when experiencing strong pitch angle anisotropy, could still be relevant for our results.

5.5 WACCM

Auroral electrons (1-30 keV), from the plasma sheet, have sufficient energy to reach the lower thermosphere and upper mesosphere. The electrons ionises the atmosphere, initiating a series of chemical reactions which leads to increased production of NO_x gasses. In the polar winter thermosphere, the NO production is mainly due to EPP. A realistic energy input is therefore important to accurately reproduce the production and composition of NO (or ions in general) at lower thermospheric altitudes. While WACCM has been repeatedly updated and improved [*Gettelman et al.*, 2019], questions still remain regarding its ability to reproduce the levels of NO observed in the lower thermosphere [*Randall et al.*, 2015; *Smith-Johnsen et al.*, 2018, 2022]. The NO production levels can be considered as a proxy for the ionisation rates, since there is a direct correlation between them. Comparison between the NO production in the lower thermosphere for WACCM and the observed NO density by satellites over an 8 year period in the southern hemisphere, found both overestimated background levels and underestimated short-term variability in NO [*Hendrickx et al.*, 2018]. Moreover, this has been supported by both event-based and statistical studies [*Smith-Johnsen et al.*, 2018, 2022]. *Smith-Johnsen et al.* [2018] examine the NO response to a geomagnetic storm event in april 2010, and finds both high pre-storm background levels of NO and weak response to increased geomagnetic activity in comparison with observations from satellites. When comparing the NO levels from WACCM and satellite observations over the year 2010 for the altitude region 90-115 km, *Smith-Johnsen et al.* [2022] finds WACCM overestimating the levels of NO in the lower thermosphere compared to satellite observations, in particular during periods of low geomagnetic activity.

In section 4.4, WACCM's daily ionisation rates, averaged over daily Kp for the year 2010, were compared to AIMOS for altitudes ∼112 km and ∼95 km. The comparison demonstrated that WACCM systematically implements higher ionisation rate levels for lower Kp (0,1,2) compared to AIMOS, while AIMOS calculated higher ionisation rate for higher Kp levels (4,5) compared to WACCM. Moreover, during high geomagnetic activity the latitudinal extent of the auroral oval was significantly wider in AIMOS compared to WACCM. Hence, based on the NO level found in WACCM, this confirms that WACCM overestimates the NO production during geomagnetic quiet periods and underestimates it during geomagnetic active periods, consistent with the findings of *Smith-Johnsen et al.* [2018] and *Smith-Johnsen et al.* [2022].

Figures 5.7 shows the peak ionisation rate over the entire grid for WACCM and AIMOS, for altitude ∼112 km, before and after period of high geomagnetic activity, days 90-99, which corresponds to early April 2010 and the event studied by *Smith-Johnsen et al.* [2018]. The first period during days 90-94, when Kp$\leq$ 3, WACCM is consistently higher than AIMOS, by around half an order of magnitude. However, in the period of high

geomagnetic activity, days 96 and 97, the roles are reversed and there is a clear difference between the peak ionisation's rates in the two models. For AIMOS, the slope from the period with lower Kp levels up to Kp=5, from day 92 to 96, is incredibly steep. AIMOS has a much larger sensitivity in response to geomagnetic activity, where the peak ionisation rate increases more than an order of magnitude. AIMOS peak ionisation rate goes from $4.4 \cdot 10^9$ to $6.9 \cdot 10^{10}$, around 15 times higher. For WACCM, however, the slope for peak ionisation rate is very gradual from period of low Kp to the period of high Kp. The peak ionisation rate for WACCM goes from $\sim 1 \cdot 10^{10}$ for lower Kp to $\sim 2.4 \cdot 10^{10}$. In other words, the peak ionisation rate more than doubles between low to high geomagnetic activity in WACCM, which is a significantly lower increase compared to AIMOS. After the period of high geomagnetic activity (days 97-99), AIMOS again falls off much more steeply than WACCM. After day 97, WACCM again implements higher peak ionisation rates than AIMOS. Considering the implication for the NO production rates, Figure 5.7 implies consistency with what was found *Smith-Johnsen et al.* [2018] for the same time period, when comparing WACCM with satellite observations, as well as further confirming the results of *Hendrickx et al.* [2018].

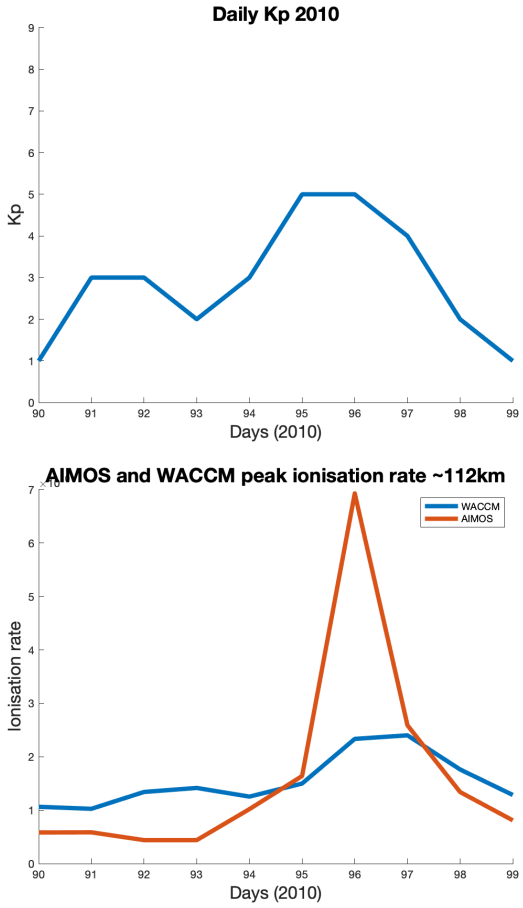

Figure 5.7: Max ionisation rate for the entire grid for both WACCM and AIMOS for altitude ~112km, before, during and after period of high geomagnetic activity in early April 2010

Relating back to the results find from the observed flux observations in section 4.2 and how their ionisation profile would potentially look like compared to WACCM and AIMOS. It seems most likely they would closer match the estimated ionisation peaks of AIMOS than WACCM. This belief is due to the matched increase in intensity as a function of Kp between POES/TED and AIMOS, as found in section 4.3. The latitudinal response, however, is less conclusive. Since section 4.3 found the latitude extent of the auroral oval as defined by AIMOS to increase more equatorwards than detected by POES/TED

In section 4.4, the contrast in response to geomagnetic activity between AIMOS and WACCM was shown to increase with decreasing altitude. The most probable explanation for this discrepancy, is the difference in energy spectra assumed for the electron fluxes. WACCM assumes the auroral electrons to have a Maxwellian energy distribution with a fixed energy of 2 keV [*Smith-Johnsen et al.*, 2018]. This results in a energy deposition as function of altitude which always peaks around 110km [*Smith-Johnsen et al.*, 2018] (see their Figure 1). AIMOS, on the other hand, assumes a power law spectrum with up to 5 different power law indices [*Wissing and Kallenrode*, 2009]. Meaning AIMOS' energy deposition as a function of altitude will have different shape to that of WACCM. *Wissing et al.* [2010] looks at the electron ionisation rate altitude profile from AIMOS before, during and after an geomagnetic event. Their Figure 5 shows increased sensitivity to the event for altitudes below 100km than above, which is consistent with our results for AIMOS at $\sim$ 112 and $\sim$95 km altitude. This could be due to influence of energy deposition from higher energy electrons at altitudes below 100 km in AIMOS, see Figure 2 in *Wissing and Kallenrode* [2009].

6 Conclusion / Summary

The overarching goal of this thesis is to study the variations of auroral EPP as a function of Kp. The main focus is in the observed auroral electron fluxes as a function of Kp. Here observations from the TED onboard POES spacecrafts are compared with observations from the SSJ detector onboard DMSP satellites. The comparison is made by binning the data into 1° CGM latitude x 3h MLT bins and calculate the average over daily Kp levels for the year 2010. Differences and similarities between the high energy channel from TED, energy range 6.503-9.457 keV, and two SSJ channels, centred on 6.46 keV and 9.45 keV was explored.

The study reveals notable discrepancies between the particle detectors. In general, for all latitudes, MLT sectors and Kp levels, the two SSJ channels observed higher levels of flux compared to the two TED detectors. The difference is particular significant below 60° CGM latitude, where the averages based on SSJ observations were 0.5-1 order of magnitude higher. The difference at these low latitudes holds for all Kp, due to the similar response to increased geomagnetic activity (or more accurately lack thereof). Moving inside the auroral oval the discrepancy is less pronounced. The relative difference usually falls between 4-8% in favour of the two SSJ channels, with the exception of MLT sector 18-21. Here, the two TED detectors observe higher flux levels compared to SSJ at some latitudes. Since, this is limited to the evening sector, it implies a day and night discrepancy between the detectors. In response to increased Kp, all detectors experienced significant increase in both flux level and latitudinal extent of the auroral oval. Overall, especially on the dayside, SSJ observe a stronger response to geomagnetic activity. Inside the auroral oval, for MLT 18-21, however, the detectors observe the flux difference between them decrease towards the equatorward end, while it increases in favour of the SSJ channels towards the polarward end for increased activity. This result implies a latitude dependent response to increased activity by the different detectors and could potentially be understood as an artefact due to the detectors pointing directions if the flux pitch angle distribution is anisotropic.

Further, a study of the shape of the electron energy flux spectra is performed for three CGM latitudes (60°, 67° and 75°). For 60° CGM latitude, the SSJ and TED 0° agree well for low and high Kp, where the exponential distributions best described the spectra for Kp=0,1 and power law described the spectra best for Kp=5. For TED 30°, however, the power law distributions was the best fit for all Kp, except Kp=2. For CGM latitude 67°, the shape of the spectra is more varied for all three detectors. For TED 0°, there were Kp levels where all the different fits were dominating. For the SSJ observations, an exponential function provided the best fit for lower Kp levels, decreasing gradually with increasing Kp, which contrasted with power law.. The fluxes observed by the TED 30° detector fitted best with a Maxwellian function and have a clear positive Kp trend. At 75° CGM latitude, all three detector observations demonstrated consistent Maxwellian best fits, both as a function of Kp and in terms of MLT variability. Here the Maxwellian function is likely to be the best description for all Kp levels, and all MLT sectors with the exception of MLT 9-12 and 18-21. This thesis finds that the shape of the electron energy flux spectra depends most on latitude and MLT, and less on Kp/geomagnetic activity. This implies that the

magnetospheric origin of the electrons are likely to decide the shape of the observed spectra. A qualitative comparison between the ionisation rates estimated by AIMOS, and the fluxes observed by TED and SSJ, reveals similar increase in magnitude in response to increased Kp within the auroral oval (60-75° CGM latitude),. However, AIMOS predicts that the MLT sector with strongest ionisation changes with Kp, a feature which is not evident in neither TED nor SSJ. Lastly, AIMOS estimate a larger expansion of the equatorward edge of the auroral oval compared to TED in response to increased geomagnetic activity.

The final comparison explored differences between AIMOS and WACCM and their response to increased geomagnetic activity. AIMOS appears to be more sensitive, with higher increase both in terms of strength and size of the auroral oval, as a function of Kp compared to the ionisation rates implemented in WACCM. By comparing two different altitudes in the lower thermosphere ($\sim$112 km and $\sim$95 km), this discrepancy increased with decreasing altitude. Compared to AIMOS, WACCM overestimates the ionisation rates for low geomagnetic activity, and underestimate the ionisation rates for high activity consistent with previous studies.

To summarise, this thesis has shown:

- Both DMSP/SSJ and POES/TED detected increased electron fluxes and a wider auroral oval with increasing geomagnetic activity.
- DMSP/SSJ consistently measured higher levels of flux compared to POES/TED, with the exception of MLT sector 18-21 where there were no clear trend.
- DMSP/SSJ had relative higher response to increased Kp compared to POES/TED.
- Both DMSP/SSJ and POES/TED appeared to have a latitude dependent response to increased activity, which suggests that the pointing directions of the detectors relative to the magnetic field might have affected our results.
- The electron flux spectra were first and foremost dependent on latitude, followed by MLT, and less on Kp.
- AIMOS estimated a similar increase in magnitude compared with DMSP/SSJ and POES/TED, however, the model projected a higher increase in the width of the auroral oval compared to the observations made by the particle detectors
- $\mathrm{IR}_{WACCM} > \mathrm{IR}_{AIMOS}$ for periods of low geomagnetic activity and $\mathrm{IR}_{WACCM} < \mathrm{IR}_{AIMOS}$ for periods of high geomagnetic activity.

7 Future Work

Based on the recent research presented in Section 4.2, the SOLARIS-HEPPA (Solar Influences for SPARC-High Energy Particle Precipitation in the Atmosphere) Working Group 5 has decided to turn their focus towards the quantification of the auroral energy input in the fourth High Energy Particle Precipitation in the Atmosphere (HEPPA) Intercomparison projects. Similarly, to the title of this thesis they ask: What is the flux of auroral electrons in the lower thermosphere? And how well is it parameterised in current chemistry-climate models? The HEPPA intercomparison experiments are designed to advance the EPP research with community-wide, collective efforts. While the HEPPA I experiment assessed the atmospheric impact of the Halloween 2003 solar proton event [*Funke et al.*, 2011], and HEPPA II focused on the 2009 wintertime transport of EPP-NOx [*Funke et al.*, 2017], HEPPA III aimed to improve the representation of medium energy electrons (>30 keV) in atmosphere and climate models [*Nesse Tyssøy et al.*, 2022; *Sinnhuber et al.*, 2022]. This thesis marks the starting gun for the HEPPA IV intercomparison project. The thesis raises several questions that should be investigate in the future.

- The current thesis is intended as a pilot study, limited to the year 2010. A natural first step, to increase the statistics, as well as examine solar cycle variability will be to include data from a full solar cycle.
- Can the discrepancies found between the different particle detectors be explained by their different viewing directions? Here, a more systematic evaluation the pitch angle distribution of the fluxes needs to be addressed. This thesis has used DMSP/SSJ data from the year 2010. During this period, both SSJ/4 and SSJ/5 were operational and in orbit. Due to SSJ/5's larger FOV, the two detectors is effectively not observing the same particle populations for the descending and ascending phase of an orbit [*Redmon et al.*, 2017a]. This naturally leads to the potential for conducting a systematic evaluation of the differences observed by the two SSJ detectors (and how they relate back to TED 0° and TED 30°).
- A natural follow up step is to convert the POES/TED and DMSP/SSJ fluxes and energy spectra into ionisation rate calculations. This will enable a direct comparison of the empirical data and the model projections. Furthermore, here one can play with different assumptions on the energy spectra of the electrons and study how they potentially change the ionisation profile as a function of altitude.
- The model projections, AIMOS and WACCM, is based on particle detector observations and UV observations, respectively. Could this be part of the explanation for their discrepancies in both intensity and latitude, and different sensitivity to the varying Kp-levels? Here a comparison of flux estimates based on different measurement techniques and the associated assumptions needs to be taken into account. Moreover, a third measurement technique like e.g. incoherent scatter radars, such as EISCAT (def. acronym), might provide a potential validation source in this respect.
- Finally, an in-depth understanding of the measurement techniques, alongside the how the observations respond to varying geomagnetic activity might provide a foundation

for a future, improved parameterisation to be implemented into chemistry climate models to better assess the effects of energetic electrons on the atmosphere.

Acronyms

AIM Aeronomy of Ice in the Mesosphere.

AIMOS Atmospheric Ionization Module Osnabrück.

CAM Community Atmosphere Model.

CESM Community Earth System Model.

CGMlat Corrected Geomagnetic Latitude.

CIR Co-Rotating Interaction Region.

CME Coronal Mass Ejections.

DMSP Defense Meteorological Satellite Program.

EPP Energetic Particle Precipitation.

HEPPA High Energy Particle Precipitation in the Atmosphere.

HP Hemispheric Power.

IMF Interplanetary Magnetic Field.

IR Ionisation Rate.

LEO Low Earth Orbit.

MEPED Medium Energy Proton and Electron detector.

MetOp Meteorological Operational satellite.

Mlat Magnetic Latitude.

MLT Magnetic Local Time.

NCAR National Center for Atmospheric Research.

NOAA National Oceanic and Atmospheric Administration.

POES Polar Orbiting Environmental Satellite.

SOFIE Solar Occultation For Ice Experiment.

SOLARIS Solar Influences for SPARC.

SPARC Stratosphere-troposphere Processes and their Role in Climate.

TED Total Energy Detector.

WACCM Whole Atmosphere Community Climate Model.

Bibliography

Anderson, J. D. (2001), *Fundamentals of aerodynamics*, 3th ed., McGraw-Hill. 12

Anderson, P. C. (2012), Characteristics of spacecraft charging in low earth orbit, *Journal of Geophysical Research: Space Physics*, *117*(A7), doi:https://doi.org/10.1029/2011JA016875. 77, 78

Anderson, P. C., and H. C. Koons (1996), Spacecraft charging anomaly on a low-altitude satellite in an aurora, *Journal of Spacecraft and Rockets*, *33*(5), 734–738, doi:10.2514/3.26828. 77

Andersson, M. E., P. T. Verronen, S. Wang, C. J. Rodger, M. A. Clilverd, and B. R. Carson (2012), Precipitating radiation belt electrons and enhancements of mesospheric hydroxyl during 2004–2009, *Journal of Geophysical Research: Atmospheres*, *117*(D9), doi:https://doi.org/10.1029/2011JD017246. 1

Babcock, H. W. (1961), The Topology of the Sun's Magnetic Field and the 22-YEAR Cycle, *apj*, *133*, 572, doi:10.1086/147060. 4, 5

Baker, D. N. (2021), Wave–particle interaction effects in the van allen belts, *Earth, Planets and Space*, doi:\url{https://doi.org/10.1186/s40623-021-01508-y}. 85

Bame, S. J., J. R. Asbridge, H. E. Felthauser, E. W. Hones, and I. B. Strong (1967), Characteristics of the plasma sheet in the earth's magnetotail, *Journal of Geophysical Research (1896-1977)*, *72*(1), 113–129, doi:https://doi.org/10.1029/JZ072i001p00113. 21

Bartels, J., N. H. Heck, and H. F. Johnston (1939), The three-hour-range index measuring geomagnetic activity, *Terrestrial Magnetism and Atmospheric Electricity*, *44*(4), 411–454, doi:https://doi.org/10.1029/TE044i004p00411. 22

Barth, C. A., D. N. Baker, K. D. Mankoff, and S. M. Bailey (2001), The northern auroral region as observed in nitric oxide, *Geophysical Research Letters*, *28*(8), 1463–1466, doi:https://doi.org/10.1029/2000GL012649. 78, 81, 82, 83

Baumgaertner, A., P. Jöckel, and C. Brühl (2009), Energetic particle precipitation in echam5/messy1-part 1: Downward transport of upper atmospheric nox produced by low energy electrons, *Atmospheric Chemistry and Physics, v.9, 2729-2740 (2009)*, *9*, doi:10.5194/acp-9-2729-2009. 28

Baumjohann, W., and R. A. Treumann (1996), *Basic space plasma physics*, doi:10.1142/p015. 3, 7, 8, 9, 10, 11, 12, 13, 15, 16, 17, 18, 19, 20, 21, 29, 82

Birkeland, K. (1908), *The Norwegian aurora polaris expedition, 1902-1903*, Christiania, H. Aschelhoug. 24, 29

Bohren, C., and E. Clothiaux (2008), *Fundamentals of Atmospheric Radiation: An Introduction with 400 Problems*, doi:10.1002/9783527618620. 3, 26, 32

Brasseur, G., and S. Solomon (2005), *Aeronomy of the Middle Atmosphere: Chemistry and Physics of the Stratosphere and Mesosphere*, doi:10.1007/1-4020-3824-0. 27

Cai, Y., X. Yue, W. Wang, S. Zhang, L. Liu, H. Liu, and W. Wan (2019), Long-term trend of topside ionospheric electron density derived from dmsp data during 1995-2017, *Journal of Geophysical Research: Space Physics*, *124*, doi:10.1029/2019JA027522. 38

Carpenter, D. L. (1963), Whistler evidence of a 'knee' in the magnetospheric ionization density profile, *Journal of Geophysical Research*, *68*(6), doi:10.1029/JZ068i006p01675. 18

Chappell, C. R., K. K. Harris, and G. W. Sharp (1970), A study of the influence of magnetic activity on the location of the plasmapause as measured by ogo 5, *Journal of Geophysical Research (1896-1977)*, *75*(1), 50–56, doi:https://doi.org/10.1029/JA075i001p00050. 18

Chen, P. (2011), Coronal mass ejections: Models and their observational basis, *Living Reviews in Solar Physics*, *8*, doi:10.12942/lrsp-2011-1. 6

College, B. (2022), Layers of the atmosphere, `https://dmsp.bc.edu/html2/ssj5_inst.html`, accessed: 26.03.22. 39

Colson, A. D., and J. I. Minow (2011), Dmsp spacecraft charging in auroral environments, `https://ntrs.nasa.gov/citations/20120004173`. 77, 78

Cowley, S. (1991), The structure and length of tail-associated phenomena in the solar wind downstream from the earth, *Planetary and Space Science*, *39*(7), 1039–1043, doi:https://doi.org/10.1016/0032-0633(91)90110-V. 15

Cowley, S., and M. Lockwood (1992), Excitation and decay of solar wind-driven flows in the magnetosphere-ionosphere system, *Annales Geophysicae*, *10*, 103–115. 16

Cranmer, S. R. (2009), Coronal holes, *Living Reviews in Solar Physics*, *6*, doi:10.12942/lrsp-2009-3. 7

Crutzen, P. J., I. S. A. Isaksen, and G. C. Reid (1975), Solar proton events: Stratospheric sources of nitric oxide, *Science*, *189*(4201), 457–459, doi:10.1126/science.189.4201.457. 1

Daglis, I. A., R. M. Thorne, W. Baumjohann, and S. Orsini (1999), The terrestrial ring current: Origin, formation, and decay, *Reviews of Geophysics*, *37*(4), 407–438, doi:https://doi.org/10.1029/1999RG900009. 20

Doe, R. A., M. B. Moldwin, and M. Mendillo (1992), Plasmapause morphology determined from an empirical ionospheric convection model, *Journal of Geophysical Research: Space Physics*, *97*(A2), 1151–1156, doi:https://doi.org/10.1029/91JA01649. 18

Dombeck, J., C. Cattell, N. Prasad, E. Meeker, E. Hanson, and J. McFadden (2018), Identification of auroral electron precipitation mechanism combinations and their relationships to net downgoing energy and number flux, *Journal of Geophysical Research: Space Physics*, *123*(12), 10,064–10,089, doi:https://doi.org/10.1029/2018JA025749. 86

Dungey, J. W. (1961), Interplanetary magnetic field and the auroral zones, *Phys. Rev. Lett.*, *6*, 47–48, doi:10.1103/PhysRevLett.6.47. 15

Dungey, J. W. (1965), The length of the magnetospheric tail, *Journal of Geophysical Research (1896-1977)*, *70*(7), 1753–1753, doi:https://doi.org/10.1029/JZ070i007p01753. 15

Efron, B. (1979), Bootstrap Methods: Another Look at the Jackknife, *The Annals of Statistics*, *7*(1), 1 – 26, doi:10.1214/aos/1176344552. 32

Evans, D., and M. Greer (2004), Polar orbiting environmental satellite space environment monitor - 2 instrument descriptions and archive data documentation, *NOAA Tech. Memo. 1.4*. 36, 37

Frooninckx, T. B., and J. J. Sojka (1992), Solar cycle dependence of spacecraft charging in low Earth orbit, *jgr*, *97*(A3), 2985–2996, doi:10.1029/91JA02704. 77

Funke, B., A. Baumgaertner, M. Calisto, T. Egorova, C. Jackman, J. Kieser, A. Krivolutsky, M. López-Puertas, D. Marsh, T. Reddmann, E. Rozanov, S.-M. Päivärinta, M. Sinnhuber, G. Stiller, P. Verronen, S. Versick, T. Clarmann, T. Vyushkova, N. Wieters, and J. Wissing (2011), Composition changes after the "halloween" solar proton event: the high energy particle precipitation in the atmosphere (heppa) model versus mipas data intercomparison study, *Atmospheric Chemistry and Physics*, *11*, doi:10.5194/acp-11-9089-2011. 39, 40, 92

Funke, B., M. López-Puertas, G. P. Stiller, and T. von Clarmann (2014), Mesospheric and stratospheric noy produced by energetic particle precipitation during 2002–2012, *Journal of Geophysical Research: Atmospheres*, *119*(7), 4429–4446, doi:https://doi.org/10.1002/2013JD021404. 1

Funke, B., W. Ball, S. Bender, A. Gardini, V. L. Harvey, A. Lambert, M. López-Puertas, D. R. Marsh, K. Meraner, H. Nieder, S.-M. Päivärinta, K. Pérot, C. E. Randall, T. Reddmann, E. Rozanov, H. Schmidt, A. Seppälä, M. Sinnhuber, T. Sukhodolov, G. P. Stiller, N. D. Tsvetkova, P. T. Verronen, S. Versick, T. von Clarmann, K. A. Walker, and V. Yushkov (2017), Heppa-ii model–measurement intercomparison project: Epp indirect effects during the dynamically perturbed nh winter 2008–2009, *Atmospheric Chemistry and Physics*, *17*(5), 3573–3604, doi:10.5194/acp-17-3573-2017. 92

Ganushkina, N. Y., I. Dandouras, Y. Y. Shprits, and J. Cao (2011), Locations of boundaries of outer and inner radiation belts as observed by cluster and double star, *Journal of Geophysical Research: Space Physics*, *116*(A9), doi:https://doi.org/10.1029/2010JA016376. 18

Gettelman, A., M. J. Mills, D. E. Kinnison, R. R. Garcia, A. K. Smith, D. R. Marsh, S. Tilmes, F. Vitt, C. G. Bardeen, J. McInerny, H.-L. Liu, S. C. Solomon, L. M. Polvani, L. K. Emmons, J.-F. Lamarque, J. H. Richter, A. S. Glanville, J. T. Bacmeister, A. S. Phillips, R. B. Neale, I. R. Simpson, A. K. DuVivier, A. Hodzic, and W. J. Randel (2019), The whole atmosphere community climate model version 6 (waccm6), *Journal*

of Geophysical Research: Atmospheres, *124*(23), 12,380–12,403, doi:https://doi.org/10.1029/2019JD030943. 41, 87

Gonzalez, W. D., B. T. Tsurutani, and A. L. Clúa de Gonzalez (1999), Interplanetary origin of geomagnetic storms, *Space Science Reviews*, doi:10.1023/A:1005160129098. 22

Gray, L. J., J. Beer, M. Geller, J. D. Haigh, M. Lockwood, K. Matthes, U. Cubasch, D. Fleitmann, G. Harrison, L. Hood, J. Luterbacher, G. A. Meehl, D. Shindell, B. van Geel, and W. White (2010), Solar influences on climate, *Reviews of Geophysics*, *48*(4), doi:https://doi.org/10.1029/2009RG000282. 26

Griffiths, D. (2017), *Introduction to Electrodynamics*, doi:10.1017/9781108333511. 76

Gringauz, K. I. (1963), The structure of the ionized gas envelope of earth from direct measurements in the u.s.s.r. of local charged particle concentrations, *Planetary Space Sci.*, doi:10.1016/0032-0633(63)90030-8. 18

Gussenhoven, M. S., D. A. Hardy, F. Rich, W. J. Burke, and H.-C. Yeh (1985), High-level spacecraft charging in the low-altitude polar auroral environment, *Journal of Geophysical Research: Space Physics*, *90*(A11), 11,009–11,023, doi:https://doi.org/10.1029/JA090iA11p11009. 77

Heikkila, W. J., and J. D. Winningham (1971), Penetration of magnetosheath plasma to low altitudes through the dayside magnetospheric cusps, *Journal of Geophysical Research (1896-1977)*, *76*(4), 883–891, doi:https://doi.org/10.1029/JA076i004p00883. 47

Hendrickx, K., L. Megner, D. R. Marsh, and C. Smith-Johnsen (2018), Production and transport mechanisms of no in the polar upper mesosphere and lower thermosphere in observations and models, *Atmospheric Chemistry and Physics*, *18*(12), 9075–9089, doi:10.5194/acp-18-9075-2018. 2, 30, 87, 88

Horne, R., R. Thorne, Y. Shprits, N. Meredith, S. Glauert, A. Smith, S. Kanekal, D. Baker, M. Engebretson, J. Posch, M. Spasojevic, U. Inan, J. Pickett, and P. Décréau (2005), Wave acceleration of electrons in the van allen radiation belts, *Nature*, *437*, 227–30, doi:10.1038/nature03939. 18

Horne, R. B., S. A. Glauert, N. P. Meredith, D. Boscher, V. Maget, D. Heynderickx, and D. Pitchford (2013), Space weather impacts on satellites and forecasting the earth's electron radiation belts with spacecast, *Space Weather*, *11*(4), 169–186, doi:https://doi.org/10.1002/swe.20023. 48

Hurrell, J., M. Holland, P. Gent, S. Ghan, J. Kay, P. Kushner, J.-F. Lamarque, W. Large, D. Lawrence, K. Lindsay, W. Lipscomb, M. Long, N. Mahowald, D. Marsh, R. Neale, P. Rasch, S. Vavrus, M. Vertenstein, D. Bader, and S. Marshall (2013), The community earth system model: A framework for collaborative research, *Bulletin of the American Meteorological Society*, *94*, 1339–1360, doi:10.1175/BAMS-D-12-00121.1. 40

Jones, D. R., and H. Schaub (2013), Periodic relative orbits of two spacecraft subject to

differential gravity and electrostatic forcing, *Acta Astronautica*, *89*, 21–30, doi:https://doi.org/10.1016/j.actaastro.2013.03.028. 77

Karavaev, A. (2010), Waves in plasmas generated by a rotating magnetic field and implications to radiation belts. 20

Kaufmann, R. L., D. N. Walker, and R. L. Arnoldy (1976), Acceleration of auroral electrons in parallel electric fields, *Journal of Geophysical Research (1896-1977)*, *81*(10), 1673–1682, doi:https://doi.org/10.1029/JA081i010p01673. 87

Kelley, M. C. (2009), *The Earth's Ionosphere: Plasma Physics and Electrodynamics* . 13, 14, 15, 16, 17, 18, 24, 25, 29, 30

Kivelson, M. G., and C. T. Russell (1995), *Introduction to Space Physics*. 15

Krivova, N. A., Balmaceda, L., and Solanki, S. K. (2007), Reconstruction of solar total irradiance since 1700 from the surface magnetic flux, *A&A*, *467*(1), 335–346, doi:10.1051/0004-6361:20066725. 26

Kwak, S., and J. Kim (2017), Central limit theorem: The cornerstone of modern statistics, *Korean Journal of Anesthesiology*, *70*, 144, doi:10.4097/kjae.2017.70.2.144. 33

Kyoto University (2022), Auroral electrojet (ae) indices, `http://wdc.kugi.kyoto-u.ac.jp/aedir/ae2/onAEindex.html`, accessed: 07.02.22. 23

Lai, S. (2011), Fundamentals of spacecraft charging: Spacecraft interactions with space plasmas, *Fundamentals of Spacecraft Charging: Spacecraft Interactions with Space Plasmas*. 76, 77

Lakhina, G. S., and B. T. Tsurutani (2016), Geomagnetic storms: historical perspective to modern view, *Geoscience Letters*, doi:10.1186/s40562-016-0037-4. 22

Laundal, K. M., and A. D. Richmond (2017), Magnetic coordinate systems, *Space Science Reviews*, *206*(1-4), 27–59, doi:10.1007/s11214-016-0275-y. 9, 10, 11

Li, W., and M. Hudson (2019), Earth's van allen radiation belts: From discovery to the van allen probes era, *Journal of Geophysical Research: Space Physics*, *124*(11), 8319–8351, doi:https://doi.org/10.1029/2018JA025940. 18

Liu, H.-L., B. T. Foster, M. E. Hagan, J. M. McInerney, A. Maute, L. Qian, A. D. Richmond, R. G. Roble, S. C. Solomon, R. R. Garcia, D. Kinnison, D. R. Marsh, A. K. Smith, J. Richter, F. Sassi, and J. Oberheide (2010), Thermosphere extension of the whole atmosphere community climate model, *Journal of Geophysical Research: Space Physics*, *115*(A12), doi:https://doi.org/10.1029/2010JA015586. 40

Lyons, L. R., and R. M. Thorne (1973), Equilibrium structure of radiation belt electrons, *Journal of Geophysical Research (1896-1977)*, *78*(13), 2142–2149, doi:https://doi.org/10.1029/JA078i013p02142. 18

Marsch, E. (2006), Origin and evolution of the solar wind, *Proceedings of the International Astronomical Union*, *2*, 259 – 268, doi:10.1017/S1743921306001980. 7, 8

Marsh, D., M. Mills, D. Kinnison, J.-F. Lamarque, N. Calvo, and L. Polvani (2013), Climate change from 1850 to 2005 simulated in cesm1(waccm), *Journal Of Climate*, *26*, 7372–7390, doi:10.1175/JCLI-D-12-00558.1. 40

McIntosh, R. C., and P. C. Anderson (2014), Maps of precipitating electron spectra characterized by maxwellian and kappa distributions, *Journal of Geophysical Research: Space Physics*, *119*(12), 10,116–10,132, doi:https://doi.org/10.1002/2014JA020080. 33, 63, 84, 85

McPherron, R. L. (1979), Magnetospheric substorms, *Reviews of Geophysics*, *17*(4), 657–681, doi:https://doi.org/10.1029/RG017i004p00657. 24

Milan, S. E. (2004), A simple model of the flux content of the distant magnetotail, *Journal of Geophysical Research: Space Physics*, *109*(A7), doi:https://doi.org/10.1029/2004JA010397. 15

Milan, S. E., G. Provan, and B. Hubert (2007), Magnetic flux transport in the dungey cycle: A survey of dayside and nightside reconnection rates, *Journal of Geophysical Research: Space Physics*, *112*(A1), doi:https://doi.org/10.1029/2006JA011642. 15, 16

Moffett, R. J., G. J. Bailey, S. Quegan, Y. Rippeth, A. M. Samson, and R. Sellek (1989), Modelling the ionospheric and plasmaspheric plasma [and discussion], *Philosophical Transactions of the Royal Society of London. Series A, Mathematical and Physical Sciences*, *328*(1598), 255–270. 17

Mozer, F. S. (1973), Electric fields and plasma convection in the plasmasphere, *Reviews of Geophysics*, *11*(3), 755–765, doi:https://doi.org/10.1029/RG011i003p00755. 18

NASA (2021), Our sun, `https://solarsystem.nasa.gov/solar-system/sun/in-depth/`, accessed: 04.02.22. 3

Nesse Tyssøy, H., M. I. Sandanger, L.-K. G. Ødegaard, J. Stadsnes, A. Aasnes, and A. E. Zawedde (2016), Energetic electron precipitation into the middle atmosphere—constructing the loss cone fluxes from meped poes, *Journal of Geophysical Research: Space Physics*, *121*(6), 5693–5707, doi:https://doi.org/10.1002/2016JA022752. 86, 87

Nesse Tyssøy, H., M. Sinnhuber, T. Asikainen, S. Bender, M. A. Clilverd, B. Funke, M. van de Kamp, J. M. Pettit, C. E. Randall, T. Reddmann, C. J. Rodger, E. Rozanov, C. Smith-Johnsen, T. Sukhodolov, P. T. Verronen, J. M. Wissing, and O. Yakovchuk (2022), Heppa iii intercomparison experiment on electron precipitation impacts: 1. estimated ionization rates during a geomagnetic active period in april 2010, *Journal of Geophysical Research: Space Physics*, *127*(1), e2021JA029,128, doi:https://doi.org/10.1029/2021JA029128, e2021JA029128 2021JA029128. 92

NOAA (2022), Layers of the atmosphere, `https://www.weather.gov/jetstream/layers`, accessed: 09.02.22. 24

Ohmi, T., M. Kojima, M. Tokumaru, K. Fujiki, and K. Hakamada (2004), Origin of the

slow solar wind, *Advances in Space Research*, *33*(5), 689–695, doi:https://doi.org/10.1016/S0273-1177(03)00238-2, streamers, Slow Solar Wind, and the Dynamics of the Magnetosphere. 8

Partamies, N., F. Tesema, E. Bland, E. Heino, H. Nesse Tyssøy, and E. Kallelid (2021), Electron precipitation characteristics during isolated, compound, and multi-night substorm events, *Annales Geophysicae*, *39*(1), 69–83, doi:10.5194/angeo-39-69-2021. 31

Randall, C. E., V. L. Harvey, L. A. Holt, D. R. Marsh, D. Kinnison, B. Funke, and P. F. Bernath (2015), Simulation of energetic particle precipitation effects during the 2003–2004 arctic winter, *Journal of Geophysical Research: Space Physics*, *120*(6), 5035–5048, doi:https://doi.org/10.1002/2015JA021196. 87

Ratcliffe, J. A. (1975), The early ionosphere investigations of appleton and his colleagues, *Philosophical Transactions of the Royal Society of London. Series A, Mathematical and Physical Sciences*, *280*(1293), 3–9. 29

Redmon, R. J., W. F. Denig, L. M. Kilcommons, and D. J. Knipp (2017a), New dmsp database of precipitating auroral electrons and ions, *Journal of Geophysical Research: Space Physics*, *122*(8), 9056–9067, doi:https://doi.org/10.1002/2016JA023339. 37, 38, 39, 92

Redmon, R. J., J. V. Rodriguez, C. Gliniak, and W. F. Denig (2017b), Internal charge estimates for satellites in low earth orbit and space environment attribution, *IEEE Transactions on Plasma Science*, *45*(8), 1985–1997, doi:10.1109/TPS.2017.2656465. 77

Roble, R. G., and E. C. Ridley (1994), A thermosphere-ionosphere-mesosphere-electrodynamics general circulation model (time-gcm): Equinox solar cycle minimum simulations (30–500 km), *Geophysical Research Letters*, *21*(6), 417–420, doi:\url{https://doi.org/10.1029/93GL03391}. 41

Roble, R. G., E. C. Ridley, and R. E. Dickinson (1987), On the global mean structure of the thermosphere, *Journal of Geophysical Research: Space Physics*, *92*(A8), 8745–8758, doi:https://doi.org/10.1029/JA092iA08p08745. 41

Rozanov, E., M. Calisto, T. Egorova, and W. Schmutz (2012), Influence of the precipitating energetic particles on atmospheric chemistry and climate, *Surveys in Geophysics*, *33*, 483–501, doi:10.1007/s10712-012-9192-0. 26, 28

Russell, C. (1972), Critical problems of magnetospheric physics, *1*. 16

Russell, C. T. (1993), Magnetic fields of the terrestrial planets, *jgr*, *98*(E10), 18,681–18,696, doi:10.1029/93JE00981. 8

Russell, C. T. (2000), The solar wind interaction with the earth's magnetosphere: a tutorial, *IEEE Transactions on Plasma Science*, *28*(6), 1818–1830, doi:10.1109/27.902211. 12

Sandanger, M. I., L. G. Ødegaard, H. Nesse Tyssøy, J. Stadsnes, F. Søraas, K. Oksavik, and K. Aarsnes (2015), In-flight calibration of noaa poes proton detectors—derivation of

the meped correction factors, *Journal of Geophysical Research: Space Physics*, *120*(11), 9578–9593, doi:10.1002/2015ja021388. 35, 36

Seppälä, A., K. Matthes, C. E. Randall, and I. A. Mironova (2014), What is the solar influence on climate? overview of activities during cawses-ii, *Progress in Earth and Planetary Science*, doi:10.1186/s40645-014-0024-3. 26, 27

Sinnhuber, M., H. Nieder, and N. Wieters (2012), Energetic particle precipitation and the chemistry of the mesosphere/lower thermosphere, *Surveys in Geophysics*, *33*, doi:10.1007/s10712-012-9201-3. 1, 27, 28

Sinnhuber, M., H. Nesse Tyssøy, T. Asikainen, S. Bender, B. Funke, K. Hendrickx, J. M. Pettit, T. Reddmann, E. Rozanov, H. Schmidt, C. Smith-Johnsen, T. Sukhodolov, M. E. Szeląg, M. van de Kamp, P. T. Verronen, J. M. Wissing, and O. S. Yakovchuk (2022), Heppa iii intercomparison experiment on electron precipitation impacts: 2. model-measurement intercomparison of nitric oxide (no) during a geomagnetic storm in april 2010, *Journal of Geophysical Research: Space Physics*, *127*(1), e2021JA029,466, doi:https://doi.org/10.1029/2021JA029466, e2021JA029466 2021JA029466. 92

Smith-Johnsen, C., H. Nesse Tyssøy, K. Hendrickx, Y. Orsolini, G. Kishore Kumar, L.-K. G. Ødegaard, M. I. Sandanger, F. Stordal, and L. Megner (2017), Direct and indirect electron precipitation effect on nitric oxide in the polar middle atmosphere, using a full-range energy spectrum, *Journal of Geophysical Research: Space Physics*, *122*(8), 8679–8693, doi:https://doi.org/10.1002/2017JA024364. 1, 30, 36, 85

Smith-Johnsen, C., D. R. Marsh, Y. Orsolini, H. Nesse Tyssøy, K. Hendrickx, M. I. Sandanger, L.-K. G. Ødegaard, and F. Stordal (2018), Nitric oxide response to the april 2010 electron precipitation event: Using waccm and waccm-d with and without medium-energy electrons, *Journal of Geophysical Research: Space Physics*, *123*(6), 5232–5245, doi:https://doi.org/10.1029/2018JA025418. 2, 30, 41, 85, 87, 88, 89

Smith-Johnsen, C., D. R. Marsh, A. K. Smith, H. N. Tyssøy, and V. Maliniemi (2022), Mesospheric nitric oxide transport in waccm, *Journal of Geophysical Research: Space Physics*, *127*(3), e2021JA029,998, doi:https://doi.org/10.1029/2021JA029998, e2021JA029998 2021JA029998. 2, 30, 87

SpaceWeatherLive.com (2022), The kp-index, accessed: 07.02.22. 22

Steinhilber, F., J. Beer, and C. Fröhlich (2009), Total solar irradiance during the holocene, *Geophysical Research Letters*, *36*(19), doi:https://doi.org/10.1029/2009GL040142. 26

Swider, W., and T. Keneshea (1973), Decrease of ozone and atomic oxygen in the lower mesosphere during a pca event, *Planetary and Space Science*, *21*(11), 1969–1973, doi:https://doi.org/10.1016/0032-0633(73)90126-8. 1

Sætre, C., J. Stadsnes, H. Nesse Tyssøy, A. Aksnes, S. Petrinec, C. Barth, D. Baker, R. Vondrak, and N. Ostgaard (2004), Energetic electron precipitation and the no abundance in the upper atmosphere: A direct comparison during a geomagnetic storm, *Journal of Geophysical Research*, *109*, doi:10.1029/2004JA010485. 1, 27

Sætre, C., C. A. Barth, J. Stadsnes, N. Østgaard, S. M. Bailey, D. N. Baker, and J. W. Gjerloev (2006), Comparisons of electron energy deposition derived from observations of lower thermospheric nitric oxide and from x-ray bremsstrahlung measurements, *Journal of Geophysical Research: Space Physics*, *111*(A4), doi:https://doi.org/10.1029/2005JA011391. 27, 28

Søraas, F., M. I. Sandanger, and C. Smith-Johnsen (2018), Noaa poes and metop particle observations during the 17 march 2013 storm, *Journal of Atmospheric and Solar-Terrestrial Physics*, *177*, 115–124, doi:https://doi.org/10.1016/j.jastp.2017.09.004, dynamics of the Sun-Earth System: Recent Observations and Predictions. 36

Tesema, F., N. Partamies, H. N. Tyssøy, A. Kero, and C. Smith-Johnsen (2020), Observations of electron precipitation during pulsating aurora and its chemical impact, *Journal of Geophysical Research: Space Physics*, *125*(6), e2019JA027,713, doi:https://doi.org/10.1029/2019JA027713, e2019JA027713 10.1029/2019JA027713. 30

Thorne, R. M. (1980), The importance of energetic particle precipitation on the chemical composition of the middle atmosphere, *pure and applied geophysics*, doi:10.1007/BF01586448. 21

Turunen, E., P. T. Verronen, A. Seppälä, C. J. Rodger, M. A. Clilverd, J. Tamminen, C.-F. Enell, and T. Ulich (2009), Impact of different energies of precipitating particles on nox generation in the middle and upper atmosphere during geomagnetic storms, *Journal of Atmospheric and Solar-Terrestrial Physics*, *71*(10), 1176–1189, doi:https://doi.org/10.1016/j.jastp.2008.07.005, high Speed Solar Wind Streams and Geospace Interactions. 26, 27, 66, 72

Van Allen, J. A., C. E. McIlwain, and G. H. Ludwig (1959), Radiation observations with satellite 1958, *Journal of Geophysical Research (1896-1977)*, *64*(3), 271–286, doi:https://doi.org/10.1029/JZ064i003p00271. 18

Vegard, L. (1912), Xviii. on the properties of the rays producing aurora borealis, *The London, Edinburgh, and Dublin Philosophical Magazine and Journal of Science*, *23*(134), 211–237, doi:10.1080/14786440208637215. 11

Vegard, L. (1917), Bericht über die neueren untersuchungen am nordlicht, *Jahrb. Radioakt. Elektron*, *14*, 383–466. 11

Walsh, A. P., A. N. Fazakerley, C. Forsyth, C. J. Owen, M. G. G. T. Taylor, and I. J. Rae (2013), Sources of electron pitch angle anisotropy in the magnetotail plasma sheet, *Journal of Geophysical Research: Space Physics*, *118*(10), 6042–6054, doi:https://doi.org/10.1002/jgra.50553. 86

Wang, Y.-M., J. L. Lean, and J. N. R. Sheeley (2005), Modeling the sun's magnetic field and irradiance since 1713, *The Astrophysical Journal*, *625*(1), 522–538, doi:10.1086/429689. 26

Weeks, L. H., R. S. Cuikay, and J. R. Corbin (1972), Ozone measurements in the mesosphere during the solar proton event of 2 november 1969, *Journal of Atmospheric*

Sciences, *29*(6), 1138 – 1142, doi:10.1175/1520-0469(1972)029<1138:OMITMD>2.0.CO;2. 1

Willson, R., and H. Hudson (1991), The sun's luminosity over a complete solar cycle, *Nature*, *351*, doi:10.1038/351042a0. 26

Wissing, J. M., and M.-B. Kallenrode (2009), Atmospheric ionization module osnabrück (aimos): A 3-d model to determine atmospheric ionization by energetic charged particles from different populations, *Journal of Geophysical Research: Space Physics*, *114*(A6), doi:https://doi.org/10.1029/2008JA013884. 34, 39, 40, 89

Wissing, J. M., M.-B. Kallenrode, N. Wieters, H. Winkler, and M. Sinnhuber (2010), Atmospheric ionization module osnabrück (aimos): 2. total particle inventory in the october–november 2003 event and ozone, *Journal of Geophysical Research: Space Physics*, *115*(A2), doi:https://doi.org/10.1029/2009JA014419. 89

Woolfson, M. (2000), The origin and evolution of the solar system, *Astronomy & Geophysics*, *41*(1), 1.12–1.19, doi:10.1046/j.1468-4004.2000.00012.x. 3

Zawedde, A. E., H. Nesse Tyssøy, R. Hibbins, P. J. Espy, L.-K. G. Ødegaard, M. I. Sandanger, and J. Stadsnes (2016), The impact of energetic electron precipitation on mesospheric hydroxyl during a year of solar minimum, *Journal of Geophysical Research: Space Physics*, *121*(6), 5914–5929, doi:https://doi.org/10.1002/2016JA022371. 1, 78, 82

Zell, H. (2017), Solar rotation varies by latitude, `https://www.nasa.gov/mission_pages/sunearth/science/solar-rotation.html`, accessed: 28.03.22. 4

Zhang, Y., and L. Paxton (2008), An empirical kp-dependent global auroral model based on timed/guvi fuv data, *Journal of Atmospheric and Solar-Terrestrial Physics*, *70*(8), 1231–1242, doi:https://doi.org/10.1016/j.jastp.2008.03.008. 41

Zirker, J. B. (1977), Coronal holes and high-speed wind streams, *Reviews of Geophysics*, *15*(3), 257–269, doi:https://doi.org/10.1029/RG015i003p00257. 7, 8